



Projekt Work

**Determination of the stability of pond slopes**

Submitted by:    Sophie Heiland

Matrikel: 3968743

Supervisor.:    Prof. Dr.-Ing. habil. Ivo Herle  
Dipl.-Ing. Markus Uhlig

Joana Carreto, *LENC*, Urban and Transportation Geotechnics Unit



## Abstact

KEYWORDS: Stability  
Triaxial Test  
Cementation

Author: Sophie Heiland

Topic for Project Work: Determination of the stability of pond slopes  
(Stabilitätsanalyse von Baggerseeböschungen)

Location: TU Dresden  
Fakultät Bauingenieurwesen  
Institut für Geotechnik

2019, 76 (116) Pages, 68 Figures, 16 Tables

The project work aims to analyse two zones of a quarry pond for the extraction of kaolin sand, in Rio Maior, Portugal. The study includes two primary purposes. The first purpose focuses on a geological-geotechnical site investigation and laboratory tests aiming to characterise the occurring soil in properties and layers, but also to examine the influence of expected cementation in the strength of the kaolin sand. The second purpose presents the numerical stability analysis of the quarry pond slopes.

In this connection, several classification -, triaxial - and direct shear tests were performed. The laboratory investigation reveals that the soil shows differences in particle size distribution and shearing behaviour. Besides, none of the tests indicated a significant behaviour regarding a cemented sand structure, and apparent cohesion did not occur so that the shear strength is defined as pure frictional.

Based on the determined parameters of design, a stability analysis, according to the method of slices, was carried out. In zone 1, the impact of a municipal road, which is intended to build, is analysed. The results show that stability is not precarious by the construction since the road is located far from the slope's crest, and the inclination does not exceed the soil's friction angle.

Zone 2 examines the impact of an extra load, due to excavation work, on the stability of a very steep slope. The high inclinations reveal that an apparent cohesion must exist. Since laboratory tests do not provide sufficient information, the smallest assumable cohesion is defined for obtaining a global factor of safety of 1.0. As a result, the stability analysis does not indicate sufficient safety. However, since the work is not a permanent situation, stability can be assured by excavating from area to area to increase the factor of safety.

The laboratory tests described in this study were performed in the National Laboratory for Civil Engineering (*LNEC*), Lisbon, Portugal.

## **Acknowledgement**

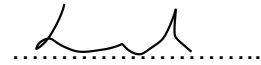
I want to thank the National Laboratory for Civil Engineering of Portugal for the warm welcome and for giving me the opportunity to participate in such an exciting project.

## Selbstständigkeitserklärung

Hiermit versichere ich, dass ich die vorliegende Arbeit ohne unzulässige Hilfe Dritter und ohne Benutzung anderer als der angegebenen Hilfsmittel angefertigt habe; die aus fremden Quellen direkt oder indirekt übernommenen Gedanken sind als solche kenntlich gemacht.

Die Arbeit wurde bisher weder im Inland noch im Ausland in gleicher oder ähnlicher Form einer anderen Prüfungsbehörde vorgelegt und ist auch noch nicht veröffentlicht worden.

Lissabon, 05.08.2019



.....  
Sophie Heiland



# Table of Contents

<b>List of Figures</b> .....	<b>III</b>
<b>List of Tables</b> .....	<b>V</b>
<b>List of Symbols</b> .....	<b>VI</b>
<b>List of Abbreviation</b> .....	<b>VIII</b>
<b>1 Introduction</b> .....	<b>9</b>
1.1 Introduction .....	9
1.2 Site investigation and Soil Sampling .....	9
1.3 Laboratory Tests .....	12
1.4 Organisation.....	12
1.5 Mohr-Coulomb Failure Criterion .....	13
<b>2 Soil Classification</b> .....	<b>14</b>
2.1 Soil Appearance.....	14
2.2 Determination of Water Content .....	14
2.3 Determination of Particle Density .....	15
2.3.1 Procedure .....	15
2.3.2 Calculations .....	15
2.3.3 Results.....	16
2.4 Determination of Liquid and Plastic Limits .....	16
2.4.1 Determination of Liquid Limit by the Casagrande Method .....	16
2.4.2 Results.....	17
2.5 Determination of Particle Size Distribution.....	17
2.5.1 Sieving Method .....	17
2.5.2 Procedure .....	18
2.5.3 Calculations .....	18
2.5.4 Results.....	19
2.6 Conclusion .....	20
<b>3 Determination of the Shear Strength</b> .....	<b>21</b>
3.1 Triaxial Test.....	21
3.1.1 Description .....	21
3.1.2 Test Procedure.....	23
3.1.3 Test Procedure of the Sample of Zone 2.....	27
3.1.4 Calculations .....	28
3.1.5 Results of Sample 5578 of Zone 1 .....	29
3.1.6 Results of Sample 5593 and Sample 5597 from zone 2.....	36
3.1.7 Source of Errors .....	39
3.2 Direct Shear Test .....	39
3.2.1 Test Procedure.....	40
3.2.2 Calculations .....	41
3.2.3 Problems during Testing .....	42
3.2.4 Results.....	43
3.3 Discussion.....	45
3.3.1 Differences between Triaxial and Direct Shear Test.....	45
3.3.2 Effect of Cementation.....	46
3.3.3 Comparison of Zone 1 and one 2 .....	48
3.4 Conclusion .....	48
<b>4 Stability Analysis</b> .....	<b>50</b>
4.1 Numerical Implementation.....	50
4.1.1 Failure Mode and Method of Slices .....	50
4.1.2 Factor of Safety (FS).....	51
4.1.3 Method and Fundamental Assumptions .....	52
4.1.4 Pore Water.....	56

4.1.5	The Grid and Radius Method .....	56
4.2	Analysing of Zone 1.....	58
4.2.1	Slope Model .....	58
4.2.2	Numerical Analysis.....	59
4.3	Analysis of Zone 2.....	64
4.4	Discussion.....	67
4.5	Conclusion .....	68
<b>5</b>	<b>Conclusion .....</b>	<b>69</b>
<b>6</b>	<b>Review .....</b>	<b>70</b>
	<b>References.....</b>	<b>71</b>
<b>A</b>	<b>Tables and Figures .....</b>	<b>73</b>
<b>B</b>	<b>Data Sheets .....</b>	<b>77</b>



## List of Figures

Figure 1.1: (right) Location of Rio Maior, (left) Aerial view of the quarry pond ( <i>Google Maps, 2019</i> ) -----	9
Figure 1.2: Current appearance of the quarry pond slopes, zone 1 (left), zone 2 (right) -----	10
Figure 1.3: SPT results zone 2 for S2-1 (left) and S2-2 (right) -----	10
Figure 1.4: SPT results zone 1 for S1-1 (left) and S1-2 (right) -----	10
Figure 1.5: Location of sampling by cylindrical cutters -----	11
Figure 1.6: Procedure of sampling by cylindrical cutter. (a) distribution of cylinder on the soil's surface, (b) driving by impact, (c) excavation and sealing -----	11
Figure 1.7: Mohr-Coulomb circle (Dohmel, 2014) -----	13
Figure 2.1: Soil appearance, (a) zone 1, (b) zone 2, (c) both zones -----	14
Figure 2.2: Soil consistency according to the associated water content (Fratta, et al., 2007 ) -----	16
Figure 2.3: Particle size distribution plot of the tested samples -----	19
Figure 3.1: Schmetical set up of the triaxial cell used for testing (Dr. Rees, 2013)-----	22
Figure 3.2: Schematic of GDS Pressure/Volume Controller used for testing (GDS Instruments, 2019) -----	22
Figure 3.3: Preparation of the specimens from sample 5578 , (a) sawing in sections, (b) appearance before testing, (c) cell chamber-----	23
Figure 3.4: Pressure during B-Value check -----	24
Figure 3.5: Development of pressure during saturation -----	24
Figure 3.6: Process of consolidation for specimen 500 kPa -----	26
Figure 3.7: Appearance of sample 5593, (a) in the tube, (b) before shearing, (c) after shearing -----	27
Figure 3.8: Appearance of sample 5597 before testing -----	28
Figure 3.9: Specimen appearance after shearing (left 50 kPa, middle 280 kPa; left 500kPa)-----	30
Figure 3.10: Deviatoric stress-axial strain behaviour of sample 5578 from zone -----	31
Figure 3.11: Stress ratio – axial strain behaviour of sample 5578 from zone 1 -----	31
Figure 3.12: Pore pressure - axial strain behaviour of sample 5578 from zone 1 -----	32
Figure 3.13: Peak strength – dilatancy behaviour for specimen 280 kPa-----	32
Figure 3.14: p'-q plot of sample 5578 from zone 1 -----	33
Figure 3.15: Pore pressure development of specimen 500 kPa -----	33
Figure 3.16: Failure envelope with the highest correlation, $c' \neq 0$ of sample 5578 -----	34
Figure 3.17: Failure envelope for the assumption that $c' = 0$ of sample 5578 -----	34
Figure 3.18: Mohr's Circle plot for sample 5578 and state of stress at failure for specimen 280 kPa-----	35
Figure 3.19: Failure envelope for the critical state of sample 5578 from zone 1 -----	35
Figure 3.20: Mohr-Coulomb envelope for peak and critical strength-----	35
Figure 3.21: Associated deviator stress at the turning point from contraction to dilation of specimen 280 kPa -----	36
Figure 3.22: Characteristic line of sample 5578 -----	36
Figure 3.23: Specimen 280 kPa of sample 5593 after shearing -----	37
Figure 3.24: deviatoric stress-axial strain behaviour of sample 5593 from zone 2 -----	38
Figure 3.25: Stress ratio – axial strain behaviour of sample 5593 from zone 2 -----	38
Figure 3.26: Pore pressure - axial strain behaviour of sample 5593 from zone 2 -----	38
Figure 3.27: p'-q behaviour of sample 5593 from zone 2-----	38
Figure 3.28: Peak failure envelope of sample 5593-----	38
Figure 3.29: Critical failure envelope of sample 5593 -----	38

Figure 3.30: Influence of friction between the specimen's ends (Rackwitz, 2005), Deformation during testing: from cylindrical to barrel-shaped.-----	39
Figure 3.31: Shear box apparatus (ISO 17892-10, 2018)-----	40
Figure 3.32: Specimen preparation for the direct shear test-----	40
Figure 3.33: (a) Tilting of the top cap, (b) soil in between the frames-----	42
Figure 3.34: Stress-strain plot from the direct shear test of sample 5604-----	43
Figure 3.35: Plot of vertical displacement against horizontal displacement of sample 5604-----	43
Figure 3.36: Comparison of direct shear behaviour between sample 5604 (continuous) and sample 5609 (pointed)-----	44
Figure 3.37: Failure envelopes from the direct shear test of sample 5604, $\phi'_{peak} =$ $41^\circ$ and $\phi'_{crit} = 26^\circ$ -----	44
Figure 3.38: Stress-strain plots from the direct shear test of the specimens of 50 kPa	44
Figure 3.39: Plots of vertical displacement against horizontal displacement $f$ of the specimens of 50 kPa-----	44
Figure 3.40: Effect of cementation (a) yielding points under different confining pressures (b) associated axial strain behaviour (Asghari, et al., 2002)-----	47
Figure 3.41: Behaviour of over consolidated soil (Lang, et al., 2011)-----	47
Figure 4.1: Acting interslice forces-----	52
Figure 4.2: Slice according to Bishop-----	53
Figure 4.3: Free body and force polygon for the Bishop's Simplified method (GEO- SLOPE International Ltd, 2018)-----	56
Figure 4.4: Pore pressure from a piezometric line-----	56
Figure 4.5: Grid and Radius Method (GEO-SLOPE International Ltd, 2018)-----	57
Figure 4.6: Optimal result of the Grid and Radius Method (GEO-SLOPE International Ltd, 2018)-----	57
Figure 4.7: Slope model of zone 1-----	59
Figure 4.8: Behaviour of the FA due to purely frictional soil-----	60
Figure 4.9: Global critical slip surface of section 57-----	60
Figure 4.11: Critical slip surface in a depth of 10 m-----	61
Figure 4.10: Critical slip surface in a depth of 10 m-----	61
Figure 4.12: Shear strength development along the base of the slip surface, with consideration of pore pressure (right), without pore pressure (left)-----	62
Figure 4.13: Critical slip surface cutting the road, current geometry (right), geometry with sectional change-----	63
Figure 4.14: Critical slip surface with the lowest FS in consideration of the road and safety factors-----	63
Figure 4.15: Slope Model zone 2-----	64
Figure 4.17: FS of 1.0 with a cohesion of 10 kPa-----	65
Figure 4.17: Trial distances to examine the impact of an additional load-----	65
Figure 4.18: Critical slip surfaces caused by line loads of 3 m, 6 m and 9 m distance to the slope's crest-----	65
Figure 4.19: Critical slip surface caused by pressure lines, (a) 3 m – 6 m distance, (b) 6 m – 9 m distance-----	66
Figure 4.20: Areas mobilised by different definitions of load-----	66
Figure B.1: Location of boreholes in zone 1-----	73
Figure B.2: Location of boreholes on zone 2-----	73
Figure B.3: Stress-strain behaviour of sample 5597-----	76
Figure B.4: Stress ratio - strain behaviour of sample 5597-----	76
Figure B.5: Pore pressure – strain behaviour of sample 5597-----	76
Figure B.6: Stress path of sample 5597-----	76

## List of Tables

Table 1.1: Correlation between $n_{30}$ for.....	11
Table 1.2: Intended laboratory tests for investigation the sand from Rio Maior.....	12
Table 2.1: Results from the pycnometer method for the determination of particle density .....	16
Table 3.1: Applied stresses for consolidation stage .....	25
Table 3.2: Values for consolidation from a sample 5593 of zone 2.....	28
Table 3.3: Values for consolidation from a sample 5597 of zone 2.....	28
Table 3.4: Essential data from <i>CU</i> -test according to the stress-strain behaviour.....	31
Table 3.5: Evaluation $p'-q$ plot to Mohr-Coulomb failure criteria .....	34
Table 3.6: Effective stresses and associated weights for the direct shear test .....	41
Table 3.7: Results of from the direct shear test from the specimens of 50 kPa .....	44
Table 3.8: Parameters of design based on the laboratory results.....	49
Table 4.1: Methods of slope stability analyses (Adeyeri, 2015).....	51
Table 4.2: Summarized soil parameter of design for zone 1.....	59
Table 4.3: Adjustments in <i>GEO-SLOPE</i> for the analysis of zone 1.....	59
Table 4.4: Evaluation of the sliding mass for the slip surface in a depth of 10 m.....	61
Table 4.5: Summarized parameter of design for zone 2.....	64
Table 4.6: Resulted <i>FS</i> of the load trials .....	65
Table A.1: Performed laboratory tests.....	74
Table A.2: Determined water content of all sample .....	75
Table A.3: Result from the particle size distribution.....	75

## List of Symbols

### Latin

$A$	Cross section area	$\text{mm}^2$
$A_c$	Corrected cross sectional area	$\text{mm}^2$
$B$	B-Value	-
$C$	Probe ring constant	$\text{kN/mm}$
$C_C$	Coefficient of curvature	-
$C_U$	Coefficient of uniformity	-
$d$	Specimen diameter	$\text{cm}$
$E$	Horizontal interslice normal force	$\text{kN/m}$
$e$	Void ratio	%
$F$	Factor of safety	
$F$	Axial Force	$\text{kN}$
$F_f$	FA with respect to horizontal force equilibrium	-
$F_m$	FA with respect to moment equilibrium	-
$f_n$	Fraction passing the given sieve size n	%
$g$	Acceleration of gravity = 9.81	$\text{m/sec}^2$
$H$	Specimen height	$\text{cm}$
$h$	Slice height	$\text{m}$
$H_d$	Sum of the driving forces	$\text{kN}$
$H_r$	Sum of the resisting forces	$\text{kN}$
$k$	Temperature correction factor	-
$m$	Initial mass of the specimen	$\text{g}$
$m_d$	total dry mass	$\text{g}$
$M_d$	Sum of driving moment	$\text{kNm/m}$
$M_r$	Sum of resisting moment	$\text{kNm/m}$
$m_{ssn}$	Mass of soil retained on sieve size n	$\text{g}$
$m_w$	Total water mass	$\text{g}$
$N$	Total normal force on the base of the slice	$\text{kN/m}$
$N'$	Effective normal force on the base of the slice	$\text{kN/m}$
$p$	Mean Stress	$\text{kPa}$
$q$	Deviator Stress	$\text{kPa}$
$T$	Shear force mobilised on the base of each slice.	$\text{kN/m}$
$V$	Initial volume of specimen	$\text{cm}^3$
$W$	Total weight of a slice	$\text{kN/m}$
$w$	Water content	%
$X$	Vertical interslice shear force	$\text{kN/m}$

## Greek

	...	
$\Delta h$	Horizontal displacement during shearing	mm
$\Delta l$	Base length of each slice	m
$\Delta s$	Shear way	mm
$\Delta u$	Change in pore pressure at the mid height of the specimen	kPa
$\Delta v_1$	Vertical displacement during shearing	mm
$\Delta x$	Width of each slice	m
$\Delta \varepsilon_1$	Axial Strain	%
$\Delta \sigma_c$	Change in cell pressure	kPa
$c'$	Effective cohesion	kPa
$\beta$	Inclination of slope	°
$\gamma_s$	Unit weight of soil	N/m <sup>3</sup>
$\gamma_w$	Unit weight of water	kN/m <sup>3</sup>
$\vartheta$	Orientation of failure plane	°
$\rho$	Bulk density	g/cm <sup>3</sup>
$\rho_d$	Dry density	g/cm <sup>3</sup>
$\rho_s$	Particle density	g/cm <sup>3</sup>
$\sigma_1$	Major principal stress	kPa
$\sigma_3$	Minor principal stress	kPa
$\sigma_B$	Back pressure	kPa
$\sigma_c$	Cell pressure	kPa
$\phi'$	Effective friction angle	°
$\theta$	Angle between the tangent to the centre of the base of each slice and the horizontal	°

## List of Abbreviation

<i>CD</i>	Consolidated drained
<i>CU</i>	Consolidated undrained
<i>FS</i>	Factor of Safety
<i>ISO</i>	International Organization for Standardization
<i>OC</i>	Over consolidated
<i>SPT</i>	Standard penetration test
<i>UU</i>	Unconsolidated undrained

# 1 Introduction

## 1.1 Introduction

In Rio Maior a city in Portugal, 100 km in the north of Lisbon, the exploitation of fine and well-calibrated kaolin sands, of high economic interest, is carried out by SIBELCO Company in a pond by using a floating dredger equipped with a suction pump that draws the sand from the bottom of the lake and pumps it to treatment ponds. This process causes the progressive and controlled destabilisation of the pond slopes, providing new material to feed the process. In this regard, a request was made to the National Laboratory for Civil Engineering (*LNEC*) for analysing the stability of two slopes. Figure 1.1 presents the location of the two zones. In zone 1, a municipal road will be built in the immediate vicinity of the quarry pond. Therefore, it is requested to examine to what extent the construction of the road has an impact on the stability of the slope.

In Zone 2, an expansion of the current exploitation to an adjacent area is planned. The actual inclination of the pond slope suggests that stability is precarious and could affect the safety of new exploitation area. Therefore, the safety conditions associated with this excavation related procedures will be assessed.



Figure 1.1: (right) Location of Rio Maior, (left) Aerial view of the quarry pond (*Google Maps, 2019*)

## 1.2 Site investigation and Soil Sampling

A site investigation was carried out, giving first information about the vicinity of the quarry pond and the occurring soil. A first assessment of the current conditions reveals that in some places, the slopes follow very steep inclinations (Figure 1.2). It leads to the conclusion that the occurring kaolin sand consists of a cemented structure. Furthermore, the investigation assumes that zone 1 and zone 2 coincide in soil.

## 1.2 Site investigation and Soil Sampling



Figure 1.2: Current appearance of the quarry pond slopes, zone 1 (left), zone 2 (right)

Based on the first site investigation, the number, type, and location of soil sampling were defined. For the slope analysis, undisturbed samples are required to characterise the sand's properties and to determine the parameters of design. Therefore, two borings in each zone were performed, aiming to maintain samples with the in-situ water content, void ratio, and soil structure. The boring was carried out by small scale boreholes, using an open-tube sampler with a diameter of  $60\text{ mm}$  to retrieve the samples. Moreover, the drilling was accompanied by a polymer slurry as a drilling fluid to minimise the disturbance. The location of the boreholes in zone 1 coincide with the location of the intended municipal road and is presented in Figure A.1, whereas Figure A.2 shows the approximate location of the two boreholes in zone 2.

Additionally, the boreholes were accompanied by Standard Penetration Tests (*SPT*) of every  $1.5\text{ m}$  to determine the in-situ compactness. The *SPT* is carried out by driving a standard sampler  $45\text{ cm}$  from the bottom of the borehole into the soil while recording the required number of blows (*N-value*) to penetrate the last  $30\text{ cm}$  (1 foot). From the *N-value*, the soil's compactness can be assessed, as shown in Table 1.1. As higher the compactness as higher is the resistance against penetration. Figure 1.3 and Figure 1.4 illustrate the *SPT* results of both zones. In zone 1, in the first  $10\text{ m}$  below the surface, the soil turns from medium dense to dense. Below  $10\text{ m}$ , the soil appears very dense since more than  $60$  blows were required to penetrate  $30\text{ cm}$ . In zone 2, very dense soil occurs along the whole depth. To conclude, the *SPT* results reveal that the occurring soil shows general high compactness in zone 1 and zone 2. Besides, the investigation detected that the water table occurs at  $56\text{ m}$ .

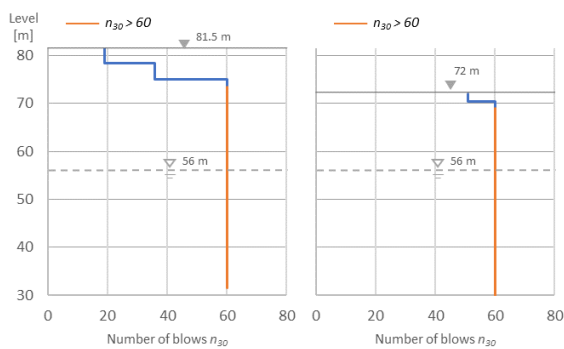


Figure 1.4: SPT results zone 1 for S1-1 (left) and S1-2 (right)

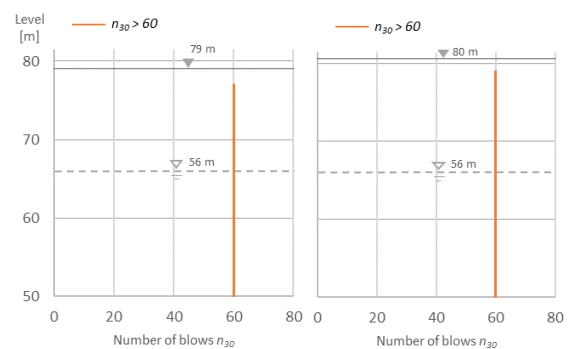


Figure 1.3: SPT results zone 2 for S2-1 (left) and S2-2 (right)



# 1 Introduction

Table 1.1: Correlation between  $n_{30}$  for granular soils (Kolymbas, 2016)

$n_{30}$	Compactness
0 - 4	very loose
4 - 10	loose
10 - 30	medium dense
30 - 50	dense
> 50	very dense



Figure 1.5: Location of sampling by cylindrical cutters

Furthermore, several soil samples were taken by cylindrical cutters from the soil's surface, aiming to minimise disturbance to maintain an intact soil structure. The location of the sampling was outside zone 1 but in a part of the same soil (Figure 1.5). The procedure of retrieving is illustrated in Figure 1.6. Therefore, a clean and plane vicinity where the sand did not indicate contamination was chosen to collect the samples. At first, an excavator removed around  $30\text{ cm}$  of the upper soil layer to disclose a smooth and plane surface to distribute the cylindrical cutters. By the impact of a heavy metal bullet from a vertical rod, the cutters were driven into the soil, followed by excavation and an appropriate sealing with caps and tape. Until testing, the sample tubes and sample container rested in a humidity room protected from sunlight to prevent the loss of natural water



Figure 1.6: Procedure of sampling by cylindrical cutter. (a) distribution of cylinder on the soil's surface, (b) driving by impact, (c) excavation and sealing

## 1.3 Laboratory Tests

### 1.3 Laboratory Tests

The laboratory investigation aims to determine essential soil properties for defining the parameters of the design regarding the stability analysis. Besides, it shall provide information about the homogeneity of the soil and if different layers occur. The intended tests follow the European Standards (*ISO*) and are presented in Table 1.2. The number of tests and the associated samples can be seen in Table A.1. Classification tests are carried out on several samples, whereas one triaxial test is provided for each zone. For zone 1 the triaxial test is accompanied by several direct shear tests, giving an additional assessment for the shear strength. The consolidation stresses for the triaxial and direct shear tests are defined by *LNEC*, based on the depth of the collected sample.

Table 1.2: Intended laboratory tests for investigation the sand from Rio Maior

Laboratory test	Standard	QUAN
Determination of particle density	<i>by LNEC</i>	4
Particle size distribution by sieving	<i>ISO 17892-4</i>	8
Determination of liquid and plastic limits	<i>ISO 17892-12</i>	8
Determination of water content	<i>ISO 17892-1</i>	14
Direct shear test	<i>ISO 17892-10</i>	6
Consolidated triaxial compression tests, <i>CU</i>	<i>ISO 17892-9</i>	2

### 1.4 Organisation

The main purpose of the project is the stability analysis of two slopes of a quarry pond for sand extraction. Therefore, the project is divided into two parts; one is the laboratory determination of the properties of the occurring soils, whereas the other part focuses on the numerical slope analysis.

Chapter 2 describes the soil classification, which aims to characterise the soil, regarding particle size distribution and plasticity, to conclude if the occurring soil shows homogeneity. Chapter 3 continues with the laboratory determination of the soil's shear strength. At first, the applied test procedure is generally described, followed by the presentation of the results and interpretation. In this connection, the test description and interpretation focus on the soil from zone 1; however, all results from zone 2 are presented and related to zone 1. As a result, the laboratory tests provide information about soil models, which form the base for the subsequent slope analysis. Moreover, conclusions can be drawn to which extent cementation impacts the soil's mechanical properties.

The second part of the project concentrates on the slope stability. The analysis is carried out by a numerical program, which bases on the method of slices. Therefore, Chapter 4 first explains the elementary assumptions and methods of the program, followed by the numerical analysis of the slope stability. Here again, the analysis focuses on the slope in zone 1 and is described in detail. In the end, an assessment of possible slip surfaces and the associated factor of safety reveal, whether the slope is stable or if stability improvements are necessary.

### 1.5 Mohr-Coulomb Failure Criterion

Analysing slope stability is based on the shear strengths of soil. Therefore, an essential part of the project includes the determination of the shear strength of the sand from Rio Maior. Thus, a failure criterion must be defined, allowing to describe the shear strength by simple experimental investigations such as triaxial test or direct shear test. Regarding this, the Mohr-Coulomb criterion provides the most significant applicability. It assumes that by a given stress ratio between the major principal stress  $\sigma_1$ , and the minor principal stress  $\sigma_3$  the shear stress is directly proportional to the associated normal stress (Lang, et al., 2011). As a result, Mohr defines the maximal shear stress acting on a failure plane as a linear function of the normal stress, where the gradient relates to the internal friction angle, while the intercept defines the cohesion. Hence, every state of normal stress has an associated maximal shear stress, which the soil can still resist.

Since water has an impact on slope stability, the failure criterion for effective stress, according to Mohr-Coulomb, is defined as:

$$\tau = \sigma' \cdot \tan(\phi') + c' \tag{1.1}$$

Nevertheless, shear strength parameters are not uniform and distinguish from different soils. Therefore, the parameters must be determined by laboratory tests. The experimental investigation of the shear strength is carried out on one soil sample but under three different stress conditions. As a result, the failure envelope can be illustrated by plotting the Mohr circle for every stress condition and defining the tangent, which touches all circles in one point (Figure 1.7). The tangent function equates Formula (1.1), allowing the determination of the effective shear strength parameter  $\phi'$  and  $c'$ .

Numerous experiments show that the Mohr-Coulomb criterion provides good approximation within a reasonable range of stresses. Just at higher normal stresses of  $2 \text{ MN/m}^2$  the line levels out (Lang, et al., 2011). However, the laboratory determination of shear strength bases on the here presented criterion, allowing to analyse the quarry pond slopes from Rio Maior.

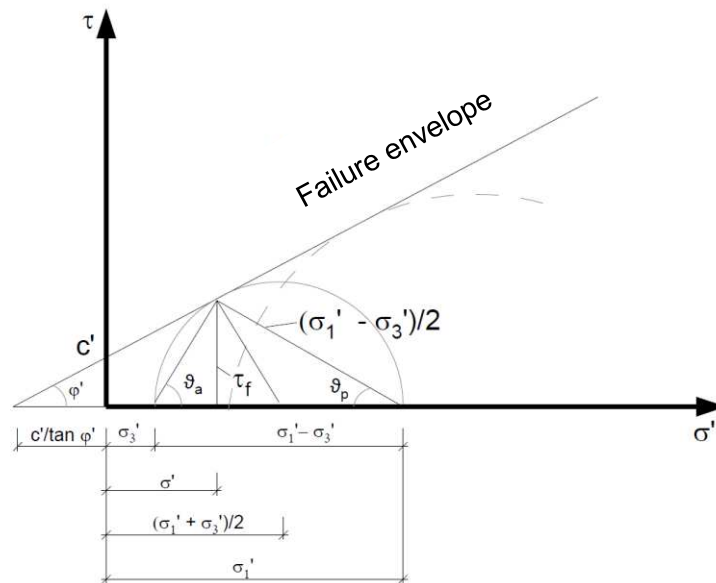


Figure 1.7: Mohr-Coulomb circle (Dohmel, 2014)

## 2 Soil Classification

### 2.1 Soil Appearance

From the soil appearance, first conclusions can be drawn, regarding soil properties and soil behaviour. Therefore, the appearance of all samples, from zone 1 and zone 2, is summarised below. Generally, all samples indicate sand with uniform particle diameters. From zone 1 (Figure 2.1, a), borehole S1-1 and S2-1, the samples indicate a white light colour with a small yellowish additional in some parts. The soil's structure seems very compact, whereas crushing the particles by fingers can be performed easily. The samples from zone 2 (Figure 2.1, b), borehole S2-1 and S2-2, show a different colour, which appears more yellow to orange. Besides, the soil seems softer with a less compact structure. In borehole S2-2, at a depth of 10 m, the soil from zone 2 coincide with the soil from zone 1. Besides, none of the samples shows an appearance of interparticle bonding as it was assumed before.



Figure 2.1: Soil appearance, (a) zone 1, (b) zone 2, (c) both zones

### 2.2 Determination of Water Content

For every sample, the water content is determined, giving valuable information about the occurring water in the field. In general, three separate portions of each sample are placed in a container of a known mass. Afterwards, the mass of each container, including the soil, is measured and dried at 105° C. According to ISO 17892-1, 16 hours of drying is sufficient to ensure all water has disappeared. Finally, the mass of the container, including the dry soil, is measured to determine the water content of the soil, according to formula (2.1).

$$w = \frac{m_1 - m_2}{m_2 - m_c} \cdot 100 = \frac{m_w}{m_d} \cdot 100 \quad (2.1)$$

$m_1$	mass of container including wet specimen
$m_2$	mass of the container and dry specimen
$m_c$	mass of container

## 2 Soil Classification

Table A.2 presents the determined water contents of all samples. The average water content of zone 1 equates 20,5 % and of zone 2 18 %. A high content already appears in small depth and slightly rises with increasing depth. The samples retrieved by cylindrical cutters indicate an average water content of 5 % since they were taken from a superficial part.

### 2.3 Determination of Particle Density

The density of solid particles  $\rho_s$  is a fundamental soil property and besides an essential parameter for the determination of the soil's void ratio. The determination is carried out by the fluid pycnometer method, which bases on the volumetric difference between a pycnometer only filled with a control fluid and a pycnometer filled with a control fluid and soil. For the control fluid, the density must be known. This is provided by using distilled water whereby the density concludes from the current water temperature. The procedure and calculations are carried out according to standards from *LNEC*. The tested samples are presented in Table A.1.

#### 2.3.1 Procedure

For each soil sample, three specimens are tested. Before starting, soil particles bigger than 4 mm are removed by sieving. Besides, the pycnometer shall be completely clean to ensure that results are not influenced by additional weight. The specimen is placed in the pycnometer of 100 ml, followed by the determination of dry mass. Afterwards, the pycnometer is filled with distilled water until the specimen is completely covered so that it can pre-soak. Carefully heating the water-soil mixture removes the surplus air. Subsequently, further distilled water is filled into the pycnometer until reaching the limit line of 100 ml. Besides, the water temperature must be known by measuring the temperature not directly from the pycnometer, but from another container filled with the same water, assuming that the temperatures coincide. Finally, the mass of the pycnometer, including distilled water and soil, and the dry mass of the specimen are determined. The same procedure is repeated for a pycnometer only filled with distilled water. The obtained masses allow to calculate the volume of soil particles, and with it the particle density.

#### 2.3.2 Calculations

According to the standards from *LNEC*, the particle density can be calculated from:

$$\rho_s = k \cdot \frac{m_4}{m_3 - (m_5 - m_4)} \quad (2.2)$$

$m_3$	the mass of the pycnometer filled with distilled water [g]
$m_5$	mass of the pycnometer with the specimen and filled with distilled water [g]
$m_4$	is the dry mass of test specimen [g]
$k$	temperature correction factor [g/cm <sup>3</sup> ]

The results and the table for the temperature correction factor  $k$  are presented in the associated Datasheet in Annexe B.



## 2.4 Determination of Liquid and Plastic Limits

### 2.3.3 Results

Table 2.1 presents the results of the pycnometer method from all tested samples. All sample indicate similar results, except sample 5606. It is assumed that the test was inaccurate since, during heating, an explosive reaction caused a loss of soil. By neglecting the results from sample 5606, the average particle density equates  $2,68 \frac{g}{cm^3}$ .

Table 2.1: Results from the pycnometer method for the determination of particle density

Sample	5578	5593	5606	5604
Borehole	S1-1	S2-1	Cylindric cutter	Cylindric cutter
Depth	13,50 - 14,10 m	12,00 -12,80 m	superficial	superficial
$\rho_s$	2.68 g/cm <sup>3</sup>	2.69 g/cm <sup>3</sup>	2.62 g/cm <sup>3</sup>	2.68 g/cm <sup>3</sup>

## 2.4 Determination of Liquid and Plastic Limits

Plasticity of soil is defined by the liquid and plastic limits, which are important indicator for the soil's water retention ability. Generally, only fine-grained soils like clays have this ability. Nevertheless, the soil from Rio Maior is a composition of sand with a fine-grained fraction of kaolin clay. Therefore it is reasonable to examine if the kaolin particles provide plasticity. From Figure 2.2, it can be seen that the water content controls the soils consistence. Hence, the plastic limit describes the water content at which the soil turns from semisolid to plastic, whereas the liquid limit describes the water content at which the soil starts to flow to a liquid consistency. According to *ISO 17892-12*, the liquid limit is determined according to Casagrande and the plastic limit by rolling soil threads till they start to crumble.

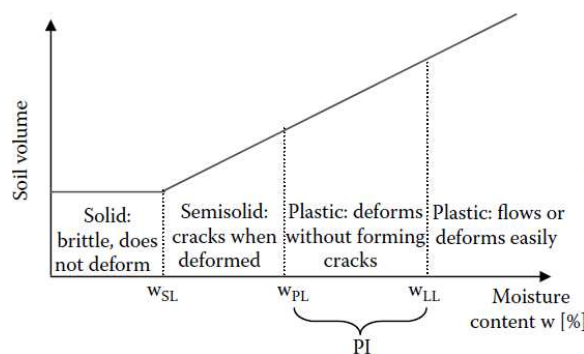


Figure 2.2: Soil consistency according to the associated water content (Fratta, et al., 2007 )

### 2.4.1 Determination of Liquid Limit by the Casagrande Method

For each test, four specimens of one sample are tested. For the specimen preparation, an oven-dried sample of around 200 g is remoulded to a paste by mixing the soil with water and stirring it with a spatula until obtaining the proper consistency. Now, one part of the paste is placed in the specimen cup, flattening it to a soil layer with a maximal thickness of 1 cm. By using a grooving tool, a gap is stroked along the middle of the soil layer. The determination of the liquid limit is carried out by a Casagrande apparatus. The apparatus consists of a specimen cup which can be lifted and dropped by rotating a cam. This action causes a flowing of the specimen, which slowly closes the gap in the middle.

## 2 Soil Classification

It is suggested to carry out the test at two rotations per second until the gap closes to a length of at least *1 cm*. The required number of rotations is automatically recorded by the Casagrande apparatus. According to *ISO 17892-12*, the number of rotations shall fall in a range of *15* to *40*. Tests outside this range must be repeated. Afterwards, a part of the specimen is used for the determination of the correlating water content, whereas the other part is used to remould new specimens of another water content to repeat the test. The test aims to identify the water content at which the specimen needs *25* rotations to close *1 cm* of the gap. The numbers of rotation shall be above and below *25*. Plotting the counts of rotation against the associated water content allows obtaining the liquid limit by connecting all points to an approximated linear line.

### 2.4.2 Results

The test was conducted only on sample *5593* and *5596*. Both tests did not obtain precise results since the soil directly liquidated while closing the whole gap in one process. Therefore, a plastic transformation did not appear before liquefaction. Since sands have bigger particle surfaces, a water retention ability is not provided. As a result, there are no bonding forces between water and the particles. The action of the cup's movement causes a change in the sand's structure. The sand cannot mobilise interparticle friction anymore since water between the particles prevents contacting, and therefore, the soil collapse. According to that, the fine-grained fraction has no impact on this behaviour. It can be concluded that the soil from Rio Maior does not provide a liquid limit. According to that, a plastic limit will not be obtained either, and further tests are not necessary to carry out.

## 2.5 Determination of Particle Size Distribution

Particle size distribution is an essential characteristic of soils, defining many geotechnical and geohydrological properties, and besides, it is an important indicator regarding the shear strength of sand. The method of determination depends on the particle sizes and composition of the soil. The sieving method is used for coarse soils, whereas the sedimentation method is tested on fine soils. For mixed soils, a combination of both methods is reasonable. As is known, the in-situ soil of the quarry pond is a composition of sand with a fine-grained fraction of kaolin clay. It is assumed that this fine-grained fraction is less than *10 %*, for which reason, according to *ISO 17892-4*, a sieving method is adequate for the determination of particle size distribution. Nevertheless, it is necessary to remove the fine-grained fraction before sieving since bonded particles could affect the results.

### 2.5.1 Sieving Method

As described, the sieving method is used for coarse soils. The separation of the different particle ranges is carried out by using a stack of standard metal sieves. Therefore, *LNEC* provides sieves for the range of sands with meshes of *0,84 mm*, *0,42 mm*, *0,25 mm*, *0,177 mm*, *0,105 mm* and *0,074 mm*. As a result, the fraction passing each sieve is plotted in a semi-logarithmic diagram, which reveals the soil's main fraction as well as the coefficient of uniformity  $C_u$  and the coefficient of curvature  $C_c$ . The tested samples are presented in Table A.1. According to that, for every zone and borehole, at least one sieving is conducted

## 2.5 Determination of Particle Size Distribution

### 2.5.2 Procedure

Sieving is carried out on dry specimens. As already discussed, it is necessary to remove the fine part from the specimen since interparticle bonding shall not affect the results. Therefore, the specimen must pre-soak to dissolve the kaolin, followed by washing the specimen through a sieve of  $0,063\text{ mm}$ . Within the specimen, the kaolin minerals are well seen as small white particles. The washing finishes once water is coming out clear with no appearance of further white particles. Subsequently, the wet specimen must dry in the oven, followed by weighing the dry mass to determine the amount of fine particles, which has been removed by washing. At this stage, the specimen only consists of sand particles and the sieving can be carried out.

For the procedure, the sieves are stacked with the coarsest mesh on top and the finest mesh on the bottom. At first, it is necessary to place the whole amount of the specimen on the top sieve, followed by locking the sieves and shaking it by hands that the particles pass the appropriate mesh. A brush can be used to remove deadlocked particles in between the mesh to ensure they pass the sieve. Afterwards, the retained amount of soil on each sieve is recorded. The last sieve on the bottom is rather a container where the fine particles retain. The amount is calculated to the mass of fine particles which has been removed by washing before.

### 2.5.3 Calculations

According to *ISO 17892-4* (2016), the fraction passing each sieve is defined as

$$f_n = 100\% - \left[ \frac{m'_{ss1} + m'_{ss2} + \dots + m'_{ssn}}{m} \times 100\% \right] \quad (2.3)$$

- $f_n$  the fraction passing the given sieve size  $n$  (%)  
 $m_{ssn}$  mass of soil retained on sieve size  $n$ , for sieve sizes greater than or equal to the given sieve size  $n$   
 $m$  the total dry mass of the initial soil specimen (g)

Furthermore, the Coefficient of Uniformity  $C_u$ , and the Coefficient of Curvature  $C_c$ , which draw conclusions from the soil's grading, are calculated from (2.4) and (2.5).

Coefficient of uniformity:

$$C_u = \frac{d_{60}}{d_{10}} \quad (2.4)$$

Coefficient of curvature:

$$C_c = \frac{d_{30}^2}{d_{60} \cdot d_{10}} \quad (2.5)$$



## 2 Soil Classification

### 2.5.4 Results

Figure 2.3 represents the results from sieving by plotting the fraction passing each sieve against the appropriate mesh size. The associated data are summarized in Table A.3. As expected, all samples represent sand, with a high fraction of medium sand, a small fraction of coarse sand and a very slight fraction of fine sand. As a secondary fraction, all samples consist of a fine-grained fraction between 4 – 8 %. Only sample 5590 shows a significant higher fine-grained fraction of 15 %. This might be caused by a lower depth (6,50 - 7,00 m) compared to the other samples. Nevertheless, the average amount of fine-grained fraction is less than 10 %, whereby further sedimentation is not necessary to carry out.

From Figure 2.3, it can be seen that all samples follow similar particle size distributions. Only sample 5593, from borehole S2-1, is out of place. Here the fraction of fine sand is significantly higher (30 %) than the one of the other samples. According to Section 2.1, 5593 represents the softer soil which appears with a colour of yellow to orange.

According to ISO 14688-1 and ISO 14688-2, the soil can now be described. All samples represent sand as the main fraction. Besides, it is known that the fine-grained fraction, as the second fraction, correlates with the kaolin clay. As a result, the soil describes a slightly clayed SAND (cl' Sa). Furthermore, the Coefficient of Uniformity  $C_u$  and the Coefficient of Curvature  $C_c$  give information about the grading of the particle size distribution. The sieving plots reveal  $C_u$  between 2,5 – 3,5 and  $C_c$  close to 1,0. Hence, the tested soil is uniformly to poorly graded.

To conclude, the sieving shows that the soil from both zones describes a uniformly graded, slightly clayed SAND. Therefore, the samples follow similar particle size distributions. Only, sample 5590 (S1-1, 6,50 - 7,00 m) indicates a difference in a high fine-grained fraction (15 %) and sample 5593 (S2-1, 12,00 - 12,80 m) consist of a higher fine sand fraction (30 %). Nevertheless, for the other parts, homogeneity across the depth can be assumed.

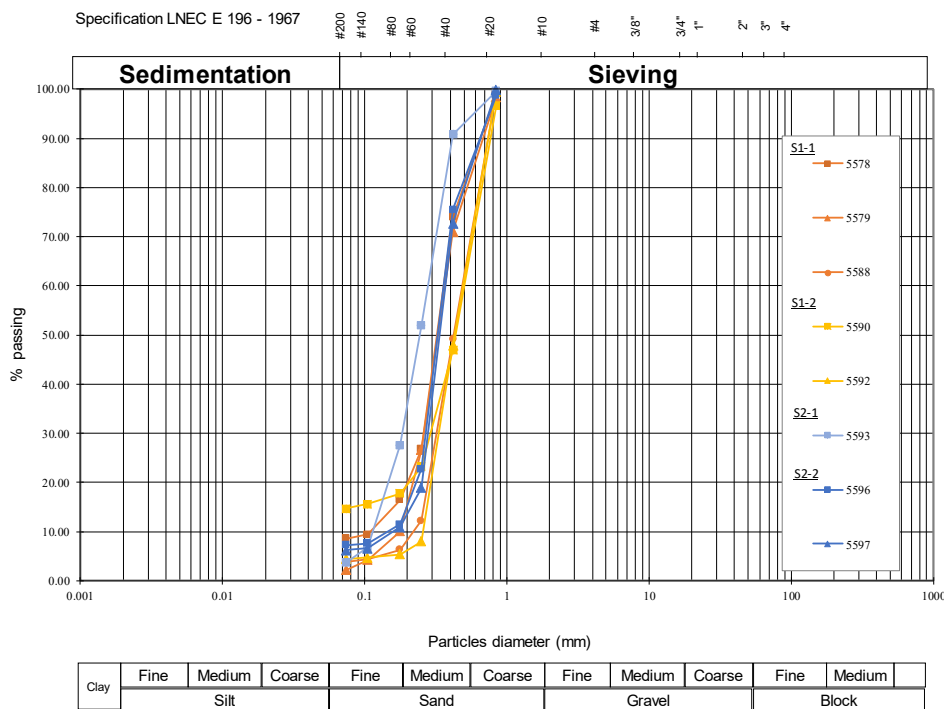


Figure 2.3: Particle size distribution plot of the tested samples

## 2.6 Conclusion

### 2.6 Conclusion

The soil classification concludes that the occurring soil, from both zones, describes slightly clayed SAND with a uniform grading. On average, the fine-grained fraction of kaolin is less than 10 %, but it does not provide plasticity since liquid and plastic limits could not be obtained. Moreover, the soils indicate a high water content of around 20 % and the average particle density equates  $2,68 \text{ g/cm}^3$ . As a result, it is expected that the in-situ soil of zone 1 shows homogeneity along the depth. In zone 2, the samples indicate differences in appearance and particle size distribution. Therefore, it is assumed that at a depth of 10 m, the soil from zone 2 coincides with zone 1. Until 10 m, zone 2 indicates a soil of a softer, yellowish appearance and a higher fine-sand fraction. Conclusions about the classification of the samples retrieved by cylindrical cutter are not provided since sieving was not performed.

### 3 Determination of the Shear Strength

Shear strength is an essential soil property, regarding the aim of this study, analysing the stability of a quarry pond slope. As shown in Section 1.5, the shear strength of soil bases on the Mohr-Coulomb criterion, representing a function of the effective normal stress  $\sigma'$ , cohesion  $c'$  and friction angle  $\phi'$ . The purpose of this Chapter is to describe the laboratory determination of the shear strength parameter by triaxial tests and direct shear tests. Both tests are the most common tests to conduct, whereby several differences influence the results.

For zone 1, one triaxial test is carried out, accompanied by several direct shear tests, aiming to obtain a range of shear strength parameters. For zone 2, only one triaxial test is intended to verify the similarities to the soil of zone 1. In the end, the results allow defining a soil model on which the subsequent slope analysis bases.

#### 3.1 Triaxial Test

Regarding the quarry pond slope in Rio Maior, the triaxial test is of prime importance, not only allowing the determination of the effective shear strength parameters but also revealing the stress-strain behaviour and the stress path during shearing. Generally, the test is carried out by placing the specimen in a triaxial cell, filled with a fluid that induces a constant confining pressure to the specimen ( $\sigma_1 = \sigma_2 = \sigma_3$ ). Meanwhile, an axial force increases until the specimen fails. For the results, it is necessary to carry out the triaxial test on three specimens of different effective stresses.

However, there are three different types of triaxial tests, the unconsolidated undrained (*UU*) tests, the consolidated undrained (*CU*) tests, and the consolidated drained (*CD*) tests. It is necessary to define the appropriate test, representing the analysing conditions. With the *UU* test, short term conditions can be examined in case of fast loading processes, when water cannot leave rapidly. Though, the slope analysis bases on long term conditions, when the soil has time to consolidate. Therefore, the *CU* test provides the best solution, obtaining the effective shear strength parameters by measuring pore water development during testing. Besides, shearing can be carried out 10 times faster compared to the *CD* test (Dohmel, 2014).

Table A.1 presents the tested sample 5578. It was collected from a depth of 13,50 - 14,10 m. For simulating realistic conditions, it is intended applying the same in-situ stress to one specimen.

##### 3.1.1 Description

The *CU* test is carried out under consolidated undrained conditions. It consists of the preparation of the specimens, followed by the three main stages: Saturation, consolidation and shearing. For every stage, different adjustment, regarding the testing devices, are applied. Therefore, it is necessary to understand all components of a triaxial apparatus and the including functions.

*LENC* is using a Triaxial Testing System by *GDS*, a load frame-based triaxial testing system allowing to compute stresses and strain during testing (GDS Instruments, 2019). The major component of the apparatus is the triaxial cell, including the load frame (Figure 3.1). The cell is connected to a tube filling the chamber with water and applying a confining pressure to the specimen. The specimen is placed in the centre of the cell. During shearing, the load frame generates a constant rate of strain by moving down. A piston, which is connected to the load frame, induces the associated axial stress to the specimen.

### 3.1 Triaxial Test

Another essential part of Triaxial Testing System is the pressure/volume controller. The system provides three controllers. One is connected to the cell chamber, controlling the confining pressure and measuring the volumetric change of water inside the cell. Another controller is connected to the bottom of the specimen, controlling backpressure and measuring the volumetric change of water inside the specimen. The last controller is connected to the top of the specimen, measuring pore pressure. Besides, a separate transducer measures pore pressure even if valves are closed. The controller consists of a cylinder, filled with de-aired water (Figure 3.2). Inside, a piston is moving against the water, by what the water generates a pressure. This process is automatically controlled, giving the possibility to apply either constant pressure or linear increase of pressure. The drainage valves, connecting the controller to the cell, stay either open or closed, depending on the stage of testing. All presented components record relevant data for the evaluation and the interpretation of the shear strength.

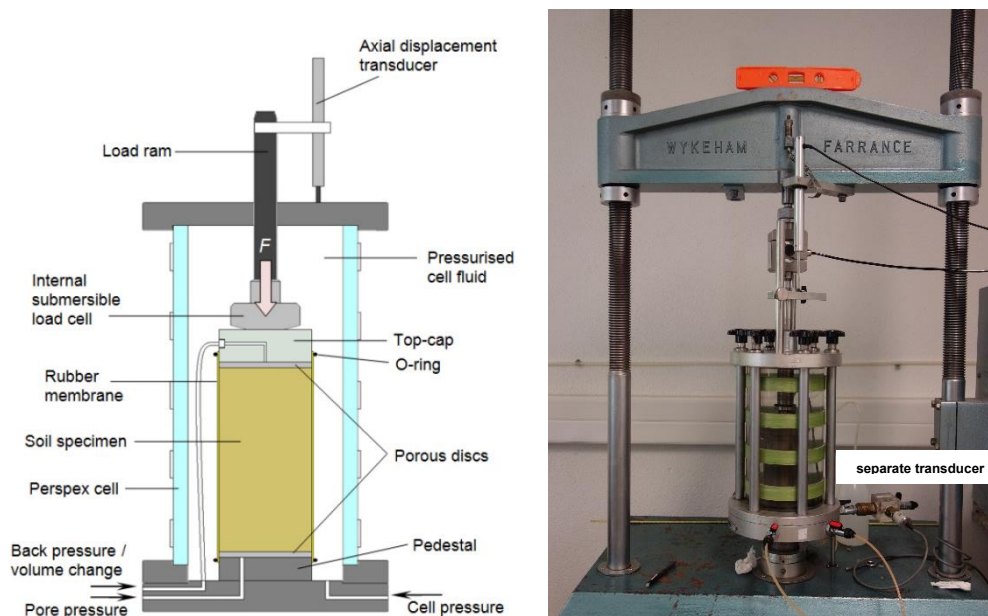


Figure 3.1: Schematic set up of the triaxial cell used for testing (Dr. Rees, 2013)

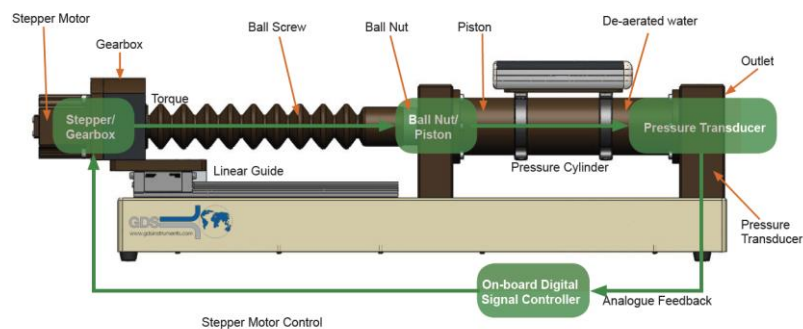


Figure 3.2: Schematic of GDS Pressure/Volume Controller used for testing (GDS Instruments, 2019)

### 3 Determination of the Shear Strength

#### 3.1.2 Test Procedure

##### 3.1.2.1 Specimen Preparation

The correct preparation of the specimens is essential to ensure accurate results. However, it is complicated to accomplish intact samples from sand since particles do not hold together well, and bonding by cementation might not appear. Therefore, the preparation must be carried out carefully to avoid disturbance.

The soil samples from the quarry pond are stored in sealed plastic tubes of a diameter of 6 cm. First, the tube, including sample, is cut by sawing into the appropriate sections of a height of 1,8 to 2.5 times the diameter (ISO 17892-9, 2018), followed by carefully extruding the specimen out of the plastic tube. At this point, the sample seems soft, with no indication of a cemented structure. Though, it was achieved to maintain three intact specimens for testing. Besides, initial documentation of the specimens allows comparisons between the appearance before and after shearing (Figure 3.3).

Afterwards, the specimen's weight, height and diameter are measured, followed by placing porous discs on top and underneath the specimen. Now, the specimen is placed centrally on the pedestal of the triaxial cell, and besides a metal top cap is placed on the specimen's top. A membrane stretcher helps to cover the specimen's surface with a membrane to prevent infiltration of cell water. Besides, snapped O-rings, on top and bottom of the specimen, generate a convenient sealing. The final steps include connecting drainage lines to the specimen, placing the piston on top, bolting the cell chamber, and finally filling water inside the cell.

At this stage, preparation is completed, and the triaxial cell can be connected to the pressure/volume controller to start the stage of saturation.

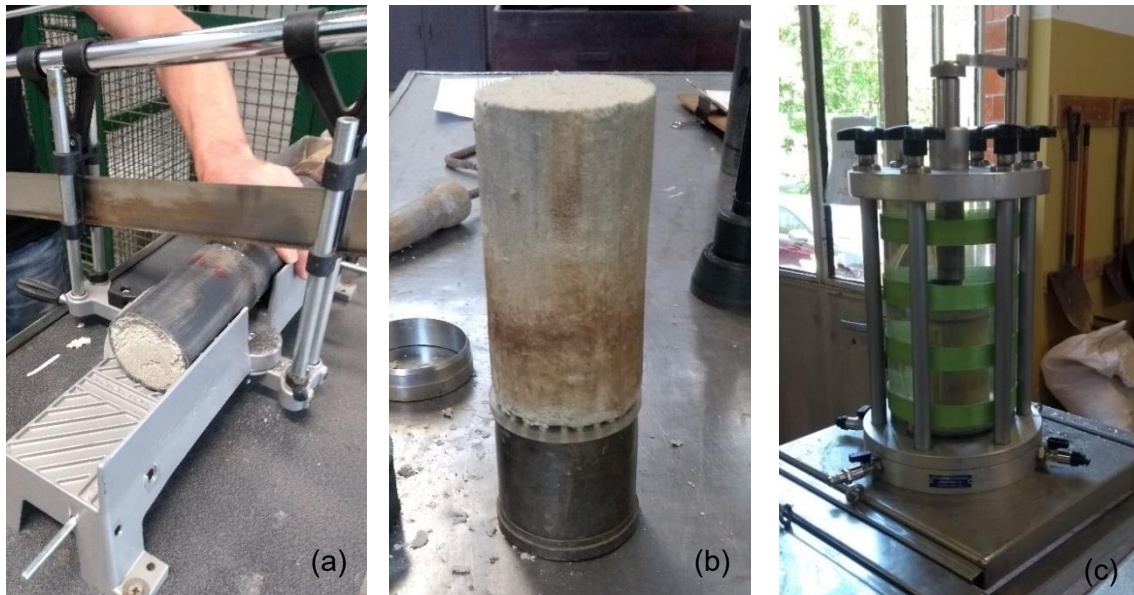


Figure 3.3: Preparation of the specimens from sample 5578 , (a) sawing in sections, (b) appearance before testing, (c) cell chamber

### 3.1 Triaxial Test

#### 3.1.2.2 Saturation

Before consolidation and shearing, it is necessary that the specimen is fully saturated to ensure all voids are filled with water. Otherwise, air voids could cause suction, and thereby, an apparent cohesion could affect the results. At first, a vacuum is applied to the drainage lines to remove surplus water and air. During saturation, the drainage valves are open while applying a linear increase of back and cell pressure to the specimen. In this connection, backpressure is defined as a hydraulic gradient inducing a pore pressure to the specimen to remove the air inside the voids. The backpressure causes unwanted swelling by what the specimen could collapse. Therefore, it is necessary to apply higher cell pressure than backpressure. The differential of both pressures equates the applied effective stress to the specimen. The stress should be constantly maintained, never exceeding the intended effective stress for consolidation. Figure 3.5 indicates the development of the applied pressures during the stage of saturation. Initially, constant pressures are maintained, whereas, after some days, a *RAMP* generates an automatic linear increase of 20 kPa per day. The differential between backpressure and cell pressure remains at 20 kPa. The *RAMP* stops by reaching a backpressure of 300 kPa and a cell pressure of 320 kPa. Besides, during testing, it is important to control the volumetric change of water inside the controller since leaks in tubes and valves could cause a limit in water by what pressure rapidly decreases.

Saturation is guaranteed by checking the *B-value*. In this connection, all valves connected to the specimen are closed, preventing drainage and maintaining constant backpressure, while an increment of 20 kPa of cell pressure is applied. As a result, the increase in cell pressure causes an increase in excess pore pressure, which is measured by a separate transducer. Therefore, the rate of change in pore and cell pressure describes the *B-Value*.

$$B = \frac{\Delta u}{\Delta \sigma_c} \quad (3.1)$$

A *B-Value* equal to 1,0 reveals that the increment of cell pressure is now entirely transmitted by pore pressure. According to ISO 17892-9, the *B-Value* must achieve at least 0,95 to ensure full specimen saturation. Nevertheless, reaching this value depends on the tested soil. Sands might reveal a *B-Value* lower than 1,0, even though full saturation is already reached (Dr. Rees, 2013)

Figure 3.4 and Figure 3.5 illustrate that saturation finished at a back pressure of 300 kPa and a cell pressure of 320 kPa. For checking the *B-Value*, an increment of 20 kPa of cell pressure was applied. Since pore pressure increased by the same amount full saturation was confirmed. Furthermore, all specimen accomplished a *B-Value* of 1.0.

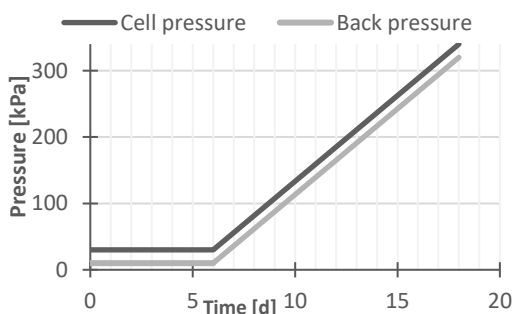


Figure 3.5: Development of pressure during saturation

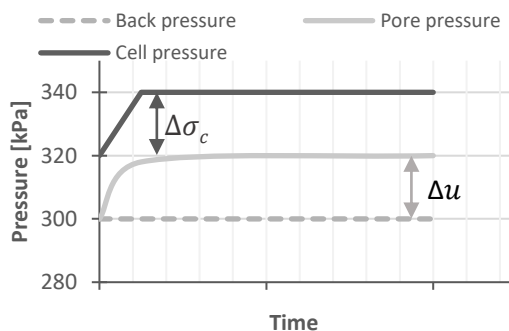


Figure 3.4: Pressure during B-Value check

### 3 Determination of the Shear Strength

#### 3.1.2.3 Consolidation

As noted, shearing is carried out on three specimens of different effective stresses. The consolidation stage is aiming to bring the specimen to the intended effective stresses. Therefore, backpressure remains constant, with the same value after saturation. Meanwhile, cell pressure increases until the difference between both pressures reach the indented effective stress. Initially, since the specimen is fully saturated, an increase of cell pressure causes an increase of pore pressure. However, since valves are open, the soil can drain, and excess pore pressure slowly releases to the amount of backpressure. Therefore, the soil is now absorbing the increase in cell pressure, which defines the effective stress.

At first, the intended effective stresses for each specimen at the end of consolidation must be defined first. Therefore, one specimen shall represent the in-situ stress of sample 5578. The stress can be easily calculated by knowing the weight and dimensions for obtaining the specimen's density.

$$\rho = \frac{m}{V} = \frac{m}{h \cdot d^2 \cdot \frac{\pi}{4}} \quad (3.2)$$

$$\gamma = \rho \cdot g \quad (3.3)$$

As a result, the average unit weight of the specimen equates:

$$\gamma = 21 \text{ kN/m}^3$$

Besides, it is known that the water table lays below the depth of the sample, so that pore pressure is not considered.

Therefore, the effective stress is calculated from:

$$\sigma' = 13,5 \text{ m} \cdot \gamma \approx 280 \text{ kPa} \quad (3.4)$$

Regarding the other specimens, it is intended, applying a mainly higher and lower effective stress, aiming to achieve a reasonable range of stresses. Table 3.1 shows the relevant data for the stage of consolidation. According to that, the cell pressure increases with a *RAMP*. This procedure has the advantage that excess pore pressure does not appear since the rate of stress is low. In this connection, at every stage of consolidation, the effective stress is equal to the applied stress.

Table 3.1: Applied stresses for consolidation stage

Sample 5578, S1-1 (13.50-14.10 m)			
Cell pressure at the end of saturation $\sigma_c=340 \text{ kPa}$	Backpressure at the end of saturation $\sigma_B=320 \text{ kPa}$		
	specimen 1	specimen 2	specimen 3
effective stress $\sigma'$	50 kPa	280 kPa	500 kPa
Target cell pressure $\sigma_c$	370 kPa	600 kPa	820 kPa
RAMP [ $\text{kPa/d}$ ]	10	20	30

### 3.1 Triaxial Test

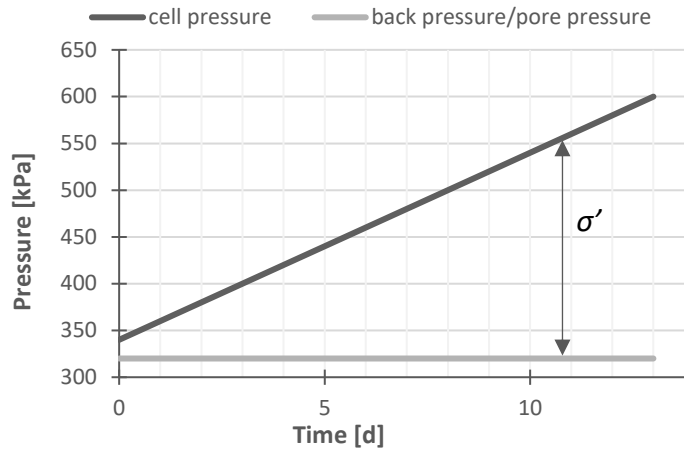


Figure 3.6: Process of consolidation for specimen 500 kPa

Besides, during consolidation, the volumetric change of the specimen must be controlled. It correlates with the amount of water, squeezed out within the specimen. The control of volumetric change is an important indicator to determine the end of consolidation since, according to *ISO 17892-9*, completed consolidation can be guaranteed when the change of volume is less than 0,1 % per hour and excess pore pressure dissipated to 0,95 %. Nevertheless, concerning the procedure of sample 5578, the end of consolidation can be guaranteed by the end of the *RAMP* when the difference between cell and backpressure equates the required stress.

Additionally, the vertical strain caused by consolidation is measured. Due to the displacement, a slippage between the specimen's top cap and the piston emerges. Adjusting the piston to the top cap and measuring the difference before and after consolidation allows determining the value of vertical strain.

All data recorded during saturation and consolidation are presented in the associated Datasheets in Annexe B.

#### 3.1.2.4 Shearing

Shearing is the final stage and the most significant for triaxial testing aiming to determine the soil's shear strengths. The test is strain-controlled by a load frame moving with a constant rate of vertical displacement and inducing a constant rate of axial strain. During shearing, cell pressure and backpressure remain at the same value from the end of consolidation. Besides, this stage is carried out undrained, so that valves to the specimen are closed. Since undrained conditions cause an increase of pore pressure, it is essential that pore pressure distributes equally within the specimen. This is accomplished by adjusting a rate of vertical displacement, slowly enough, that pore pressure occurs equally. Usually, the rate of displacement is determined from a plot of volume against the consolidation time, recorded during consolidation. According to *ISO 17892-5*, the consolidation time,  $t_{100}$ , defines a maximum velocity for the load frame. Though, the plot can only be obtained by applying stress in one increment and recording the volumetric change until consolidation finishes. Since consolidation was accomplished by adjusting a *RAMP*, the rate of the load frame must be estimated. According to that, *LNEC* provides a standard rate of 0,05 mm/min. Sand is a coarse soil and referring to the rate of displacement for the direct shear test, 0,5 mm/min (drained test) (Dohmel, 2014), it is



### 3 Determination of the Shear Strength

evident that shearing could be carried out faster. Nevertheless, a rate of  $0,05 \text{ mm/min}$  ensures confidentially that pore pressure distributes equally.

During testing, a computer plots the essential strain-stress behaviour, recording data every  $60 \text{ sec}$ . The test finishes when failure is evident, and the plot of axial strain against deviator stress approaches a plateau. The associated Datasheets, presented in Annexe B, indicate measurements of every  $20 \text{ min}$ .

#### 3.1.3 Test Procedure of the Sample of Zone 2

For sample 5593 ( $12 - 12.8 \text{ m}$ ) from zone 2, the same procedure for testing was carried out. However, some differences in soil behaviour were detected. At first, the soil appeared soft like a sponge, with a different colour and a higher saturation, compared to the sample from zone 1. It is assumed that the process of retrieving by borehole already disturbed the soil since the sample and tube were not flush with each other (Figure 3.7). Moreover, all specimen showed a low density of around  $1,7 \text{ g/cm}^3$ , which does not coincide with the *SPT* results.

For the stage of saturation, higher final back and cell pressure were necessary compared to sample 5578 from zone 1. The values for consolidation are presented in Table 3.2. Specimen  $250 \text{ kPa}$  represents the in-situ effective stress. Shearing was conducted with the same rate of strain of  $0.05 \text{ mm/min}$ . As a result, the essential plots illustrate lower peak stresses with a nonlinear distribution (see Section 3.1.6). Besides Specimen  $500 \text{ kPa}$  indicated a local disturbance after consolidation. Hence, the specimen did not deform uniformly so that results are unusable.

Assuming that sample 5593 does not represent the actual soil from zone 2, another triaxial test was intended to perform. However, finding intact samples from borehole S2-1 was not achieved since the same soft and yellow soil continued until the final depth of  $18 \text{ m}$ . Only sample 5597 (S2-2,  $18 - 19 \text{ m}$ ) showed similarities to the soil from zone 1 by having the same white colour and a density of  $2.0 \text{ g/cm}^3$  (Figure 3.8). It was achieved to assemble three intact specimens. Table 3.3 presents the stresses, applied for consolidation. Due to technical problems, the project can only include the shearing of the specimen of  $50 \text{ kPa}$ . The associated results are presented in Annexe B.

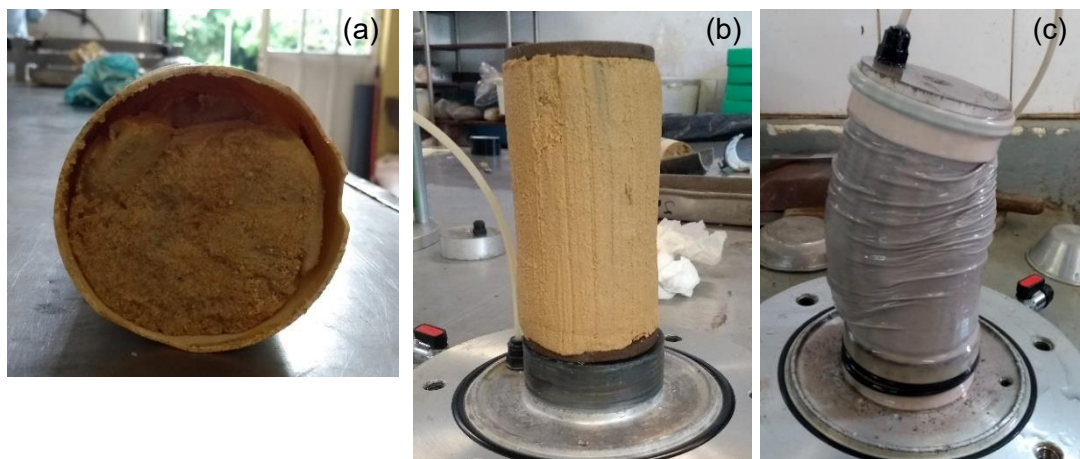


Figure 3.7: Appearance of sample 5593, (a) in the tube, (b) before shearing, (c) after shearing

### 3.1 Triaxial Test

Table 3.2: Values for consolidation from a sample 5593 of zone 2

Cell pressure at the end of saturation $\sigma_c = 380$ kPa	Backpressure at the end of saturation $\sigma_B = 370$ kPa		
	specimen 1	specimen 2	specimen 3
effective stress $\sigma'$	50 kPa	250 kPa	500 kPa
Target cell pressure $\sigma_c$	420 kPa	630 kPa	870 kPa
RAMP [kPa/d]	20	30	40



Figure 3.8: Appearance of sample 5597 before testing

Table 3.3: Values for consolidation from a sample 5597 of zone 2

Cell pressure at the end of saturation $\sigma_c = 320$ kPa	Backpressure at the end of saturation $\sigma_B = 310$ kPa		
	specimen 1	specimen 2	specimen 3
effective stress $\sigma'$	50 kPa	360 kPa	500 kPa
Target cell pressure $\sigma_c$	360 kPa	670 kPa	810 kPa
RAMP [kPa/d]	25	60	80

#### 3.1.4 Calculations

During shearing, a computer records the pore pressure  $u$ , the axial displacement  $\Delta v_1$ , and the axial force  $F$ . Those data allow further calculations to evaluate the triaxial test. The specimen performs axial strain by maintaining a constant volume. This behaviour causes a radial extension, and therefore, the specimen's section changes as well. However, a radial strain is not measured directly during shearing, but it infers from the axial strain, allowing to calculate the corrected specimen section  $A_c$ , and furthermore the state of axial stress  $\sigma_1$  (major principle stress), at every stage of testing.

Axial strain:

$$\Delta \varepsilon_1 = \frac{\Delta v_1}{H_0} \quad (3.5)$$

### 3 Determination of the Shear Strength

Corrected specimen section:

$$A_c = \frac{A_0}{(1 - \Delta\varepsilon_1)} \quad (3.6)$$

State of axial stress:

$$\sigma_1 = \frac{F}{A_c} \quad (3.7)$$

Since the test is undrained, pore pressure occurs. Recording pore pressure during shearing allows obtaining principal effective stresses.

Major principle effective stress:

$$\sigma'_1 = \sigma_1 - u \quad (3.8)$$

Minor principal effective stress:

$$\sigma'_3 = \sigma_3 - u \quad (3.9)$$

Additionally, stress paths are illustrated from the Cambridge stress path plot  $p'$ - $q$ .

$q$  is the deviator stress representing the Y-axis

$$q = \sigma_1 - \sigma_3 \quad (3.10)$$

$p'$  is the mean effective stress or hydrostatic stress representing the X-axis.

$$p' = \frac{\sigma'_1 + 2 \cdot \sigma'_3}{3} \quad (3.11)$$

#### 3.1.5 Results of Sample 5578 of Zone 1

##### 3.1.5.1 Failure Mode

All specimen from zone 1 followed a barrelling failure mode during shearing. Figure 3.9 indicates that the most considerable radial strain appeared in the specimen mid-height, whereas at the edges, friction between the specimen and the top cap prevented radial strain. Specimen 280 kPa and 500 kPa indicate an explicit shear zone which occurred after the specimens underwent a great axial strain of around 25 - 30 %. Specimen 50kPa only indicates barrelling, but no shear zone, since the test stopped a 20 % axial strain.

### 3.1 Triaxial Test



Figure 3.9: Specimen appearance after shearing (left 50 kPa, middle 280 kPa; left 500kPa)

#### Stress-Strain Behaviour

Figure 3.10 shows the deviatoric stress  $q$  plotted against the axial strain  $\varepsilon_1$  for the specimens of zone 1. The associated values are presented in Table 1.1. With increasing confining pressure, the associated peak strength increases as well. For all specimens, a clear peak can be seen, followed by a decrease till the curve reaches a plateau, and axial strain is carried out under constant deviator stress. Specimen 500 kPa shows a distinct, clear peak followed by a fast fall reaching the plateau. The curves of specimen 50 kPa and 280 kPa are approaching the peak gradually and decreasing slightly till the curves remain constant.

The associated axial strains at the peak points distinguish for the three specimens. Specimen 500 kPa generates the peak at a lower axial strain, and the rate of reaching the peak is higher compared to the other specimen. The curves of 50 kPa and 280 kPa superpose at first but fail both at a different axial strain.

The plateau correlates with the critical state when deformation takes place under constant stress and volume. Here, 500 kPa generates the constant level by fluctuation and at a lower axial strain, whereas the other specimens reach that level at a higher axial strain of more than 20 %. Specimen 50 kPa stops before reaching a clear plateau. However, it is assumed that the ending point already indicates the critical state.

Figure 3.11 shows the stress ratio ( $p/q$ ) plotted against the axial strain. The stress ratio infers from the mobilised friction angle  $\phi'$ . The maximal mobilised stress ratio for all specimens is generated fast, within the first 7 % of axial strain. Only 500 kPa generates the maximal stress ratio at the same time as reaching the peak of deviator stress. For specimen 50 kPa and 280 kPa, the maximal stress ratio is approached earlier, remaining nearly constant until reaching the peak deviator stress and decreasing to the plateau. However, all specimens generate similar peak and critical stress ratios.

The reason for the different stress-strain behaviour of specimen 500 kPa might be higher confining stress, which prevents initial axial strain. As Figure 3.10 illustrates, an initial jump of deviator stress is necessary to perform axial strain. Therefore, the curve does not superpose with the other specimen's curves, but the inclination appears similar.

### 3 Determination of the Shear Strength

Table 3.4: Essential data from *CU*-test according to the stress-strain behaviour

Specimen	peak				critical			
	Deviator stress		Stress ratio		Deviator stress		Stress ratio	
	$q$ [kPa]	$\epsilon_1$ [%]	$p/q$	$\epsilon_1$ [%]	$q$ [kPa]	$\epsilon_1$ [%]	$p/q$	$\epsilon_1$ [%]
<b>50 kPa</b>	1287	10.5	1.55	5.6	1106.5	$\geq 20$	1.4	$\geq 20$
<b>280 kPa</b>	1823	13.3	1.47	5.4	1502.5	30	1.32	30
<b>500 kPa</b>	2511	7.5	1.51	7.5	2202	$\approx 13.5$	1.35	$\approx 13$

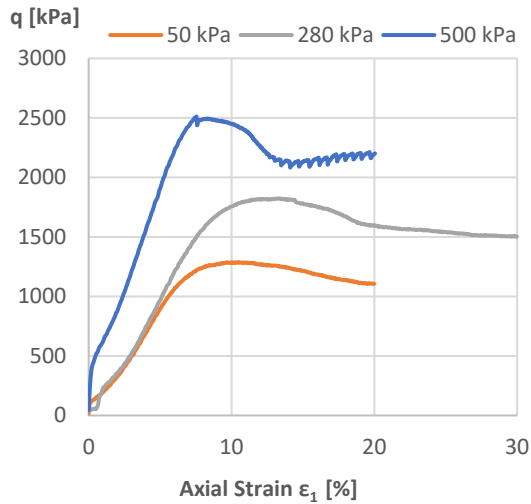


Figure 3.10: Deviatoric stress-axial strain behaviour of sample 5578 from zone 1

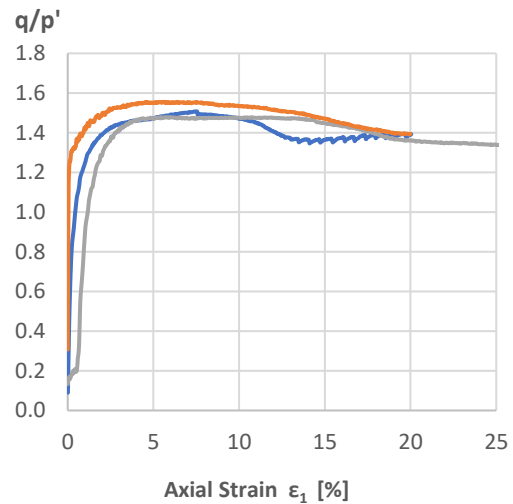


Figure 3.11: Stress ratio – axial strain behaviour of sample 5578 from zone 1

#### 3.1.5.2 Pore Water Pressure Development

Figure 3.12 represents the pore pressure development during shearing of the specimens from zone 1. As already described, since the test was carried out undrained, pore water inside the specimen cannot leave, whereas excess pore pressure appears. It is important to emphasise that constant backpressure during shearing is maintained. Hence, the actual pore pressure is the difference between backpressure and the recorded pore pressure.

The curve from *50 kPa* indicates an initial decrease to negative pressure until reaching a constant level. On the contrary, *280 kPa* and *500 kPa* generate positive pore pressures immediately, reaching a peak and afterwards falling with a high rate towards negative pressure until remaining on a constant level. Therefore, negative pore pressure dominates positive pore pressure.

The curves from Figure 3.12 infer from the soil's behaviour of dilatancy. Generally, soils change in volume during shearing. Therefore, the material either contracts by reducing the volume or expand by increasing the volume. However, the undrained condition prevents a change in volume. Hence, when the soil intends to contract, the soil's grains try to compromise pore water, but since water is incompressible, positive pore pressure is generated as an interaction. On the other hand, when the soil intends to expand, pore water cannot distribute, causing negative pore pressure (Wood, 1990). As a result, positive pore pressure correlates with contraction, whereas negative pore pressure correlates with dilatancy.

### 3.1 Triaxial Test

According to the curves from Figure 3.12, at first, specimen 500 kPa and 280 kPa are willing to contract, but after small strain, they intend to perform dilatancy, while specimen 50 kPa only indicates dilatancy. This behaviour is associated with higher confining pressure, which suppresses dilatancy by crushing the soil (Lade, et al., 2014).

Furthermore, the results are related to Figure 3.10. For all specimens, the peak strength is approached by performing dilatancy. At the peak stress ratio ( $p'/q$ ), the soil generates the highest rate of dilatancy. From Figure 3.13, it can be seen that this rate correlates with the turning point of pore pressure when the curve approaches the constant level. In contrast, at the critical state, dilation disappears, and shearing is carried out at constant volume.

As a result, the presented pore pressure behaviour for the *CU* test correlates with shearing behaviour of dense sands, confirming the results from the *SPT*.

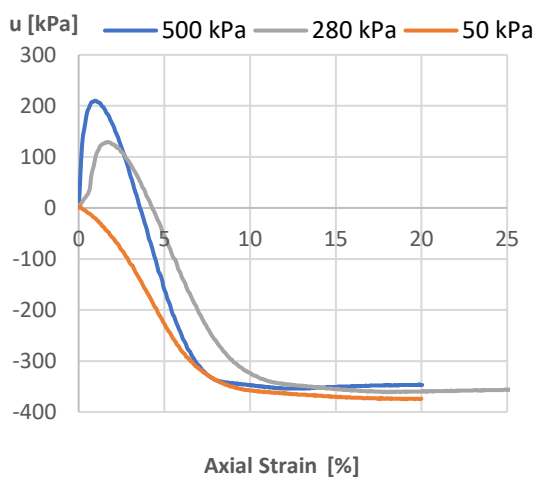


Figure 3.12: Pore pressure - axial strain behaviour of sample 5578 from zone 1

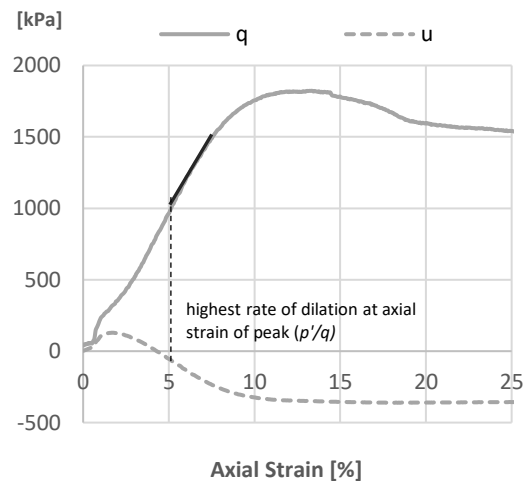


Figure 3.13: Peak strength – dilatancy behaviour for specimen 280 kPa

#### 3.1.5.3 Stress Path

Figure 3.14 represents the effective stress path  $p'-q$  of sample 5578. All curves start from a different mean effective stress  $p'$  while ending on the same linear line, but reaching the peak at a different deviator stress  $q$ . After peaking, the curves fall to the critical stress, where  $p'$  and  $q$  remain constant. According to Figure 3.14, the stress path reveals that a constant stress ratio ( $p'/q$ ) is generated rapidly since all curves follow a straight line after a small increase of stresses.

Figure 3.15 assembles the effective and total stress path of specimen 500 kPa. The curves are demonstrating pore pressure development during testing. At the point where the effective stress path intersects the total stress path, the total amount of pore pressure turns from positive to negative.



### 3 Determination of the Shear Strength

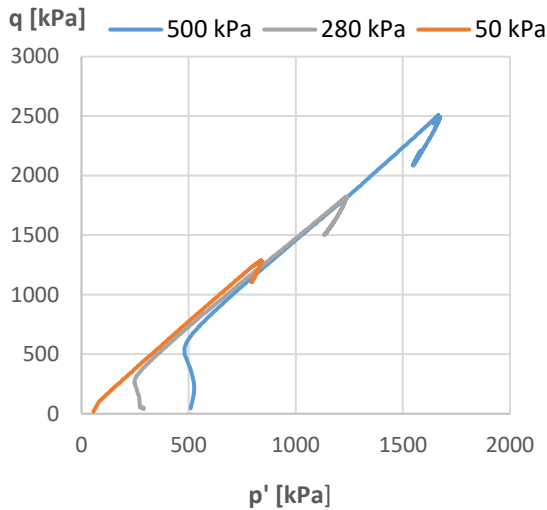


Figure 3.14:  $p'$ - $q$  plot of sample 5578 from zone 1

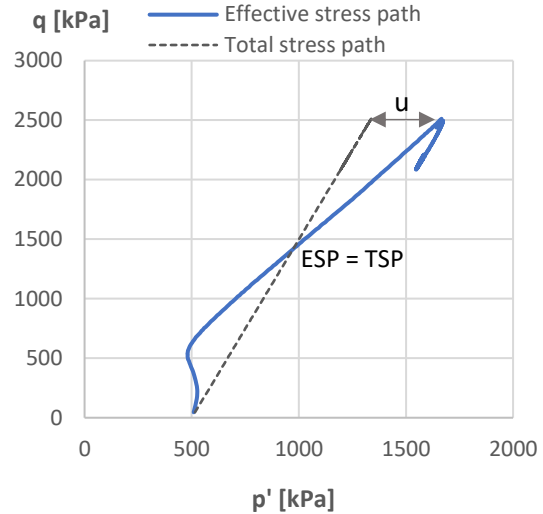


Figure 3.15: Pore pressure development of specimen 500 kPa

#### 3.1.5.4 Failure Envelope

Plotting the peak deviator stress against the associated mean effective stress of each specimen and approximating all points to a linear line allows obtaining the failure envelope for the  $p'$  -  $q$  plot. The failure envelope can be transformed into the Mohr-Coulomb criterion. In this connection, the effective friction angle  $\phi'$  and the effective cohesion  $c'$  are calculated from the gradient of the failure envelope  $M$ , according to formula (3.12), (3.13) and (3.14).

$$M = \frac{\delta q}{\delta p'} \quad (3.12)$$

$$\sin \phi' = \frac{3 \cdot M}{6 + M} \quad (3.13)$$

$$c' = \frac{q_0 \cdot \tan \phi'}{M} \quad (3.14)$$

Figure 3.16 and Figure 3.17 present the  $p'$ - $q$  failure envelope of sample 5578. Figure 3.16 defines the linear approximation with the highest correlation. In this case, the line intercepts the y-axis at  $q_0$ , which means cohesion exists whereas, for the second case from Figure 3.17, the assumption is made that cohesion equates zero by what the line crosses the origin. Table 3.5 represents the results of both cases, according to the Mohr-Coulomb criterion. The effective peak friction angles slightly distinguish. The correlation,  $R^2$ , for both approximations, approaches a value close 1.0. Hence, both figures represent adequate results.

Cohesion defines the strength a soil can mobilise without performing interparticle friction. Generally, sands are cohesionless, but some properties, such as very high

### 3.1 Triaxial Test

density and interlocking, can cause an interception with the y-axis so that an apparent cohesion appears. Besides, it is assumed that the soil shows a cemented structure. Therefore, cementation would reveal a 'real cohesion' due to particle bonding. Nevertheless, a definite tendency of cohesion in Figure 3.17 is not indicated, which leads to the conclusion to neglect cohesion, concerning the shear strength.

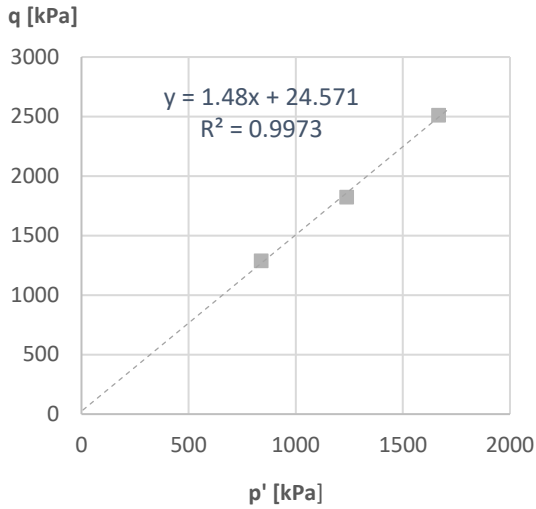


Figure 3.16: Failure envelope with the highest correlation,  $c' \neq 0$  of sample 5578

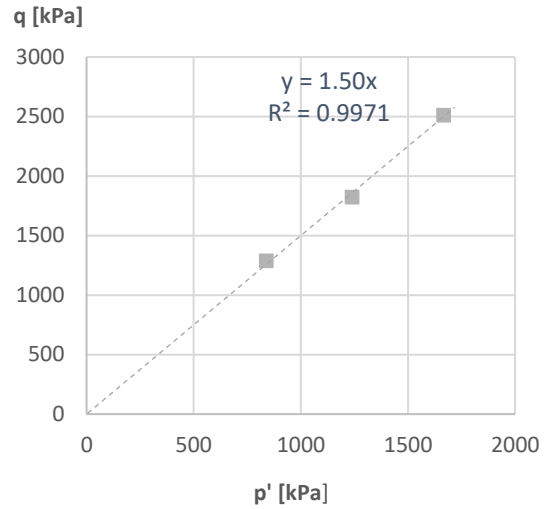


Figure 3.17: Failure envelope for the assumption that  $c' = 0$  of sample 5578

Table 3.5: Evaluation  $p'$ - $q$  plot to Mohr-Coulomb failure criteria

	$M$	$\varphi'_{peak}$	$c'$
Figure 3.16	1.48	$36.45^\circ$	30 kPa
Figure 3.17	1.5	$36.85^\circ$	0

According to Section 3.5, the Mohr circles of each specimen are illustrated in Figure 3.18, allowing to determine the shear stress  $\tau$  and the effective stress  $\sigma'$  along the failure plane, as well as the orientation of failure plane  $\vartheta_a$ . The failure envelope is precisely tangent to the three circles, inclining with the same peak friction angle of  $37^\circ$  by intercepting the coordinate origin. The contact point between each circle and the envelope defines the shear stress and the associated normal stress at failure. Figure 3.18 shows the state of stresses at failure for specimen 280 kPa.

The associated direction of the failure plane can be calculated from (3.15). Thus, all circles show the same direction of the failure plane but fail at different states of stress.

$$\vartheta_a = 45^\circ + \frac{\varphi}{2} \quad (3.15)$$

As a result, the peak shear strength is defined, according to the Mohr-Coulomb criterion, as:

$$\tau = \sigma' \cdot \tan 37^\circ \quad (3.16)$$



### 3 Determination of the Shear Strength

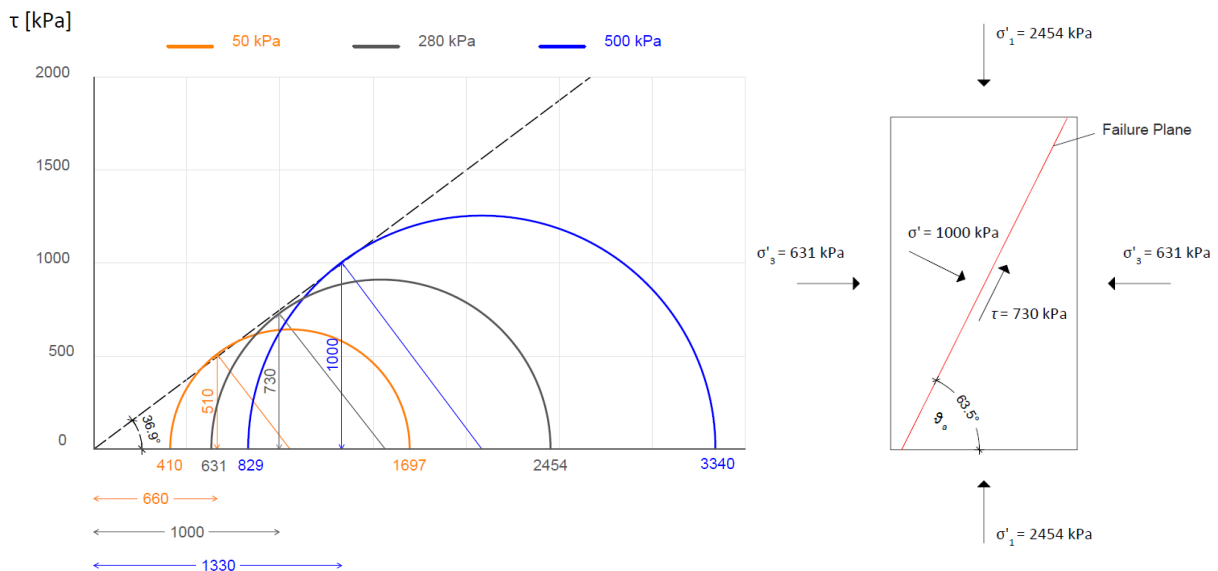


Figure 3.18: Mohr's Circle plot for sample 5578 and state of stress at failure for specimen 280 kPa

Besides, the stress path from Figure 3.14 allows determining the critical state envelope. At critical state, axial strain is performed under constant stresses and volume. According to that, the critical points of deviator stress are plotted against the associated mean effective stress. Connecting the three points to one line obtains the critical line, represented in Figure 3.19. The line must intercept the origin since at critical state cohesion does not appear. By transforming Figure 3.19 into the Mohr-Coulomb criterion, the critical shear strength is defined as:

$$\tau = \sigma' \cdot \tan 34^\circ \quad (3.17)$$

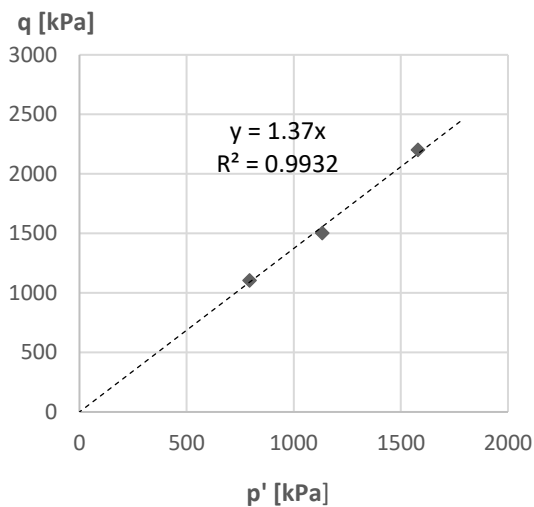


Figure 3.19: Failure envelope for the critical state of sample 5578 from zone 1

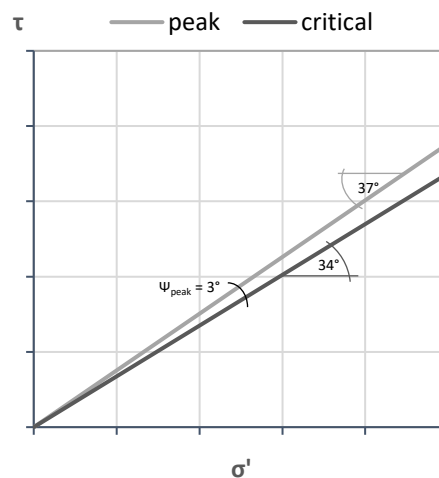


Figure 3.20: Mohr-Coulomb envelope for peak and critical strength

### 3.1 Triaxial Test

Figure 3.20 assembles the peak and critical envelope, according to Mohr-Coulomb. It can be seen that the peak friction angle  $\phi'_{peak}$  is composed of the critical friction angle  $\phi'_{crit}$  and an additional angle  $\psi_{peak}$ . The value of  $\psi_{peak}$  is associated with the ability to perform dilatancy during shearing. Hence, according to Figure 3.12,  $\psi_{peak}$  starts to mobilise from the peak of pore pressure. Transferring this point to the stress path of each specimen gives the characteristic line (Lade, et al., 2014), shown in Figure 3.21 and Figure 3.22. This line describes the intersection between contraction and dilatancy. The corresponding angle coincides with the critical friction angle  $\phi'_{crit}$ , but the state is reached at a lower axial strain. Till peaking further shear strength is only mobilised by dilation or by  $\psi_{peak}$ .

It must be emphasised that neither  $\phi'_{peak}$  nor  $\psi_{peak}$  is an accurate soil parameter since they variate due to different density. Besides, high confining pressure suppress dilatancy, causing a lower peak friction angle (Kolymbas, 2016). However, the critical friction angle describes a real soil parameter since the same soils of different densities can mobilise it.

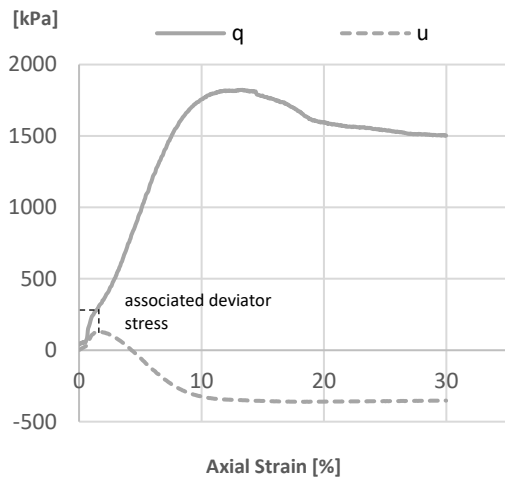


Figure 3.21: Associated deviator stress at the turning point from contraction to delation of specimen 280 kPa

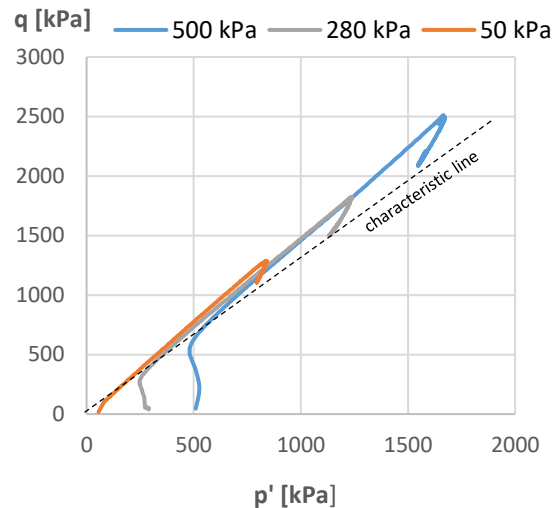


Figure 3.22: Characteristic line of sample 5578

#### 3.1.6 Results of Sample 5593 and Sample 5597 from zone 2

As described before, due to a local disturbance, specimen 500 kPa underwent a non-uniform deformation. For this reason, only the results of specimen 50 kPa and 280 kPa are evaluated below.

All specimens followed a barrelling failure mode with no appearance of a shear plane (Figure 3.23). The stress-strain behaviour from Figure 3.24 reveals that all specimens underwent a significant high axial strain of 25 % until reaching the highest deviator stress, whereas a clear peak is not indicated. Additionally, compared to sample 5578 from zone 1, the lines increase with a lower rate by reaching lower peak values. Finally, the critical state might not be approached since none of the lines shows a definite plateau.

### 3 Determination of the Shear Strength

Figure 3.25 indicates that the maximal stress ratio ( $p'/q$ ) is mobilised immediately, followed by a direct decrease. As a result, the points of the peak stress ratio ( $p'/q$ ) and peak deviator stress  $q$  do not coincide.

The pore water pressure development from Figure 3.26 reveals that specimens  $50\text{ kPa}$  and  $280\text{ kPa}$  show a tendency of dilatancy. Hence, compared to sample 5578, dilatancy is carried out with a lower rate. This behaviour confirms the lower density of sample 5593 than sample 5578.

In Figure 3.27, the stress paths of specimen  $50\text{ kPa}$  and  $280\text{ kPa}$  follow the same straight line after an immediate small increase of stresses. The associated failure envelope of peaking shows an excellent approximation to the peak points ( $R = 1$ ) by intercepting the origin. Hence, apparent cohesion does not appear. Besides, the critical state follows nearly the same envelope than the peak state. Therefore, the peak and critical friction angle equate  $29^\circ$ , according to Mohr-Coulomb. However, the peak stress ratio ( $p'/q$ ) mobilises a friction angle of  $33^\circ$ . The difference between both angles is caused by dilatancy. Until reaching the peak deviator stress, the rate of dilatation is already decreasing, and therefore, the soil mobilises a smaller friction angle at peak stress. Hence, the associated envelope of peak stress ratio can also represent the peak shear strength, depending on the definition.

Nevertheless, the critical friction angle  $\phi'_{crit}$  is a better indicator, regarding the shear strength, representing a real soil propriety. According to that, the results of sample 5598 reveal a  $5^\circ$  lower critical friction angle than for sample 5578 from zone 1. Therefore, both soils do not coincide in shear strength. For this reason, a second test from the soil of zone 2 was carried out on sample 5597. However, the project only includes the results of specimen  $50\text{ kPa}$ . They are presented in Annexe A, Figure A.3 - Figure A.6, with a comparison to the results of specimen  $50\text{ kPa}$  of sample 5578. The plots reveal similar shearing behaviour and stress ratio ( $p'/q$ ). It concludes that both samples coincide in shear strength.



Figure 3.23: Specimen  $280\text{ kPa}$  of sample 5593 after shearing

### 3.1 Triaxial Test

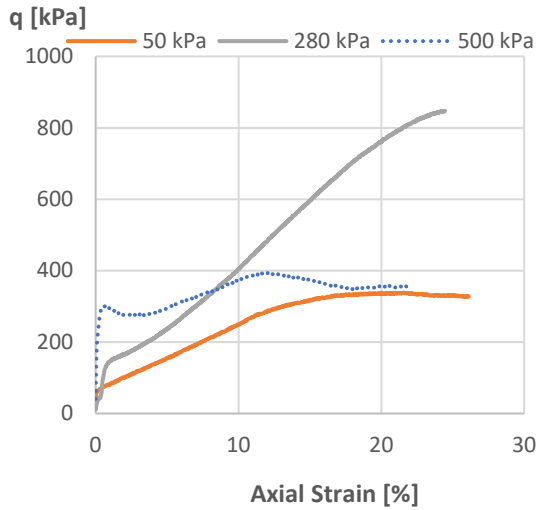


Figure 3.24: deviatoric stress-axial strain behaviour of sample 5593 from zone 2

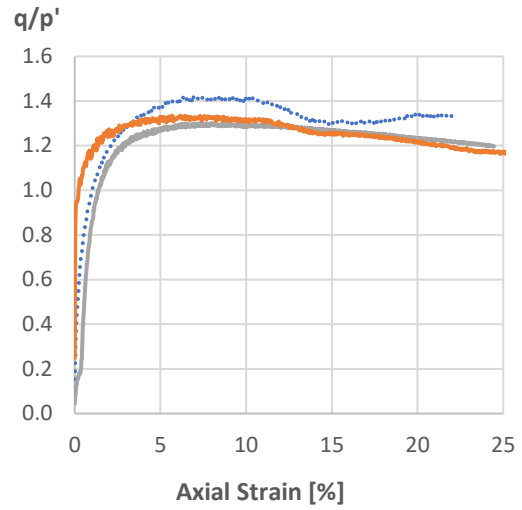


Figure 3.25: Stress ratio – axial strain behaviour of sample 5593 from zone 2

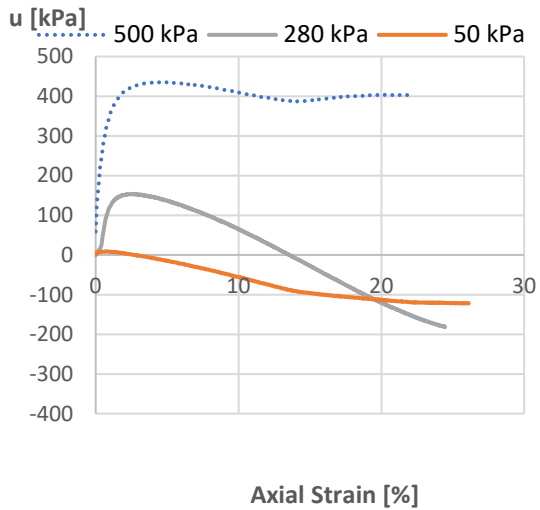


Figure 3.26: Pore pressure - axial strain behaviour of sample 5593 from zone 2

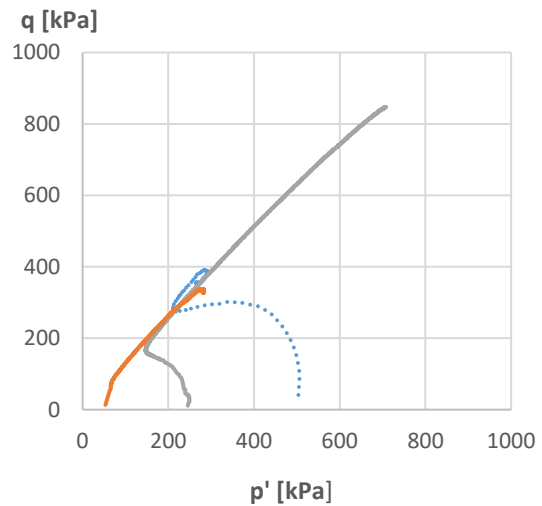


Figure 3.27: p'-q behaviour of sample 5593 from zone 2

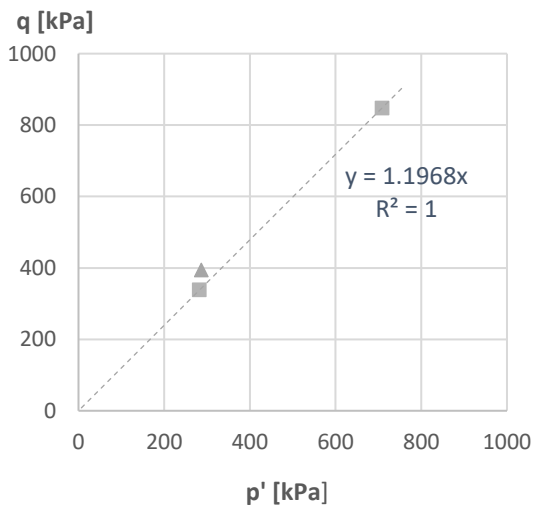


Figure 3.28: Peak failure envelope of sample 5593

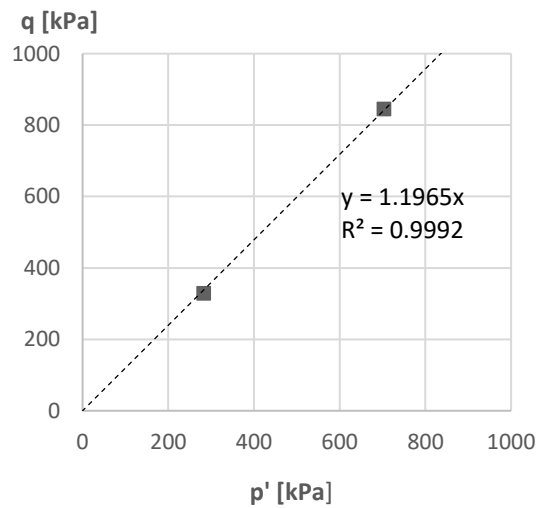


Figure 3.29: Critical failure envelope of sample 5593

### 3 Determination of the Shear Strength

#### 3.1.7 Source of Errors

The triaxial test attains to perform uniform deformation of the specimen during shearing to determine the appropriate state of stress. Therefore, a standard procedure is to carry out the test with compact dimensions ( $D:H = 1:1$ ) and with lubricated ends to eliminate friction between the specimen and the cell's plates. Though, for testing the samples from Rio Maior, no lubricated ends were used by what lateral restraint developed at the specimens ends. Slender specimen dimensions ( $D:H = 1:3$ ) attain to minimise the influence of friction at the specimen's mid-height that deformation appears homogeneous there (Kolymbas, 2016). However, since dimensions of  $1:2$  were used, it can be assumed that friction had an impact on the specimen's mid-height deformation. This can also be seen from the specimen's formation after shearing, which appears barrel-shaped (Figure 3.30). If the failure occurs at small axial strain, it is assumable that the impact of friction is small (Rackwitz, 2005). Though, the specimen already underwent considerable axial strain at failure. At the critical state, axial strain approached nearly 20 %, accomplished by a high deformation. For this reason, the calculated state of stress at the critical state might distinguish from the actual since the deformation was apart from a homogenous cylinder.

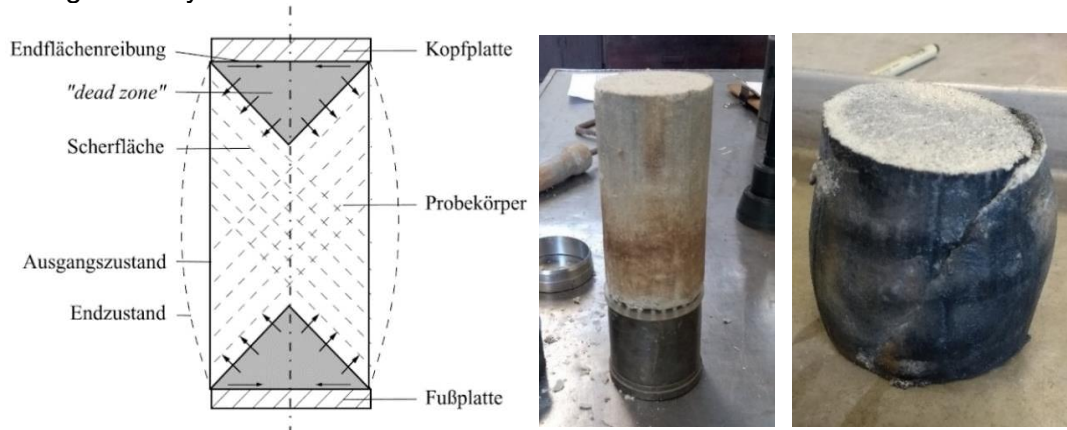


Figure 3.30: Influence of friction between the specimen's ends (Rackwitz, 2005), Deformation during testing: from cylindrical to barrel-shaped.

#### 3.2 Direct Shear Test

The triaxial test obtained precise results, but it is a time-consuming, expensive test. However, since more results for the shear strength of the soil from zone 1 are requested, it is intended to perform further direct shear tests for having a comparison and assessment regarding the triaxial results from zone 1. Besides, it is expected that the direct shear test reveals more about an eventual effect of cementation since it is assumed that soil sampling by cylindrical cutters is less disturbing than retrieving by a borehole.

Compared to the *CU* test, the direct shear test is fast and simple to run, and the data are easy to grasp. It is a drained test giving a proper estimation regarding the effective shear stress parameters but also allowing to infer from the tendency of dilatancy during shearing. In the direct shear test, the specimen is placed inside a shear box of a square cross-section or a circular cross-section. The box is divided in the middle into two separate frames. Shearing is carried out under a constant rate of displacement by moving one frame against the other one, whereas the dividing horizontal defines the shear plane. Thereby, shear stress and normal stress are directly applied to the failure plan, allowing an immediate measurement without any further calculations. Besides, it is a drained test, and the specimen must be saturated to ensure that suction does not affect

## 3.2 Direct Shear Test

the results. As per description for the triaxial test, the direct shear is performed on one sample but under three different normal stresses, allowing to determine the shear stress parameter from the Mohr-Coulomb criterion, according to Section 1.5.

### 3.2.1 Test Procedure

#### 3.2.1.1 Specimen Preparation

Table A.1 presents the tested samples, which were collected by cylindrical cutters in a low depth close to the surface and are now stored in sample containers. Figure 3.32 indicates the specimen preparation. At first, the sample must be extruded carefully from the container. Afterwards, a cutter of  $60 \times 60 \text{ mm}$  is pushed into the soil, by placing a second cutter above. The surrounded soil can now be excavated, followed by extracting the cutter and trimming the specimen until the surface is plane and flush. Finally, the specimen is placed into the shear box by extruding it carefully with a piston from the cutter, followed by putting the shear box into the loading device.

Figure 3.31 indicates the shear box, used for testing. The specimen inside the box is placed between porous discs, to enable drainage, and shear friction plates. The relief of the friction plate is perpendicular to the direction of the shear plane to ensure proper friction. Besides, specimen saturation is accomplished by filling the outer container with water. Before testing the specimen's initial dimensions, bulk density and water content are determined.

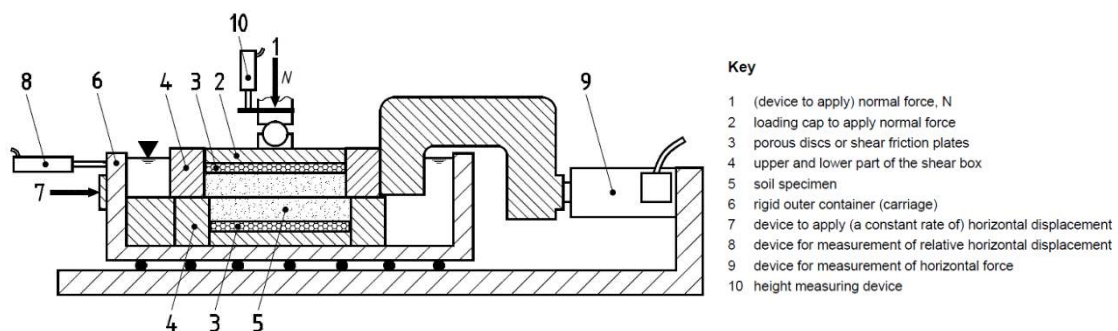


Figure 3.31: Shear box apparatus (ISO 17892-10, 2018)



Figure 3.32: Specimen preparation for the direct shear test

## 3 Determination of the Shear Strength

### 3.2.1.2 Consolidation

Before shearing, the three specimens consolidate to intended effective stresses. The stresses correlate with the one from the triaxial test: *50 kPa, 280 kPa and 500 kPa*. However, the process of consolidation within the direct shear test is easier and faster to conduct compared to the triaxial test. The loading device consists of a lever system which applies normal stress by putting weights on a hanger, inducing a *10* times higher force to the specimen. The associated weights for each stress are listed in Table 3.6.

During consolidation, the vertical displacement is measured, allowing to plot the vertical displacement versus the square root of consolidation time. According to *ISO 17892-10*, the plot attains the determination of the maximal rate of horizontal displacement. Usually, the velocity should be small enough that no pore pressure emerges. However, since the consolidation of sand takes place within the first seconds after loading, the rate of displacement is defined as *0.5 mm/min* (Dohmel, 2014).

Table 3.6: Effective stresses and associated weights for the direct shear test

	Specimen 1	Specimen 2	Specimen 3
Effective stress $\sigma'$	50 kPa	280 kPa	500 kPa
Required Weight on hanger	1.83 kg	10.28 kg	18.35 kg

### 3.2.1.3 Shearing

At this stage, the specimen is sheared under a constant rate of displacement along the horizontal plane between the upper and lower frame. Before shearing, it is important to fix the shear box inside the apparatus and to remove the bolts, which hold the upper and lower frame together. During testing, vertical and horizontal displacement are automatically recorded. Besides, a displacement of a probe ring (shear way) infers from the applied shear stress. The test ends after reaching the maximal horizontal displacement of *13 mm* and shear way and vertical displacement remain constant. If there is no indication of the constant level, the shear box is removed to the start, followed by repeating the test to ensure reaching the critical state. All recorded data are presented in the associated Datasheet in Annexe B.

### 3.2.2 Calculations

The applied shear force is proportional to the measured shear way, whereas the ring's stiffness is the constant of proportionality.

$$T = s \cdot C \quad (3.18)$$

During shearing, the specimen's cross-section changes, but the determination of shear stress bases on the simplification of a constant section.

$$\tau = \frac{T}{A_0} \quad (3.19)$$



## 3.2 Direct Shear Test

### 3.2.3 Problems during Testing

During testing, several problems occurred, which affected the results negatively. Firstly, obtaining undisturbed samples from the container appeared complicated. Pushing the cutter inside the soil caused immediate disturbance and rearrangement of the structure. Besides extruding the sample from the tube generates a higher density on the bottom, whereas the top structure loosens. Therefore, specimens from one sample showed different densities.

Another immense influence on the results was tilting of the box's top cap during shearing. Therefore, the shear force caused a moment by what the back part of the upper frame lifted, whereas the top cap settled and tilted (Figure 3.33). The tilting had an impact on vertical displacement so that the results do not represent the proper tendency of dilatancy. Besides, lifting of the upper frame opened a wide gap, in which soil interlocked. On the one hand, soil left the box, causing an undesired settlement, but on the other hand soil between both frames generated friction, affecting an apparent higher shear strength. One primary purpose was to determine the critical state by reversing the shear box and repeating the test. Though, this process pushed as much soil between both frames that results are ineligible. Besides, it was notable that the effect of tilting and lifting appeared more significant at higher normal stress.

To conclude, due to the discussed problems, only peak strength parameter could be determined. Neither the vertical displacement nor the reversing test obtained consistent results, due to tilting of the top cap and interlocking of soil particles.

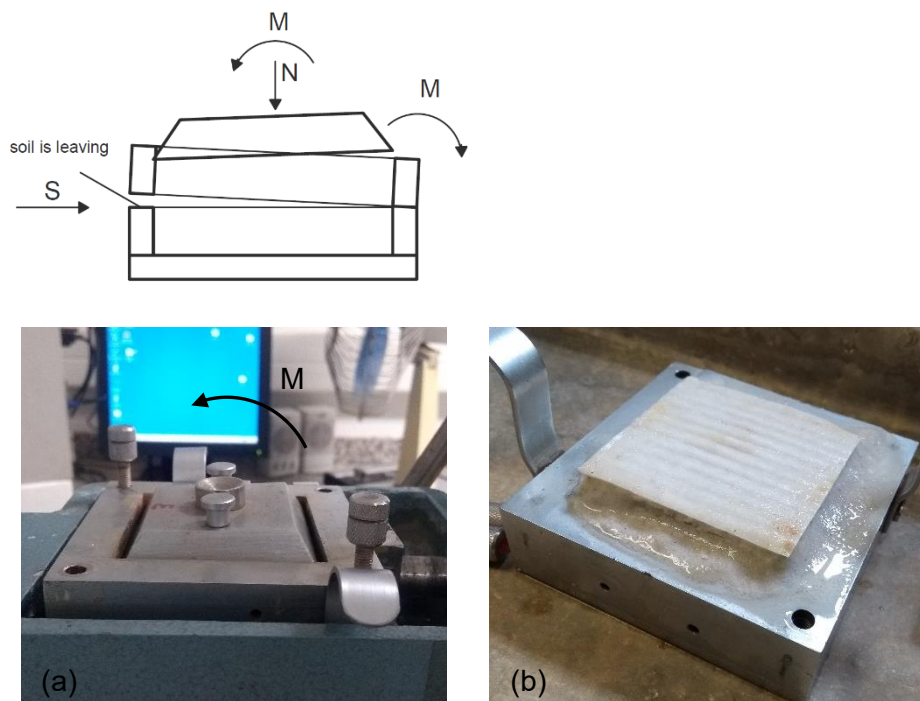


Figure 3.33: (a) Tilting of the top cap, (b) soil in between the frames



### 3.2.4 Results

In total, four samples were tested, but due to disturbance, the results of sample 5601 are unusable. Figure 3.34 represents the stress-strain plot from sample 5604, demonstrating the shearing behaviour of the specimens of different normal stresses. It can be noted that all lines reach a clear peak, followed by decreasing until remaining constant. With an increase in normal stress, the peak stress and the associated horizontal displacement increase as well. Besides, at higher normal stress the line crashes immediately after peaking, but at lower normal stress, the line decreases more slightly.

The shear stress plotted against the vertical displacement of sample 5604 can be seen from Figure 3.35. The plot must be used carefully since tilting of the top cap affected the results of vertical displacement, especially for the specimen at higher normal stress. However, conclusions can still be drawn, regarding the tendency of dilatancy during shearing. According to that, all lines of different normal stresses show a tendency of dilation. At higher normal stress ( $\geq 280 \text{ kPa}$ ) the specimen first contract, followed by dilatancy whereas at lower normal stress ( $50 \text{ kPa}$ ) the specimen performs dilatancy immediately. This behaviour correlates with the triaxial test, confirming the assumption of testing dense sand.

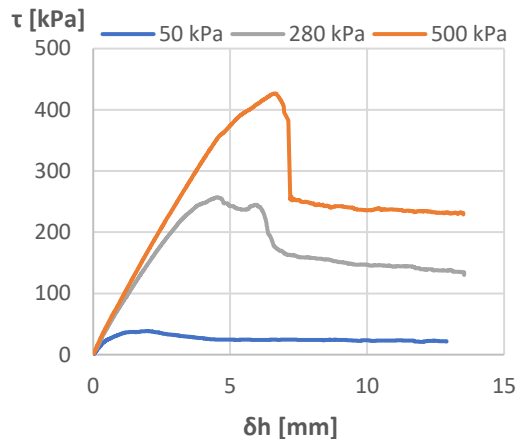


Figure 3.34: Stress-strain plot from the direct shear test of sample 5604

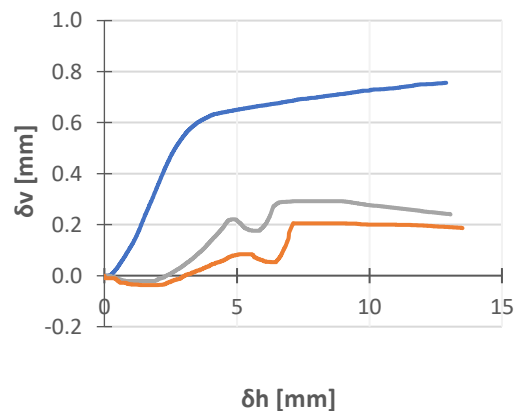


Figure 3.35: Plot of vertical displacement against horizontal displacement of sample 5604

Figure 3.36 assembles the stress-strain plots of two different samples. By comparing the lines, it can be noted that the samples show the same behaviour in reaching the peak, with nearly the same values of peak stress and horizontal displacement, but afterwards, the lines fall to significantly different values of constant level. This behaviour is unpredictable and distinguishes from every sample.

Figure 3.37 indicates the peak and critical failure envelope of sample 5604 by plotting the shear stress against the associated normal stress of the three specimens. Therefore, the peak envelope gives a reasonable approximation to the associated points, not intercepting the y-axis so that cohesion equates zero. All sample coincide in this behaviour, whereas the associated peak friction angles fall in a range of  $38^\circ - 40^\circ$ . In comparison, the peak friction angle, obtained from the triaxial test, equates  $37^\circ$ . Hence, the resulted angle from the direct shear is, on average,  $2^\circ$  higher. The failure envelopment for the critical state also approximates well to the associated points, but comparing the envelopes between the different samples, the lines and the associated critical friction angles  $\phi'_{crit}$  distinguish significantly.

### 3.2 Direct Shear Test

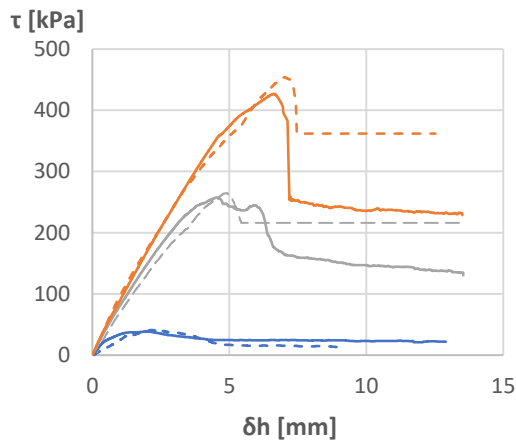


Figure 3.36: Comparison of direct shear behaviour between sample 5604 (continuous) and sample 5609 (pointed)

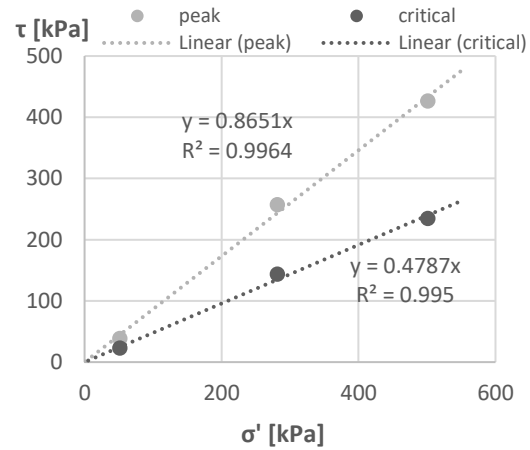


Figure 3.37: Failure envelopes from the direct shear test of sample 5604,  $\phi'_{peak} = 41^\circ$  and  $\phi'_{crit} = 26^\circ$

As already noted, it is evident that the results for the specimens of 280 kPa and 500 kPa are more inaccurate since the effect of tilting and frame opening has a higher impact. Regarding only the results of the specimens of 50 kPa, indicated in Figure 3.38 and Figure 3.39, the curvatures are more uniform and coincide with each other. Besides, the lines correlate with the behaviour of dense sand by carrying out dilation. Table 3.7 summarises the obtained results. Assuming that cohesion equates zero, the peak friction angles  $\phi'_{peak}$  fall in a range of 37° - 39. Hence, the results are similar to the obtained friction angle from the triaxial test. Nevertheless, the critical friction angles  $\phi'_{crit}$  still distinguish immensely.

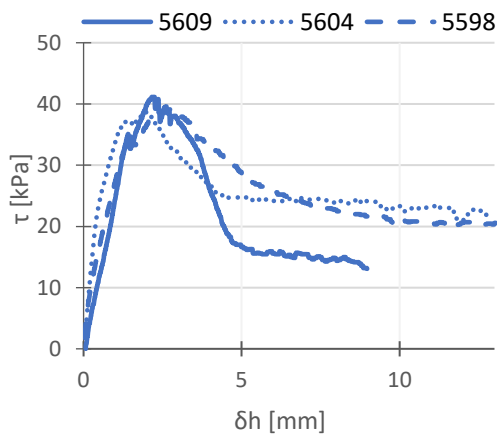


Figure 3.38: Stress-strain plots from the direct shear test of the specimens of 50 kPa

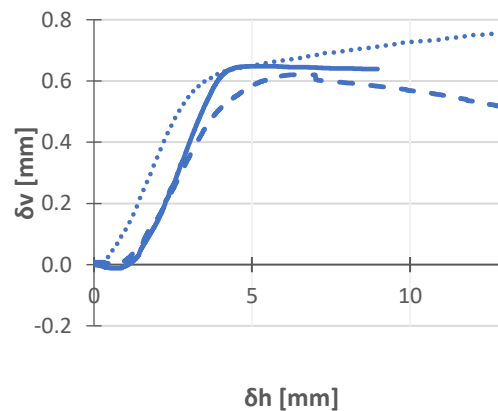


Figure 3.39: Plots of vertical displacement against horizontal displacement of the specimens of 50 kPa

Table 3.7: Results of from the direct shear test from the specimens of 50 kPa

Sample	5598	5604	5609
Peak stress	39 kPa	39 kPa	41 kPa
$\phi'_{peak}$	37.2°	37°	39°
Critical stress	21 kPa	23 kPa	15 kPa
$\phi'_{crit}$	22.78°	24.7°	16°

## 3 Determination of the Shear Strength

To conclude, due to tilting of the box's top cap and frame opening, safe results cannot be guaranteed. In particular, for the specimens at high normal stress ( $\geq 280 \text{ kPa}$ ), the shearing behaviour is unpredictable. Only at lower normal stress, the specimens show more similar lines with a correlation to dense sands. Therefore, it can be assumed that the test was carried out at too high stresses. A range of lower stress might obtain better results. However, the distribution of peak friction angles ( $37 - 40^\circ$ ) nearly correlates with the results from the triaxial test ( $37^\circ$ ), but the critical friction angles distinguish significantly, and results are unusable.

### 3.3 Discussion

#### 3.3.1 Differences between Triaxial and Direct Shear Test

For the soil from zone 1, one triaxial test and several direct shear tests were conducted aiming to determine the effective shear strength parameters of the sand in Rio Maior. The peak friction angles for both tests distinguish from  $2^\circ$ . In general, the range of variables, having an impact on the results, is extensive. Not only the size effects of specimens but also different techniques and apparatus must be regarded for evaluation and interpretation. However, those impacts of each test discuss Section 3.1.7 and Section 3.2.3. The following focuses on the difference between triaxial testing and direct shear testing concerning the stress-strain conditions and their impact on results.

One main difference between both tests is the orientation of the failure plane. In the triaxial test, the specimen is stressed in every dimension. The state of stress and change of stress is simulated realistically since the confining minor principal stress  $\sigma_3$  remains constant, while the mayor principal stress  $\sigma_1$  increases until failure. As a result, the failure plane is uncertain since failure is generated in the plane with the minimum resistance. In contrast, in the direct shear test, shearing is performed along a predefined horizontal plane, where normal stress and shear stress are directly applied. Therefore, the state of stress is only two-dimensional.

Moreover, another difference between both tests is the state of principal stress. At every stage of triaxial testing, the state of principal stress is known since the change in sectional area is calculated from deformation. The direct shear test bases on the simplification of a constant sectional area during shearing. Hence, the calculated state of stress does not correlate with the actual one.

Medzvieckas (2016) was simulating the states of stress during direct shear testing and triaxial testing for dense sand by using a finite element program. The results confirm that in the direct shear test, stresses do not distribute equally. The shear stress is applied at the specimen's edge, and therefore, higher shear stress is generated there than in the specimen's middle. Besides, the shear box walls prevent a uniform distribution of normal stress. Especially at the time of failure, locally stress concentration appears. Also, the specimen does not deform uniformly since the horizontal failure plane follows an irregular and unsmoothed geometry. However, in the triaxial test, deformation and principal stress are distributed equally. Only lateral restraint at the specimen's ends influences the state of stress.

To conclude, the triaxial test obtains more realistic shear strength parameters since they are calculated from the actual state of stress and deformation. The direct shear test provides different results, due to simplifications, which do not represent the actual state of stress and deformation. Furthermore, the failure plane is predefined and might not represent the plane with the lowest resistance (Lang, et al., 2011).

Several studies on dense sands show that triaxial tests obtain a  $3^\circ$  lower friction angle than the direct shear test (Medzvieckas, et al., 2016). Those results correlate with the

### 3.3 Discussion

results of the sand from Rio Maior. Therefore, it can be assumed the direct shear results are an additional confirmation regarding the obtained peak friction angle from the triaxial test to ensure the stability of the quarry pond slope. However, comparisons of the critical state are not provided since the results of the direct shear test are not accurate and disturbed by many unpredictable conditions

#### 3.3.2 Effect of Cementation

The site-investigation assumed that the quarry pond sand indicates a cemented structure, due to the kaolin minerals. Kaolin is a widely occurring white clay with a considerably smaller particle diameter than sand. The sieving revealed that this fine-grained fraction defines less than 10 % of the particle size distribution. In regard to cementation, the smaller kaolin minerals distribute between the sand particles and deposit on the sand's surface, bonding the particles together. Hence, the resulted matrix would improve mechanical properties. According to that, several studies about the effects of cementation on sands were carried out, allowing to compare the results with the shearing behaviour of the sand of Rio Maior, to draw conclusions if cementation occurs

Therefore, Asghari et al. (2002) investigated in the mechanical behaviour of an artificially cemented gravelly sand by performing triaxial tests. The results indicated that cemented sand sample followed a brittle failure mode without barrelling at low confining pressure, whereas at higher confining pressure, a barrelling failure mode appeared. However, all cemented specimen indicated a significant shear zone. Besides, it was noted that cemented samples showed a clear peak in the stress-strain behaviour followed by a clear fall till reaching the constant level. With an increase in cementation higher peak values were reached, but at higher confining pressure, the peaks were less clear than at lower confining pressure. Regarding the volumetric change, cemented sample underwent dilation during shearing. However, the maximal rate of dilation took place after the maximal stress ratio ( $p'/q$ ) was reached. In this connection, according to Leroueil and Vaughan (1990), the peak strength is carried out by cementation, but the maximal rate of dilatancy can only take place, after bonding breaks. Regarding the failure envelope, cemented samples rather followed a curved failure envelope with an apparent cohesion, which increased with an increasing amount of cementation.

To conclude, Asghari et al. (2002) indicated that cemented sand follows a significant behaviour at lower confining pressure, but at higher confining pressure, this behaviour disappears, and the sand appears uncemented. The effect of cementation can be explained according to Coop and Atkinson (1993) (Asghari, et al., 2002). Figure 3.40 demonstrates that every cemented structure has a yielding point at which, under a certain pressure, the interparticle bonding starts to break. At high confining pressure, this yielding point is reached before peaking. The bonding is already destroyed by the confining pressure, and the shearing behaviour correlates with the behaviour of uncemented soils, whereas failure occurs on the general failure envelope (case 1 and 2). For shearing at lower confining pressure, the yielding point is reached at the peak, and failure occurs above the envelope since intact bonding accomplishes a higher shear strength. Besides, failure appears at low axial strain since cementation prevents movement (Figure 3.40 (b)). However, after peaking the line reaches the critical state at the same strain as uncemented soils.

Hence, cemented sands show similarities to the behaviour of overconsolidated clays since exceeding the pre-consolidated effective stress causes the disappearance of cohesion, and therefore, the shear strength lies on the same failure envelope as normally consolidated clays (Figure 3.41).

### 3 Determination of the Shear Strength

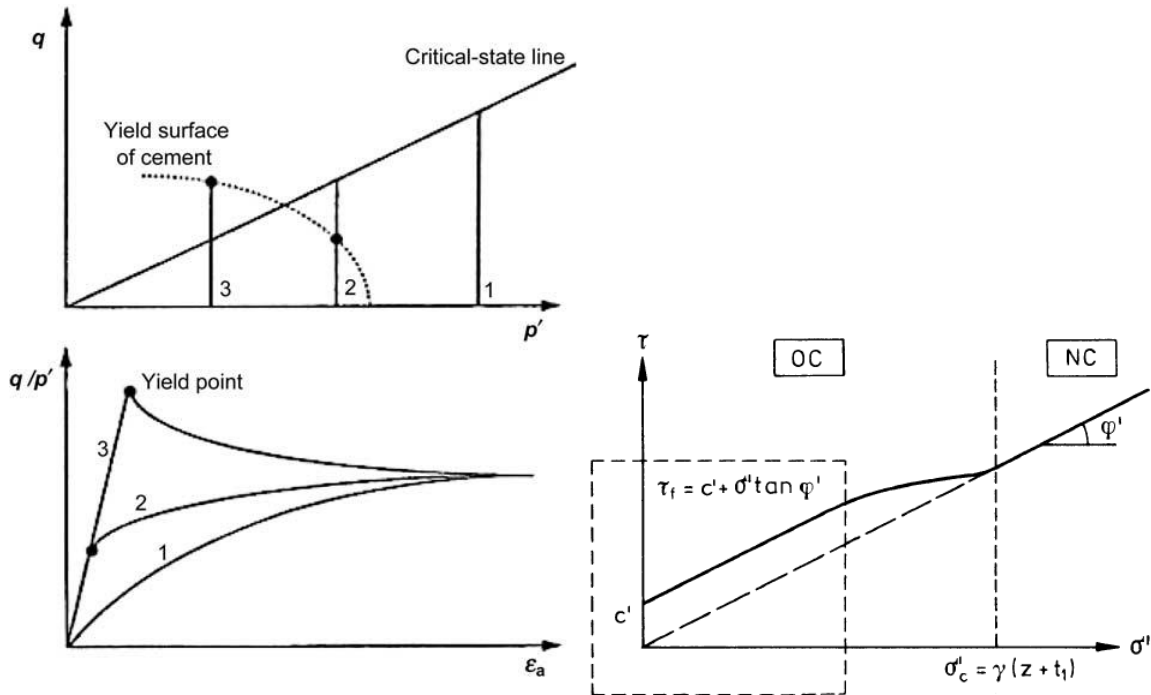


Figure 3.40: Effect of cementation (a) yielding points under different confining pressures (b) associated axial strain behaviour (Asghari, et al., 2002)

Figure 3.41: Behaviour of over consolidated soil (Lang, et al., 2011)

The triaxial test from the sand of Rio Maior shows some similarities to the explained behaviour of cemented sand, such as the occurrence of a shear zone, clear peaks in the stress-strain behaviour and the tendency of dilatancy. Nevertheless, some characteristics of the tested soil differ considerably. The specimen showed a barrelling failure by undergoing great axial strain, but cementation would prevent barrelling and the performance of axial strain. Besides, according to Asghari et al. (2002), the influence of cementation of specimen  $50 \text{ kPa}$  with the lowest confining pressure must be more significant since interparticle bonding is still intact. Though, neither the triaxial test nor the direct shear test indicate different behaviour of specimen  $50 \text{ kPa}$ , compared to the specimens with higher confining pressure. After peaking the graph falls rather slightly than crashing to the critical state, which would be expected since breaking the bonding causes a direct increase in strength. Another indication of a none-cemented structure is the miss of a definite cohesion. Like OC soils, interparticle bonding causes a strength which the sand can mobilise, without inducing normal stress. Indeed, the failure envelope from Figure 3.16 intercepts the y-axis at  $30 \text{ kPa}$ , but this assumption is uncertain and unpredictable since the regression curve can also intercept the origin.

It leads to the assumption that the sand from Rio Maior rather correlates with dense sand than with a cemented sand. Indeed, it is uncertain that there might be a real cementation in-situ since sampling by borehole could already destroy the cemented structure before testing, but even the direct shear test, where samples were collected by cylindrical cutters, indicates none cemented results. Besides, analysing the sand before testing, by direct contact with the fingers, revealed that a significant appearance of cementation does not exist.

## 3.4 Conclusion

### 3.3.3 Comparison of Zone 1 and one 2

Before testing, it was assumed that the soil from zone 1 and zone 2 coincide in properties and shear strength. However, sample 5593 from borehole S2-1 distinguishes significantly in shearing behaviour and shear strength, compared to sample 5578 from zone 1. One reason might be that the triaxial test was carried out on disturbed specimens since, before testing, it was noted that the process of retrieving by borehole already damaged the structure of the soil, and besides, soil and tube were not flush with each other. As a result, disturbance could cause a non-uniform deformation and distribution of stresses, which decreases the shear strength. However, only specimen 500 kPa indicated a very non-uniform deformation and failure occurred at low deviator stress. Hence, the associated peak point lies apart from the approximation of the failure envelope. However, the other specimens showed a similar shearing behaviour, and peak and critical points follow an excellent linear approximation of failure envelope.

Another reason for a lower shear strength might be the influence of a lower density. The low density of sample 5593 does not coincide with the *SPT* results since, according to Figure 1.4, the in-situ soil occurs very dense. However, a lower density, but the same soil, only impacts the peak strength since loose sands cannot perform dilatancy to mobilise higher friction angles. Nevertheless, the critical friction angle between dense sand and loose sand should not distinguish, but sample 5593 reveals a 5° smaller critical friction angle than the one from zone 1.

It seems reasonable to conclude that the lower shear strength of sample 5593 from zone 2 results from a different material. This assumption is already made in Section 2.5 where sample 5593 distinguishes in particle size distribution from the other samples. Indeed, the sample is also a uniform graded medium sand, but with a higher fine sand fraction, compared to the other samples. The critical friction angle is only affected by the interparticle friction. Therefore, the finer sand fraction cannot mobilise the same friction between particles as the sample from zone 1. Another influence of the fine sand fraction can be seen from the stress-strain behaviour, where sample 5593 undergoes a very higher axial strain till reaching the highest deviator stress. Hence, the fine sand provides more structure to perform strain. For this reason, the soil appeared soft, like a sponge, before testing.

Nevertheless, the second triaxial test of sample 5597 from zone 2 reveals the same shear strength as sample 5578 from zone 1. Besides, both samples follow the same particle size distribution. According to that, it is assumed that in borehole S2-2, the soil coincides with zone 1 in a depth of 10 m, whereas borehole S2-1 indicates a different soil along the whole depth.

## 3.4 Conclusion

For the determination of the shear strength regarding zone 1, one triaxial test and several direct shear tests were conducted. The triaxial test shows precise results for the peak friction angle and the critical friction angle. All specimens showed a tendency of dilatation and underwent great axial strain until failure. Compared to the triaxial test, the direct shear test obtained, on average, a 2° higher peak friction angle. Though, the results must be seen as unsafe since the tests were carried out under disturbed conditions. Besides conclusions about the critical state cannot be made since the results distinguish significantly. However, the triaxial test obtained more accurate results than the direct shear test, since stresses are simulated more realistically, and besides, deformation and states of stress distribute more uniformly. Therefore, the slope analysis bases on the shear strength parameters from the triaxial test.

### 3 Determination of the Shear Strength

Moreover, the site-investigation assumed that the sand indicated a cemented structure due to the kaolin particles. However, neither the triaxial test nor the direct shear test showed an appearance of cementation and the soil follows rather the behaviour of dense sand.

Another assumption was that the soils from zone 1 and zone 2 coincide in shear strength, but the triaxial results of sample 5593 indicate a different shearing behaviour with a 5° lower critical friction angle. The influence of this behaviour is extensive since the sample was already disturbed and showed a lower density than the *SPT* detected. Besides, the sieving revealed that the sample follows another particle size distribution. According to that, it is uncertain in what extension sample 5593 represents the in-situ soil of zone 2.

For this reason, another triaxial test of the soil from zone 2 was performed. However, finding an undisturbed sample, with the same appearance of the soil from zone 1, only accomplished with sample 5597, which was collected from a depth of 18 m. As expected, the results coincide with the results from zone 1.

In this regard, the soil layers of zone 2 are not clear since laboratory results and *SPT* are contradictory. For this reason, a soil model for zone 2 must be assessed. It assumes that until a depth of 10 m, the weaker soil occurs, whereas at 10 m the layer of the stronger soil starts. Table 3.8. summarises the resulted layers with the associated parameters of design, on which the subsequent slope analysis bases.

Table 3.8: Parameters of design based on the laboratory results.

	$\phi'_{peak}$	$\phi'_{crit}$	$c'$
Zone 1	37°	34°	0
Zone 2 (until 10m)	29°	29°	0
Zone 2 (from 10 m)	37°	34°	0

# 4 Stability Analysis

The project aims to analyse the long-term stability of two quarry pond slopes in Rio Maior. In Chapter 2 and 3, several laboratory tests were conducted to classify the soil and to determine its shear strength. The challenge of the analysis is now to construct a slope model from the provided information, which represents the in-situ conditions. It becomes clear that the laboratory tests only provide limited knowledge about the in-situ soil since the retrieved samples represent a small part of the slope. Therefore, simplifications and idealisations must be applied to characterise the slope from the known soil properties. Those idealisations, the slope analysis bases on, are described below.

First, a slope is a three-dimensional body with a continuous change in section. However, a slope analysis bases on a two-dimensional problem. Therefore, the slope is reduced by cutting it into sections, which represent the potential slope geometry. Regarding the two-dimensional problem, the slope's soil must be idealised to a model of homogenous layers, represented by soil parameters (Table 3.8). It assumes that the soil layer shows homogeneity in compactness and material. For this reason, the soil parameters must be defined accurately to ensure that every part of the layer correlates with the chosen parameter. Besides, it is important having a realistic simulation of pore water, allowing to determine pore pressure at every point of the slope.

Furthermore, one essential part of the slope analysis is the estimation of a possible failure mode. A slope fails, due to exceeding the shear strength in a failure plane. In slope analysis, the failure plane is idealised by a continuous slip surface, which follows either a straight or circular geometry. From the failure mode, the shear stress acting on the associated slip surface can be determined.

Relating to the slopes from Rio Maior, a slope model must be defined, representing the in-situ situation by including the laboratory results. However, at first, it is essential to determine a realistic failure mode since further calculations are related to that. Though, many failure modes follow complex calculation which can only be solved numerically. For this reason, the analysis is supported by the program *SLOPE/W*, defining the failure mode and finding possible slip surfaces. In the end, a reasonable assessment regarding the program is necessary to conclude if the results are simulated realistically.

In *Eurocode 7*, stability analysis of slopes is considered in the category *GEO-3*; which includes decreasing the values of the friction angle and cohesion. For the following analysis, those safety factors are regarded in some parts.

## 4.1 Numerical Implementation

### 4.1.1 Failure Mode and Method of Slices

The idealisation of the quarry pond slope from a three-dimensional into a two-dimensional model of homogenous layers allows the definition of a possible failure mode. It is assumed that the slope follows rather a circular slip surface than a straight one. Hence, stability infers from the forces acting on the circular sliding mass. However, the determination of the acting forces is time-consuming, and only possible by making simplifications. Therefore, it is reasonable to implement the analysis numerically. In this connection, the program *GEO-SLOPE International, Ltd.* provides an adequate solution by solving slope stabilities with the method of slices.

The method of slices indicates some advantages since it is clear, easy to grasp and bases on a simple numerical implementation. Within this method, the sliding mass is divided into a certain number of vertical slices. Determining the forces acting on each



## 4 Stability Analysis

slice and summing them up to by either forming a momentum equilibrium or a horizontal forces equilibrium reveals the factor of safety. The factor of safety is the rate between driving forces and resistant forces. It concludes if stability is precarious or not. However, failure can follow several possible slip surfaces, and therefore, SLOPE performs many trials to find the critical slip surface of the lowest factor of safety. The method of slices provides several functions and factor of safety methods to implement the acting forces. The following sections explain the essential assumptions on which the analysis of the slope from Rio Maior bases.

### 4.1.2 Factor of Safety (FS)

The evaluation of slope stability with *SLOPE/W* bases on the factor of safety method.

The *FS* follows limit equilibrium formulations. According to *SLOPE/W*, it is defined as:

*»A factor of safety is defined as that factor by which the shear strength of the soil must be reduced in order to bring the mass of soil. into a state of limiting equilibrium along a selected slip surface«* (GEO-SLOPE International Ltd, 2018)

It can be expressed with respect to moment equilibrium,

$$F_m = \frac{M_r}{M_d} \quad (4.1)$$

and with respect to horizontal force equilibrium.

$$F_f = \frac{H_r}{H_d} \quad (4.2)$$

In general, it expresses whether the slope will fail,  $F < 1$ , or not,  $F \geq 1$ . *SLOPE/W* provides several factor of safety methods, as shown in Table 4.1, either including just one equilibrium or both. The selection of the appropriate method mainly depends on the considering failure mode and the definition of the interslice forces, as explained in the following Section 4.1.3.

Table 4.1: Methods of slope stability analyses (Adeyeri, 2015)

Method	Factor of Safety (FS)		Interslice Force Assumption (H=Horizontal, V=Vertical)
	Force Equilibrium	Moment Equilibrium	
1. Ordinary (Swedish or USBR)	-	Yes	Ignore both H, V
2. Bishop's Simplified	-	Yes	V ignored, H considered
3. Janbu's Simplified	Yes	-	V ignored, H considered
4. Janbu's 'Generalised'	Yes	-	Both H, V considered
5. Spencer	Yes	Yes	Both H, V considered
6. Morgenstern-Price	Yes	Yes	Both H, V considered
7. Lowe-Karafiath	Yes	-	Both H, V considered
8. Corps of Engineers	Yes	-	Both H, V considered

## 4.1 Numerical Implementation

### 4.1.3 Method and Fundamental Assumptions

As already discussed, the numerical implementation within *SLOPE/W* bases on a limit equilibrium which obtains the *FS* to evaluate slope stability. Therefore, it is essential to find an adequate factor of safety method, representing the failure mode and providing consistent results. As shown before, the sliding mass is divided into vertical slices; between their faces, forces are acting. Those forces are defined as interslice forces. (GEO-SLOPE International Ltd, 2018). Figure 4.1 shows a free body of a slice with acting forces. Here, the interslice forces are resolved into a vertical component, the shear force  $X_i$ , and into a horizontal component, the normal force  $E_i$ . It becomes clear that the slice is statically indeterminate. Therefore, the calculation of the normal force  $N$  along each slice is only possible by making assumptions regarding the interslice forces.

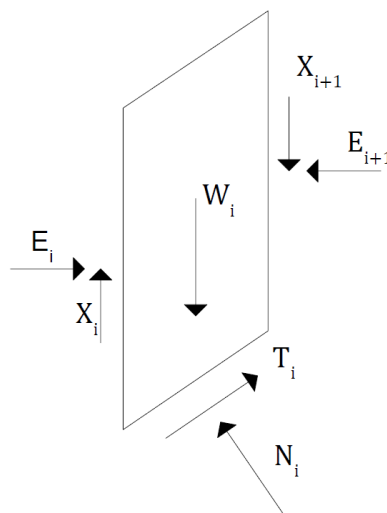


Figure 4.1: Acting interslice forces

To find an appropriate method, it can be useful having a look back to the analysing slope. It is defined that failure follows a circular slip surface. According to that, the sliding mass moves by rotating around the circle centre. Moreover, the whole mass can rotate independently from any interslice slippage (GEO-SLOPE International Ltd, 2018). As a result, the momentum equilibrium is independent of the interslice forces  $X_i$  and  $E_i$ . However, it must be considered that the interslice forces still have an impact on horizontal force equilibrium since slippages between the slices are necessary for a lateral movement of the whole sliding mass (GEO-SLOPE International Ltd, 2018). According to this, the Bishop's simplified method provides a standard solution for circular slip surfaces. As shown in Table 4.1, the method ignores the interslice shear force but includes the interslice normal force. This simplification enables to calculate the normal force  $N$ , acting on the base of each slice, by summing forces in the vertical direction. As a result, the shear force infers from the normal force, which enables to determine the *FS* with respect to moment equilibrium, due to the insensitivity of any interslice force. However, this method does not satisfy horizontal force equilibrium whereby just one *FS*

## 4 Stability Analysis

can be determined. Though, experiences show that the Bishop's simplified method obtains confidential results for circular slip surfaces.

Figure 4.2 illustrates a slice, presenting the acting forces, according to Bishop. Since the analysis considers long-term stability, effective stresses are included. According to Figure 4.2, the  $FS$  can now be calculated.

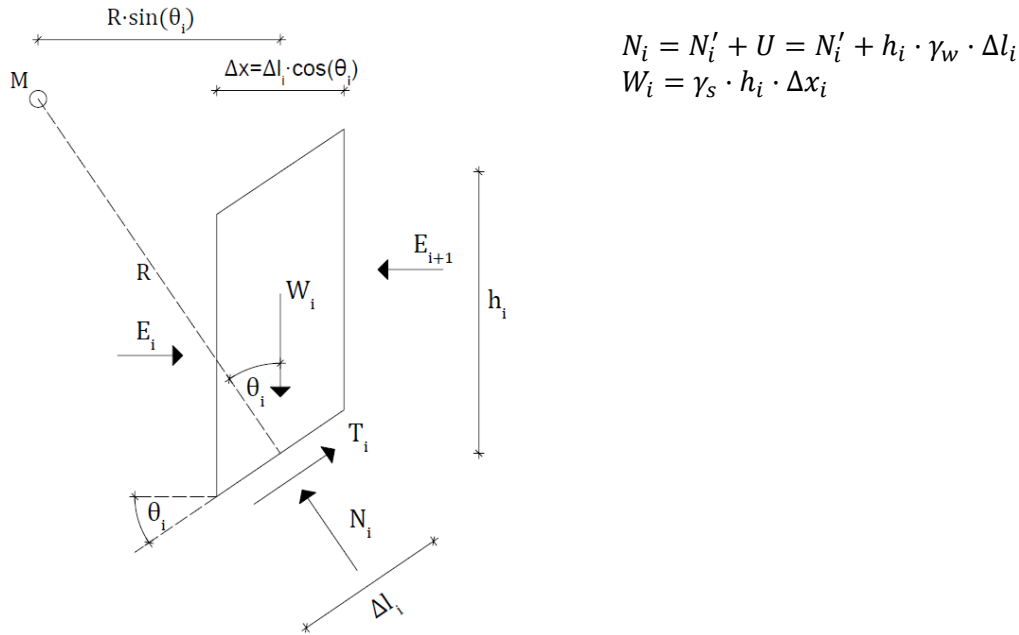


Figure 4.2: Slice according to Bishop

The shear stress at the time of failure bases on the Mohr-Coulomb failure criterion.

$$\tau = c' + \sigma' \cdot \tan \varphi' \quad (4.3)$$

However, the mobilised shear stress before failure is assumed to be  $FS$  smaller than the max. shear strength from (4.3) (GEO-SLOPE International Ltd, 2018).

$$\tau_{mob} = \frac{c'}{F} + \sigma' \cdot \frac{\tan \varphi'}{F} \quad (4.4)$$

The normal force at the base of each slice is determined by summing forces in the vertical direction, according to Figure 4.2.

$$\sum V = 0 \rightarrow 0 = S_i \cdot \sin \theta_i + N_i \cdot \cos \theta_i - W_i \quad (4.5)$$

Hence, the mobilised shear force of each slice equates:

#### 4.1 Numerical Implementation

$$T_i = \frac{c'_i \cdot \Delta l_i}{F} + N'_i \cdot \frac{\tan \varphi'}{F} \quad (4.6)$$

The substitution of the total the normal force and the shear force into formula (4.5)

$$N_i = N'_i + u_i \cdot \Delta l_i \quad (4.7)$$

gives

$$0 = \left( \frac{c'_i \cdot \Delta l_i}{F} + N'_i \cdot \frac{\tan \varphi'_i}{F} \right) \cdot \sin \theta_i + N'_i \cdot \cos \theta_i + u_i \cdot \Delta l_i \cdot \cos \theta_i - W_i \quad (4.8)$$

Expanding the first term of formula (4.8) by  $\cos \theta_i$  gives

$$0 = \frac{c'_i \cdot \Delta l_i}{F} \cdot \tan \theta_i \cdot \cos \theta_i + N'_i \cdot \left( \frac{\tan \varphi'_i}{F} \cdot \tan \theta_i + 1 \right) \cdot \cos \theta_i + u_i \cdot \Delta l_i \cdot \cos \theta_i - W_i \quad (4.9)$$

With

$$\Delta x_i = \Delta l_i \cdot \cos \theta_i \quad (4.10)$$

the effective normal force is resolved as

$$N'_i = \frac{W_i - u_i \cdot \Delta x_i - \frac{c'_i \cdot \Delta x_i}{F} \cdot \tan \theta_i}{\left( \frac{\tan \varphi'_i}{F} \cdot \tan \theta_i + 1 \right) \cdot \cos \theta_i} \quad (4.11)$$

As a result,  $FS$  can be calculated, according to Bishop's simplified method, with respect to moment equilibrium, whereas the driving moment is

$$M_d = R \cdot \sum_{i=1}^n W_i \cdot \sin \theta_i \quad (4.12)$$

and the resistant moment

$$M_r = R \cdot \sum_{i=1}^n T_i = R \cdot \sum_{i=1}^n \left( \frac{c'_i \cdot \Delta l_i}{F} + N'_i \cdot \frac{\tan \varphi'}{F} \right) \quad (4.13)$$

## 4 Stability Analysis

The state of limiting equilibrium occurs when the resistant moment equates the driving moment.

$$M_r = M_d \quad (4.14)$$

After solving (4.14),  $FS$  is defined as

$$F = \frac{M_r}{M_d} = \frac{\sum_{i=1}^n (c'_i \cdot \Delta l_i + N'_i \cdot \tan \varphi')}{\sum_{i=1}^n W_i \cdot \sin \theta_i} \quad (4.15)$$

The substitution of  $N'_i$ , according to formula (4.11), and

$$M_i(\theta_i) = \left( \frac{\tan \varphi'_i}{F} \cdot \tan \theta_i + 1 \right) \cdot \cos \theta_i \quad (4.16)$$

gives (Adeyeri, 2015)

$$F = \frac{\sum_{i=1}^n \left( c'_i \cdot \Delta l_i \cdot M_i(\theta) + \left( W_i + u_i \Delta x_i - \frac{c'_i \cdot \Delta x_i}{F} \cdot \tan \theta_i \right) \cdot \tan \varphi' \right)}{\sum_{i=1}^n W_i \cdot \sin \theta_i} \cdot \frac{1}{M_i(\theta_i)} \quad (4.17)$$

$$F = \frac{\sum_{i=1}^n (c'_i \cdot \Delta x_i + (W_i - u_i \Delta x_i) \cdot \tan \varphi'_i)}{\sum_{i=1}^n W_i \cdot \sin \theta_i} \cdot \frac{1}{M_i(\theta_i)}$$

Formula (4.17) presents the general equation of  $FS$ , according to Bishop, without regarding an additional load. It can be noted, that the  $FS$  appears on both sides of the equation. As a result, the equation is a nonlinear function. For solving the problem, an initial  $FS$  must be estimated. According to *SLOPE/W*, the initial guess for the  $FS$  equates 'the Ordinary factor of safety' (GEO-SLOPE International Ltd, 2018). As a result,  $M_i$ , from (4.16), can be determined, which obtains a new  $FS$  from (4.17). Subsequently, the new  $FS$  computes a new  $M_i$ , and that again a new  $FS$ . The process continues until the new  $FS$  equates the previous  $FS$  with a slight difference.

With the  $FS$ , it is now possible to calculate the forces acting on each slice. Besides, it allows determining the normal interslice forces  $H_i$  by summing the forces of each slice in the horizontal direction. Usually, the computation starts from the left slice and continues until the last slice on the right. As a result, a force polygon of every slice can be illustrated. Figure 4.3 reveals that the acting forces nearly form a closed polygon. It confirms that Bishop's simplified method finds confidential results, even by neglecting the interslice shear forces  $X_i$ .

## 4.1 Numerical Implementation

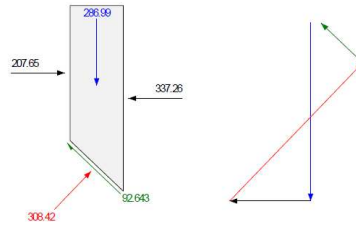


Figure 4.3: Free body and force polygon for the Bishop's Simplified method (GEO-SLOPE International Ltd, 2018)

### 4.1.4 Pore Water

Pore pressure has a significant impact on the  $FS$ , and since the quarry pond slope is located below the water table, it must be considered. Formula (4.17) bases on effective stresses since the analysis refers to long-term stability. As a result, hydrostatic pressure is integrated. The implementation is simple, assuming that a groundwater flow does not appear. According to that, the water table is defined by a piezometric line. Furthermore, *SLOPE/W* calculates the distance between the slice's base and the piezometric line and multiplies it times the unit weight of water  $\gamma_w$ . This provides the determination of pore pressure on every slice's base. However, *SLOPE/W* only includes pore pressure for calculating the shear strength at the base but neglecting it for the interslice forces.

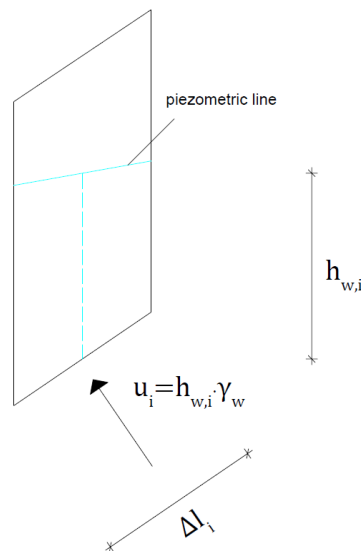


Figure 4.4: Pore pressure from a piezometric line

### 4.1.5 The Grid and Radius Method

Finding the critical slip surface of the lowest  $FS$  requires many trials. Therefore, *SLOPE/W* provides several methods, searching for the smallest  $FS$ . However, the following focuses on the grid and radius method, which forms the base for further calculations regarding the slopes form Rio Maior.

Within the grid and radius method, a grid (grid of rotation centre) above the slope is defined, composed of vertical and horizontal lines, where every intersection defines a

## 4 Stability Analysis

grid point. Moreover, those grid points could define a circle centre of the trial circle, cutting the slope. The number of grid points and the position of the grid depends on the examining problem. Below the slope surface, the radius lines are located. The number, distance and position of those lines is arbitrary. The perpendicular distance between the radius lines and the grid centres defines the trial radii. Therefore, each trial circle is tangent to the appropriate radius line, as shown in Figure 4.5. As a result, every trial circle centre has as many trial radii, as radius lines exist. For instance, Figure 4.5, shows a grid of  $6 \times 6$  points and 6 radius lines. Therefore, *SLOPE/W* computes 216 trial circles. To conclude, *SLOPE/W* sums up every possible radius for each grid point, models the trial circle and computes the appropriate *FS*.

However, to ensure the founded critical circle is the global critical circle, its centre should fall centrally inside the grid. It can be attained by defining an initial large grid to find an approximate region of the critical centre. From there, the search continues with a smaller grid to perform further trials. This process goes on until obtaining a small grid with a central position of the critical centre. Besides, the centre point shall be surrounded by contour lines, as shown in Figure 4.6. It is the optimal result for finding the lowest factor of safety.

### Grid and Radius Method

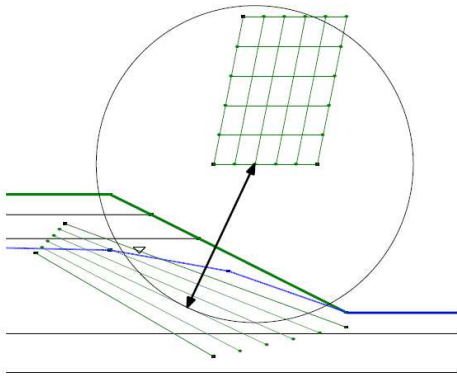


Figure 4.5: Grid and Radius Method (GEO-SLOPE International Ltd, 2018)

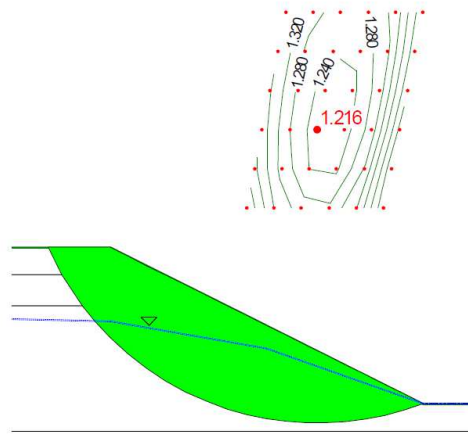


Figure 4.6: Optimal result of the Grid and Radius Method (GEO-SLOPE International Ltd, 2018)

## 4.2 Analysing of Zone 1

### 4.2.1 Slope Model

For zone 1, a municipal road is intended to build in the vicinity of the quarry pond. Therefore, *LNEC* was asked to analyse the stability of the adjacent slopes. Regarding that, the analysis bases on two situations. One is related to the current slope geometry, if stability is already precarious, whereas the other one examines the impact of the road on the stability. As already described, slopes are three-dimensional bodies with irregular shapes, having a continuous change in section. However, since the analysis bases on a two-dimensional problem, five sections are chosen to represent the slope geometry. Therefore, the geometry of the sections is grasped by a contour map of the quarry pond. However, the below focuses on the analysis of section 57. It is the section, cutting the boreholes *S1-1* and *S1-2*, indicated in Figure A.1.

Figure 4.7 illustrates section 57 with the associated slope geometry and soil layers. The analysing slope has a length of around  $240\text{ m}$  and a height of  $80\text{ m}$ . Besides, the slope surface follows a graded line with a maximum inclination of  $34,8^\circ$ . The site investigation and *SPT* reveal that the slope consists of two layers. The lower one (soil 2) represents the kaolin sand, which takes most of the slope's quantity. Due to the laboratory test, the soils properties and shear strength are well known. Besides, according to the soil classification and *SPT* results, it is assumed that the layer shows homogeneity and a high density across the whole depth. Though, instead of using the peak friction angle  $\phi'_{peak}$  for further calculations, the shear strength is defined as the critical friction angle  $\phi'_{crit}$  of  $34^\circ$ . This guarantees safe results, in case smaller compactness occurs. Besides, the unit weight of this layer equates  $21\text{ kN/m}^3$ , due to very dense sand.

The upper layer describes a sand filling (soil 1). After the exploitation of the kaolin, the remaining unusable sand is carried back to the quarry pond and filled up above the unexploited kaolin sand layer. Characteristics of this sand are not known since laboratory test are not provided, but the same proprieties as soil 2 are expected. The maximal inclination of  $34,5^\circ$  occurs in this layer. It is assumed, that this inclination defines the angle of repose. The angle is mobilised during the process of filling loose sand. In this connection, the angle of repose equates the critical friction angle, and therefore, the sand filling and the kaolin sand would coincide with their friction angles. However, since confidential information, regarding soil 1, are not provided, it is reasonable to reduce the friction angle to  $32^\circ$  to ensure safe results. Besides, the sand filling has a unit weight of  $18\text{ kN/m}^3$ , suggesting that the sand is rather loose than dense.

Figure 4.7 indicated the water table, which occurs at a level of  $56\text{ m}$ . Generally, groundwater rather follows a curved line along the ground's surface due to a flow of rainwater (Kolymbas, 2016). Though, the piezometric line is simplified as a horizontal line, which correlates with the water level of the quarry pond. The free water is modelled as a layer with a unit weight of water  $\gamma_w$  but without any shear strength.

Furthermore, Figure 4.7 reveals the change in section due to the intended road. The road is located far from the slope's crest. Comparing the dimension of the actual section to the dimension of the changed section assumes a slight impact on the stability. Besides, single loads simulate the weight of a truck acting on the surface of the road.

The presented information allows the implementation of section 57 in *SLOPE/W* to examine stability, based on the assumptions and methods of Section 4.1.



## 4 Stability Analysis

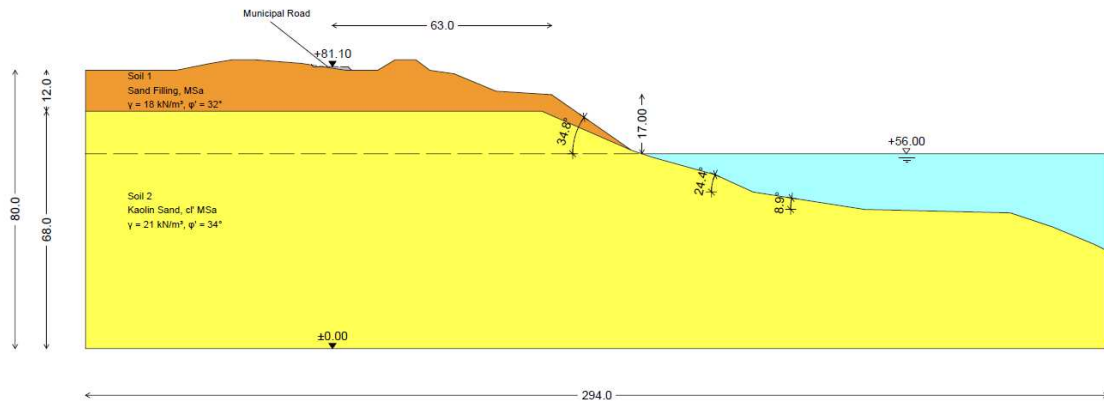


Figure 4.7: Slope model of zone 1

Table 4.2: Summarized soil parameter of design for zone 1

	Soil 1	Soil 2
Description	Sand filling, Sa	Kaolin Sand, cl' Sa
Soil Model	Mohr-Coulomb	Mohr-Coulomb
Unit weight $\gamma$	18 kN/m <sup>3</sup>	21 kN/m <sup>3</sup>
Effective friction angle $\phi'$	32°	34°

### 4.2.2 Numerical Analysis

Table 4.3: Adjustments in *GEO-SLOPE* for the analysis of zone 1

Description:	Zone 1/ Section 57
Analysis Method:	Bishop
Direction of Slip Movement:	Left to Right
Slip Surface Option:	Grid and Radius
Pore Water Pressure Option:	Piezometric Line
Number of slices	30

The below concentrates on the implementation of section 57 in *SLOPE/W*. All adjusted functions are presents in Table 4.3, whereas Table 4.2 presents the adjusted soil properties.

In the first instance, the slope analysis of zone 1 focuses on the current slope geometry, disregarding any sectional change and load due to the road, to examine if the stability is already precarious. According to Section 4.1.5, firstly, the aim is to find the global critical slip surface of the lowest *FS* by starting with a big grid and reducing the region until the critical circle centre is positioned centrally in the grid. Figure 4.9 indicates the global critical slip surface for the pond slope. The process reveals that the critical surface lies

## 4.2 Analysing of Zone 1

in soil 1, the sand filling. It is the soil with the lower shear strength, but also with the region of the highest inclination. The geometry of the sliding mass is hardly visible since it is very shallow and parallel to the surface. It is evident; the illustrated slip surface is not representing a realistic appearance since such shallow sidings do not occur in nature. The reason for this unrealistic simulation is caused by the definition of the shear strength, which is purely frictional without cohesion (GEO-SLOPE International Ltd, 2018). The shear strength is a function of the normal stress and increases across the depth, but at the soil's surface, it reveals to zero. Since the *FS* is also a function of the shear strength, it becomes clear that *SLOPE/W* always defines the shallowest slip surface as the critical one. The explained behaviour is illustrated in Figure 4.8, where the *FS* increases along the depth.

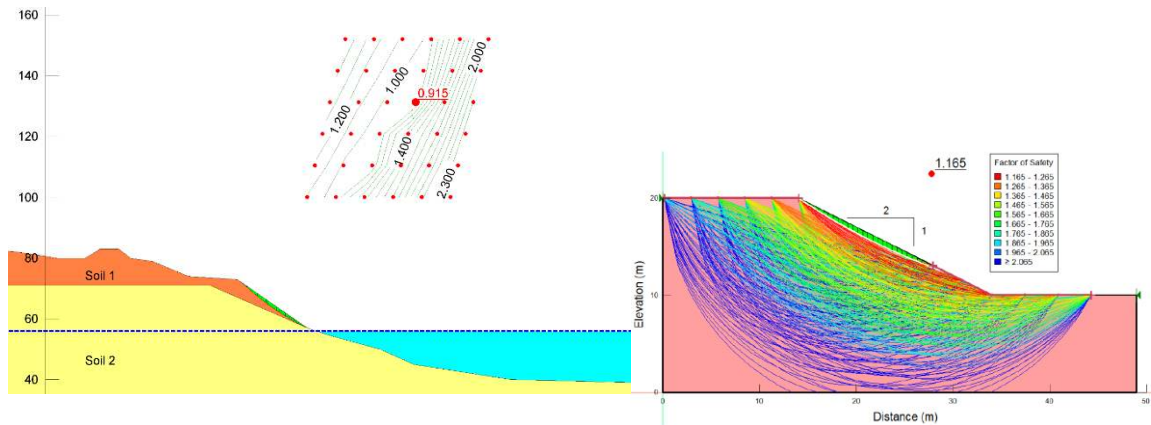


Figure 4.9: Global critical slip surface of section 57      Figure 4.8: Behaviour of the FA due to purely frictional soil

According to GEO-SLOPE International Ltd (2018), the shallow slope surface of a cohesionless soil correlates with the infinite slope case, where the *FS* is defined as:

$$F = \frac{\tan(\varphi')}{\tan(\alpha)} = \frac{\tan(32^\circ)}{\tan(34.8^\circ)} = 0.9 \quad (4.18)$$

The *FS* is below 1.0. The reason for that is the reduction of the friction angle  $\phi'_{crit}$  of the sand filling since essential information about soil properties is not known. However, in the part of the highest inclination, it can be assumed that the process of filling sand on top of the slope always generates the angle of repose. It is the maximal friction angle loose can mobilise. According to (4.18), if the angle of response and angle of the slope's inclination coincide, the FA equates 1.0. The characteristic of an infinite slope case is valid for cohesionless soil and sliding parallel to straight surfaces. Besides, pore pressure, defined as a piezometric line, has no impact on that behaviour since (4.18) is independent of effective stresses. (Lang, et al., 2011).

However, it is reasonable to analyse further slip surfaces in deeper regions, apart from shallow geometries. Therefore, *SLOPE/W* provides a function to adjust a minimal depth of slice to avoid shallow geometries. In the first case, a minimum depth of 10 m is defined. Figure 4.11 shows the associated critical slip surface. Again, *SLOPE/W* finds the shallowest slip surface as the critical one, but here the geometry appears more realistic. The circle centre is located centrally in the grid surrounded by contour lines and the *FS* increases to 1.36. Table 4.4 evaluates the critical sliding mass with a width of 1 m. The sliding mass has a respectable volume and weight, but even in consideration of

## 4 Stability Analysis

decreasing the friction angle by a safety factor, the  $FS$  is still in a safe range to ensure stability. Besides, now the kaolin sand, whose shear strength was accurately determined, mobilises most of the resistance since the sliding base lies inside its layer. From this layer, it is known that, above the critical angle, the soil can perform dilatancy.

Table 4.4: Evaluation of the sliding mass for the slip surface in a depth of 10 m

Total Volume	339 m <sup>3</sup> /m
Total weight	6282 kN/m
Total Resisting Moment	1.49 · 10 <sup>5</sup> kNm/m
Total Activating Moment	1.09 · 10 <sup>5</sup> kNm/m
FS	1.36
FS including safety factor	1.10

The second case, in Figure 4.10, indicates a deeper slip surface where most of the sliding mass lies below the piezometric line. The geometry follows a profound, circular shape, and the circle centre position is centrally in the grid, surrounded by uniform contours. The  $FS$  increases again. It confirms the behaviour of pure frictional soils, from Figure 4.8, that the  $FS$  increases along the depth, even in consideration of pore pressure. However, pore pressure still affects the shear strength, as shown in Figure 4.12. It reveals the development of the shear strength along the slip surface (left to right), with and without applying a piezometric line. Therefore, the shear strength and the associated  $FS$  decrease significantly due to pore pressure (from 2.9 to 1.6). Hence, pore water as a piezometric line affects a slower increase of the  $FS$  with increasing depth.

As a result, the cases reveal that the critical slip surface always generates in the region of highest inclination. Simulating a more realistic sliding mass, apart from shallow geometries, shows that, within the layer of the kaolin sand, stability is ensured due to high  $FS$ .

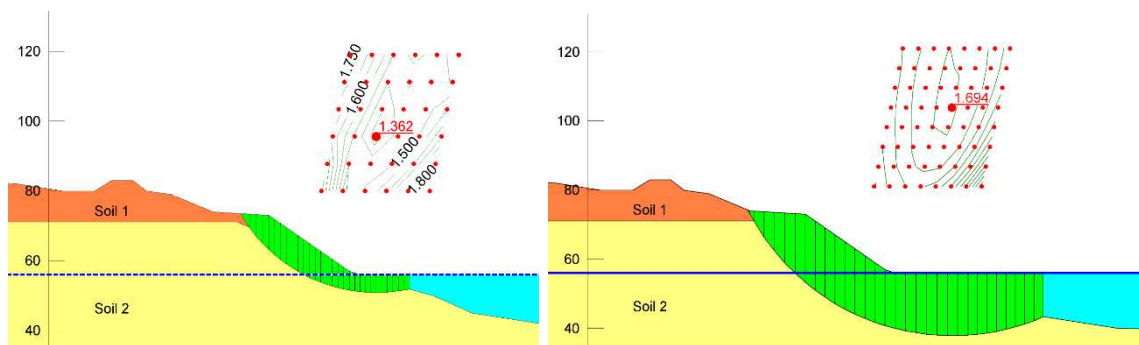


Figure 4.10: Critical slip surface in a depth of 10 m

Figure 4.11: Critical slip surface in a depth of 10 m

## 4.2 Analysing of Zone 1

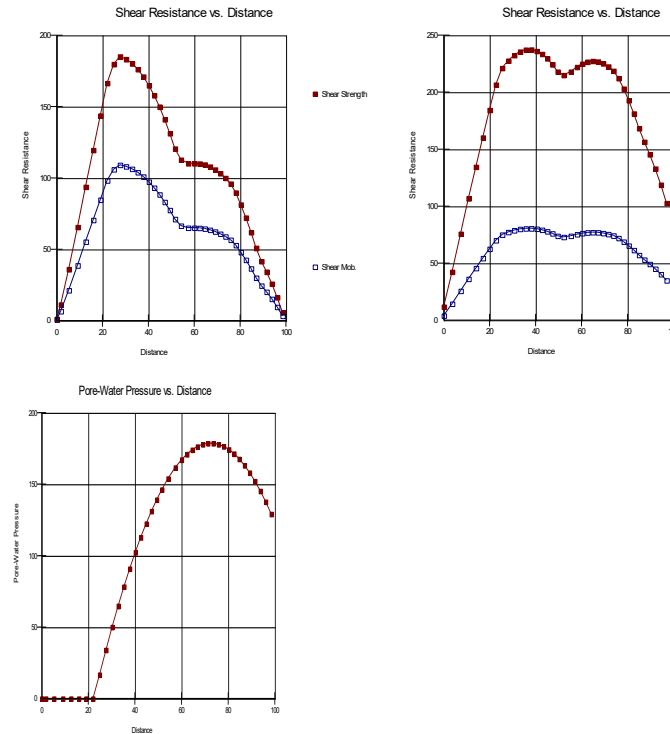


Figure 4.12: Shear strength development along the base of the slip surface, with consideration of pore pressure (right), without pore pressure (left)

Furthermore, it is requested to examine the stability in consideration of the construction of the municipal road, which causes a sectional change but also an additional load. It becomes clear that only sliding masses, which include the section of the road, are affected. For this reason, *SLOPE/W* provides a function to concentrate the radii lines to one point. This allows finding the critical circle which cuts the road's section.

Figure 4.12 indicates the critical slip surface of the current geometry and the geometry, including the sectional change. Both slip surfaces indicate a high *FS*, where the critical centre lies in the middle of the grid, uniformly surrounded by the contour lines. The high  $\underline{FS}$  is caused by a profound surface of a long radius, far away from the highest inclination. Besides, it is notable that both *FS* hardly distinguish since the sectional change is tiny. Moreover, the sectional change affects the stability positively by increasing the *FS*.

The additional load is simulated by the scenario of two trucks standing next to each other on the road. It is assumed that each truck has an axle load of  $8 \text{ t/m}$ . Therefore, two singular line loads are applied on the road's surface, one on each lane. A line load is additional weight to one slice, which affects the associated normal force and the driving moment. Testing various trials of slip surfaces reveals that the smallest *FS* follows the circle cutting through the middle of the road's section. The associated slip surface is shown Figure 4.14 The slip surface includes only one axle load. Circles, including both loads, show a higher *FS* since the geometry is more profound and away from the highest inclination. It reveals that the loads have a small impact on the critical slip surface. Only at a single load of  $20 \text{ MN/m}$ , the *FS* decreases to 1.0.

Moreover, the calculation of Figure 4.14 includes safety factors by decreasing the friction angle and increasing the additional load, according to Eurocode 7. The *FS* still indicates a high value. As a result, the construction of the road does not endanger the stability of the slope since all critical slip surfaces, which are affected by the road, show a very high *FS*.

## 4 Stability Analysis

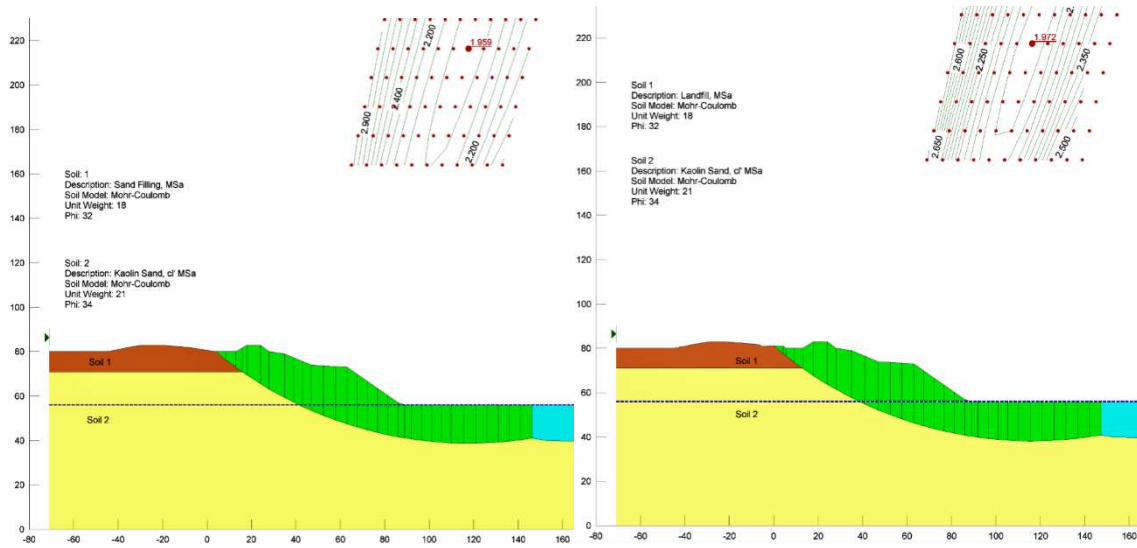


Figure 4.13: Critical slip surface cutting the road, current geometry (right), geometry with sectional change

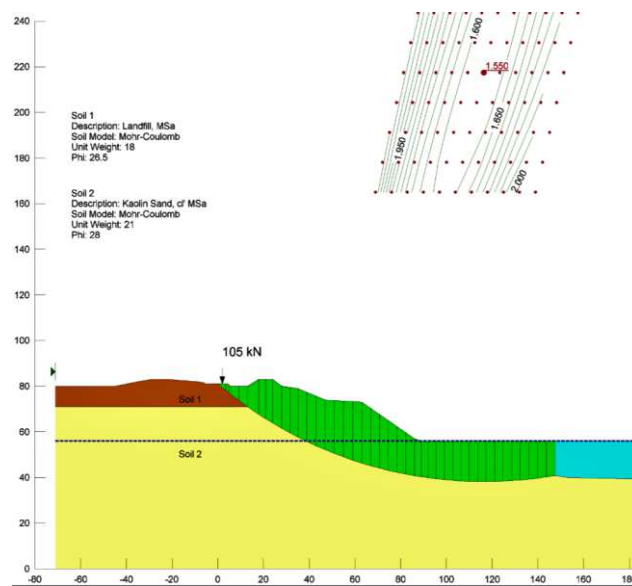


Figure 4.14: Critical slip surface with the lowest FS in consideration of the road and safety factors

## 4.3 Analysis of Zone 2

### 4.3 Analysis of Zone 2

The analysis in zone 2 regards the expansion of the exploitation area of zone 1 to an area adjacent to a steep slope. The expansion includes the construction of a platform which implicates an excavation close to the crest of the slope, as seen in Figure 4.15. In this regard, a load of an excavator could endanger stability. According to that, the stability analysis focus on the assessment in which distance to the current slope's crest the excavator can work so that stability is still ensured.

Figure 4.15 indicates the slope model. The slope shows a very high inclination of  $63^\circ$  directly next to the excavating area of the new platform. The soil layers are related to the laboratory test and *SPT* results. Soil 1 indicates a friction angle of  $29^\circ$ , which is related to the second triaxial test and reaches a depth of  $10\text{ m}$  below the surface. From there, the same soil as in zone 1 appears, which is related to the third triaxial test. The water table occurs at  $57\text{ m}$  but has no impact on this analysis.

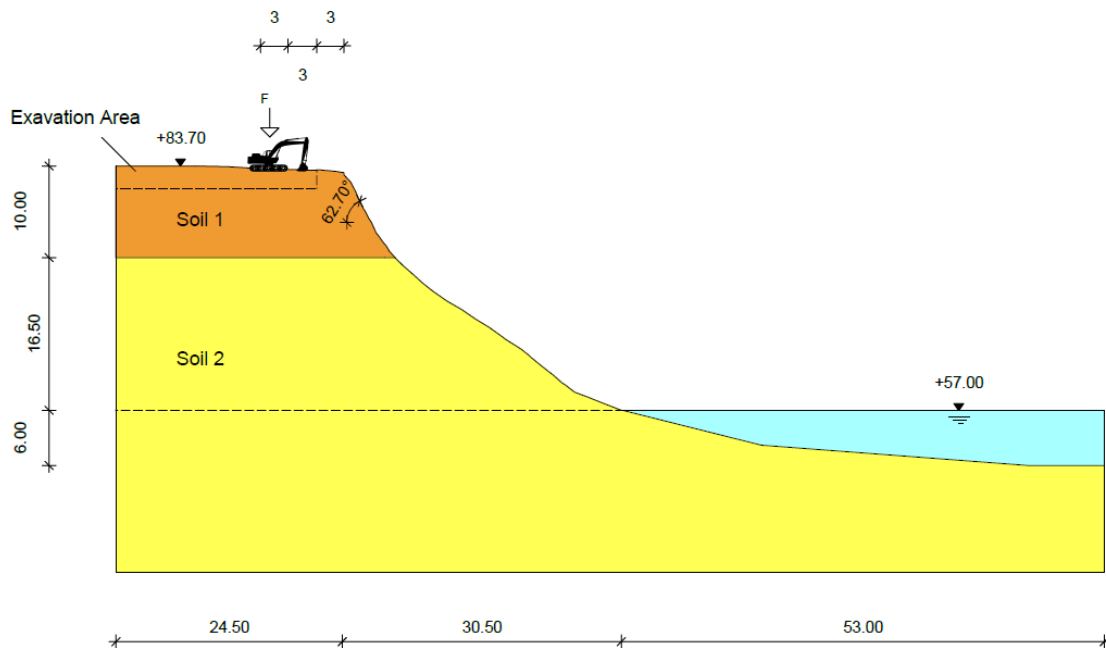


Figure 4.15: Slope Model zone 2

Table 4.5: Summarized parameter of design for zone 2

	Soil 1	Soil 2
Description	Sa	cl' Sa
Soil Model	Mohr-Coulomb	Mohr-Coulomb
Unit weight $\gamma$	$18\text{ kN/m}^3$	$21\text{ kN/m}^3$
Effective friction angle $\varphi'$	$29^\circ$	$34^\circ$

First, it becomes clear that the inclination of  $63^\circ$  is far higher than the defined friction angle of soil 1. For a purely frictional shear strength, the *FS* would follow the infinite slope case. According to formula (4.18), the slope must directly collapse since the *FS* equates  $0.3$ . For this reason, the soil must indicate an apparent cohesion, either as cementation or as suction, since high inclinations occur without collapsing. However, the laboratory tests do not reveal something about that cohesion. Therefore, the analysis assumes the lowest possible cohesion to attain a critical slip surface with a global factor of safety of

## 4 Stability Analysis

1.0. Based on the new formulation of shear strength, several trials are carried out, examining the impact of additional loads due to the excavator.

Figure 4.17 shows that *SLOPE/W* finds the global factor of safety of 1.0 with a defined cohesion of 10 kPa for both soils. As assumed, the critical slip surface is in the region of the highest inclination, cutting the head of the slope in 3 m to the crest. As a result, every work within the 3 m causes direct instability. From this point in every 3 m, trials of single line loads of 5 t, 10 t and 35 t are carried out, simulating loads of different excavator (Figure 4.17).

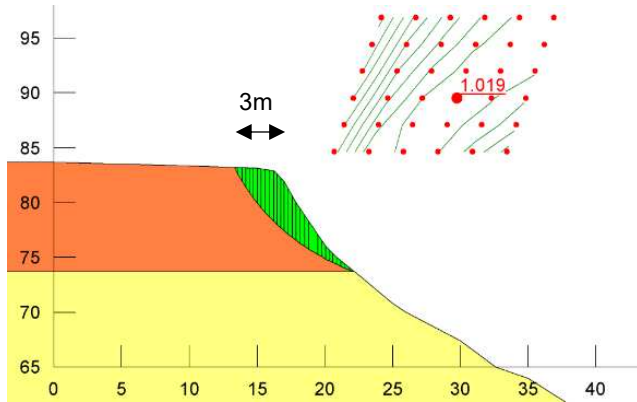


Figure 4.17: FS of 1.0 with a cohesion of 10 kPa

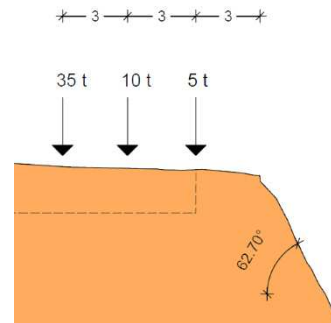


Figure 4.17: Trial distances to examine the impact of an additional load

Table 4.6 presents the resulted *FS* of the trails. It reveals a general low *FS* for every load along the whole distance. In the area of the first 6 m, none of the loads ensures stability. Between 6 – 9 m, the *FS* for a load of 5 t and 6 t show still a questionable safety, whereas the highest load of 35 t endangers stability in the whole area of the first 9 m. The associated slip surfaces are shown in Figure 4.18.

Table 4.6: Resulted *FS* of the load trials

Load	Distance to the crest		
	3 m	6 m	9 m
5 t	0.95	1.084	1.137
10 t	0.895	1.044	1.118
35 t	0.668	0.86	1.025

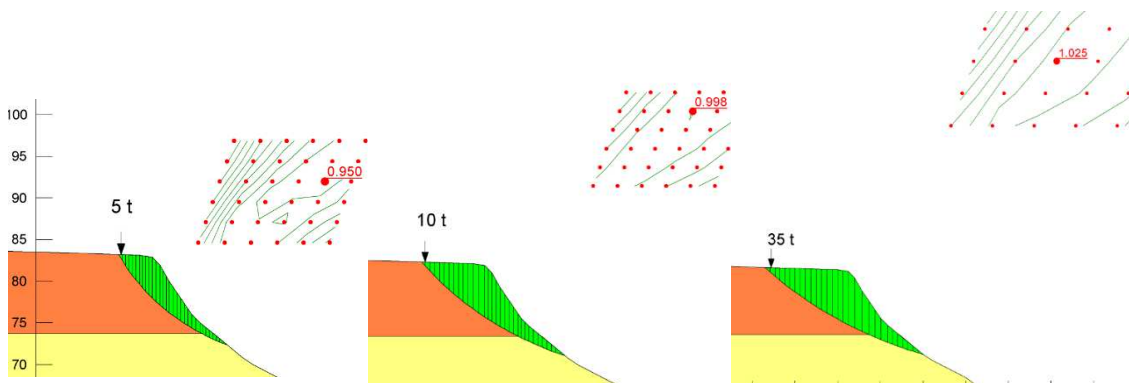


Figure 4.18: Critical slip surfaces caused by line loads of 3 m, 6 m and 9 m distance to the slope's crest



### 4.3 Analysis of Zone 2

The low  $FS$  result from the high inclination and the lowest assumable cohesion to maintain equilibrium. However, the way of applying the load might be conservative since SLOPE/W defines it as an infinite line load  $t/m$  ( $kN/m$ ). Therefore, the second trial assumes that the load is distributed over an area. This area can be attributed to a pressure line which represents the load. In this connection, a pressure line of  $20\text{ kN/m}^2$ , correlating to a load of  $10\text{ t}$ , is applied in every area of  $3\text{ m}$ . Figure 4.19 indicates the results of the applied pressure line. It reveals still a small  $FS$  between  $3\text{--}6\text{ m}$ . From  $6\text{ m}$ , the factor of safety increases to a safer range.

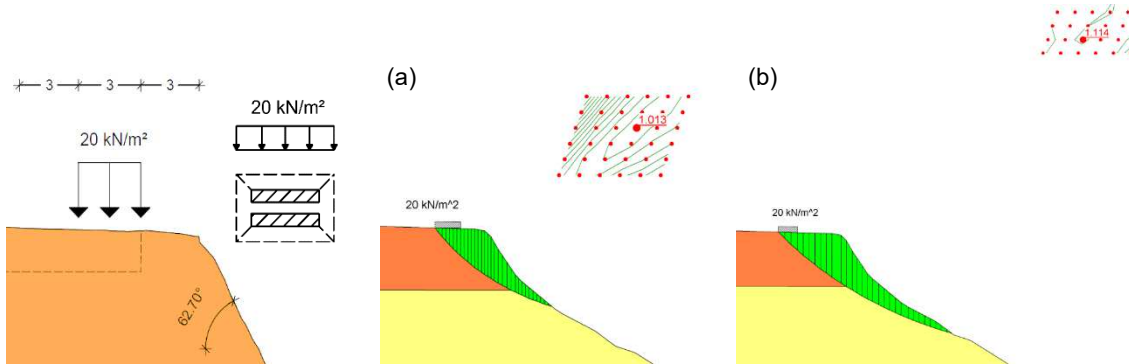


Figure 4.19: Critical slip surface caused by pressure lines, (a)  $3\text{ m} - 6\text{ m}$  distance, (b)  $6\text{ m} - 9\text{ m}$  distance

The cases show that reducing the load to a pressure line does not increase the  $FS$  immensely. In case 1, the line load is absorbed by one single slice. The impact of the line load increases the driving moment, but besides, the shear resistance in the associated slice increases as well. Since the  $FS$  is the same for every slice, a concentrated stress occurs at the slice affected by the single load (Figure 4.20). This concentrated stress does not give a realistic stress distribution since, in reality, other slices would mobilise a higher shear resistance as well. However, the  $FS$  defines an equilibrium, and therefore it does not matter how the stresses distribute. As long as all forces are integrated, the  $FS$  reveals realistic results (GEO-SLOPE International Ltd, 2018)

In the second case, the applied load distributed in one area. As a result, more slices are affected by the load, causing a more realistic simulation of stress distribution. However, the resulted  $FS$  does not differ significantly from the first case since the mobilised shear resistance affects the same equilibrium as the line load. For this reason, the geometry of the surface defines the safety. With increasing depth and distance to the crest of the slope, the  $FS$  increases as well.

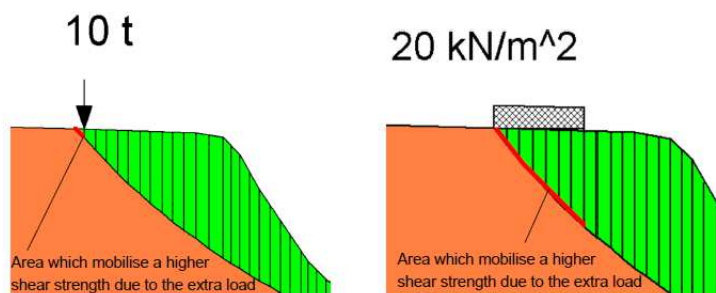


Figure 4.20: Areas mobilised by different definitions of load



## 4 Stability Analysis

To conclude, both cases reveal the limits of *SLOPE/W*. It can not simulate distributions of stress. Stresses are always defined as infinite, along a constant area. Hence, the mobilised slip surface, which defines the shear resistance, is infinite as well. This simplification causes an unrealistic stress distribution, but the *FS* depends on equilibrium formulations, and therefore, the unrealistic distribution does not impact the results. Though, since it is not clear which area of slip surface a single load mobilises, both cases can reveal conservative results.

Nevertheless, the soil conditions of the slope in zone 2 do not provide sufficient information so that the excavation work must consider the results of the load trials. Therefore, in the area of 3 -6 m only very small excavator of around 5 t should perform work. From 6 m, bigger excavator up to 10 t can be provided. Big and heavy machines should stay in a distance of at least 9 m.

### 4.4 Discussion

The method of slices, according to Bishop, bases on many assumptions and simplifications. First, the equilibrium formulation regards only static problems. Displacement and the affected distribution of stress are not considered. Besides the method assumes that failure follows a circular slip surface. According to Bishop, the *FS* can only satisfy the momentum equilibrium, but not the horizontal force equilibrium. It is an appropriate solution for more profound slip surfaces, especially when cohesion is included. However, since the sand from Rio Maior defines as purely frictional shear strength, failure follows more shallow, and elongate slip surfaced. In this regard, the method of Janbu, which considers horizontal translation, is more accurate (Lang, et al., 2011). Besides, the calculation does not include interslice shear forces, only interslice normal forces, and it can not simulate the distribution of stress by finite loads.

Considering all those simplifications, it is essential to extend the safety by including safety factors within the analysis. In zone 1, this is provided by using the critical friction angle instead of the peak friction angle. The *SPT* revealed that the soil occurs very dense from the depth of the kaolin sand. Therefore, it can be assumed that above the critical angle, the soil can perform dilatancy to mobilise a higher shear strength. Besides, regarding the construction of the road, additional safety factors, according to *Eurocode 7*, are included. In this connection, the stability for zone 1 can be guaranteed.

Nevertheless, in zone 2, the resulted *FS* indicates questionable slope stability and safety factors, according to *Eurocode 7*, are not considered in the calculation. Moreover, the ability of dilatancy for soil 1 is low, and therefore, using the critical friction angle does not provide more safety. Besides, much information about the conditions of the slope is not provided, and therefore, it is reasonable to assume the lowest possible cohesion that equilibrium is maintained. This assumption affects that the global *FS* is 1.0, and therefore, every extra load close to the slope's crest causes disability. However, the excavation work is not a permanent situation, and once the work is finished the global safety increases. According to that, it is suggested to ensure safety by performing the work from area to area, which slowly increases the *FS*. However, the project does not include this part of the analysis.

### 4.5 Conclusion

For the examination of the stability of the quarry pond slopes in Rio Maior, a numerical analysis was conducted. At first, soil models for both zones were defined. The models follow simplifications of homogenous soil layers, characterised by the known soil properties from the laboratory tests. According to that, it was defined that the slope failure follows a circular slip surface. Therefore, the implementation of the failure mode was conducted by the numerical program *SLOPE/W*, which bases on the method of slices and limit equilibrium formulations to obtain the factor of safety.

Furthermore, it was necessary to define an adequate factor of safety method concerning interslice forces. According to that, the Bishop's simplified method allowed to neglect the interslice shear forces. As a result, the formation of a moment equilibrium of the acting forces on each slice revealed the factor of safety. By carrying out a large number of trials, using the grid and radius method, the lowest *FS*, and therefore, the critical slip surface was found.

In this regard, in zone 1, the analysis revealed that *SLOPE/W* finds the slip surface of the smallest global *FS* in the region of the highest inclination with the shallowest geometry. Therefore, with an increase in depth, the *FS* increases as well. This behaviour is caused by the definition of the shear strength, which is purely frictional. As a result, the critical slip surface coincides with the infinite slope case. However, such shallow sliding does not occur in nature since the shear strength is rarely zero at the slope's surface (GEO-SLOPE International Ltd, 2018).

Simulations of more realistic, profound surfaces showed that in the layer of the kaolin sand stability is ensured by a high *FS*, whereas slip surfaces in the layer of the sand filling indicate *FS* lower than 1.0. This is caused by estimating the friction angle of the sand filling since laboratory tests for this layer were not conducted. Though, assuming that the inclination follows the angle of repose, stability can be guaranteed with *FS* of 1.0.

However, it should be considered that the soil is saturated, and therefore, suction (negative pore pressure) could affect a higher inclination. Due to the infiltration of water, suction loses its effect, causing a destabilisation. Moreover, formula (4.18) is only valid for simulating pore pressure by the simplification of a piezometric line. Often water follows a flow parallel to the slope's surface, which causes a decrease of the *FS* of around 50 % (Kolymbas, 2016). For this reason, the stability for the sand filling must be regarded carefully, and further fillings should not exceed the current inclination.

Nevertheless, the construction of the municipal road does not endanger stability since its location is far from the region of the highest inclination. The slip surfaces follow profound, circular geometries, indicating a high *FS*. Besides, singular loads to the road rarely decrease the *FS*. Only at an unrealistic high load of 20 MN/m, stability is not assured.

The second analysis, for zone 2, examined the impact of an extra load on the stability. The slope's geometry shows a very high inclination, which can only result from an apparent cohesion, such as suction or cementation. Hence, the shear strength defines the smallest assumable cohesion to obtain a global critical slip surface with *FS* of 1.0. This assumption causes unsafe stability within the area close to the slope's crest. Therefore, only small excavator should perform work in the vicinity of the slope. Besides, the working process should attain to progress in areas, for slowly increasing the stability of the slope.

## 5 Conclusion

A study on two different zones of a quarry pond for the extraction of kaolin sand in Rio Maior, Portugal, was carried out. The study included two primary purposes. The first purpose focused on a geological-geotechnical site investigation and laboratory tests aiming to characterise the occurring soil in properties and layers but also to examine the influence of expected cementation in the strength of the kaolin sand. The second purpose included the numerical stability analysis of the quarry pond slopes from both zones.

The classification concluded that the occurring soil describes slightly clayed SAND with a uniform grading. The fine-grained fraction of kaolin is less than 10 % and does not provide any plasticity for the sand. Furthermore, the tests revealed that in zone 1, the soil indicates homogeneity along the whole depth, whereas in zone 2, the soil coincides with zone 1 at a depth of 10 m, but until 10 m it differs in appearance and particle size distribution.

The triaxial test for zone 1 showed precise results, obtaining a peak friction angle of 37° and a critical friction angle 34°. All specimen showed a tendency of dilatancy and underwent great axial strain until failure, whereas cohesion did not appear. The triaxial test for zone 2, indicated a different shearing behaviour, with a 5° lower critical friction angle. The influence of this behaviour was extensive. On one side, the sample indicated a disturbance, but on the other side, it was related to another particle size distribution. Therefore, a second triaxial test for zone 2 was conducted, with a deeper sample, which coincided in results with zone 1. Hence, the laboratory investigation concluded that in zone 2, the slope consists of two layers. One layer reaches until 10 m, representing the weaker soil with a friction angle of 29°, whereas at 10 m the same soil as in zone 1 occurs.

Furthermore, none of the triaxial tests showed significant behaviour related to the expected cementation. However, the retrieval of the samples could have already destroyed the interparticle bonding so that in the fields cementation might exist.

Subsequently, a numerical analysis, based on the method of slices, according to Bishop, was carried out. The associated slope models represented the determined layers and parameters from the laboratory tests. In zone 1, a municipal road is intended to build. Therefore the analysis regarded two situations. One was related to the current slope geometry, if stability is already precarious, whereas the other one examined the impact of the road on the stability. The analysis revealed that for both cases, stability is given. The shear strength was defined as purely frictional, and therefore, the infinite slope case was decisive, defining that the highest inclination of the slope can not exceed the soil's friction angle. Furthermore, the road does not cause destabilisation since it is located far from the slope's crest. By integrating safety factor and using the critical friction angle, stability could be assured with high safety.

In zone 2, a platform is intended to be built, which implicates an excavation close to the crest of the slope. In this connection, the analysis included trails to examine, in which distance an excavator is allowed to work without endangering stability. The current slope shows a very high inclination, which can only result from an apparent cohesion, such as suction or cementation. Since information about that cohesion was not provided, the shear strength defined the smallest assumable cohesion to obtain a global factor of safety of 1.0. According to that, the analysis revealed that stability is not assured in the direct vicinity of the slope since the formulation of the cohesion just maintained equilibrium. However, the excavation work is not a permanent situation, and once the work is finished the global safety increases. According to that, it was suggested to ensure safety by performing the work from area to area to increase the FS.

# 6 Review

The first purpose of the study, the laboratory investigation, was a time consuming and intensive process, which aimed to characterise the soil to obtain a representative soil model to determine if stability is given or not. However, the geometry of the slope in zone 1 reveals that stability is rather not precarious. Therefore, a first assessment of the conditions of the slope in zone 1 could have influenced further decisions, regarding laboratory testing. The below reviews the laboratory investigation and an eventual need of improvement.

For instance, the investigation included triaxial tests, which obtained consistent results for the peak friction angle, but in the analysis, only the critical friction angle was considered. The triaxial test is a very time-consuming test, which attains a realistic simulation of stresses to illustrate stress path accurately. An assessment of the results in correlation to the *SPT* reveals that the kaolin sand can perform dilatancy since very dense conditions occur along the whole depth. In this connection, using the peak friction angle, in accordance with safety factors, would have been adequate as well. Besides, the calculated state of critical stress might not represent the actual state of stress since the deformation, at that stage, was non-uniform and barrel-shaped. Therefore, for just attaining the critical shear strength, the ring shear test gives more sufficient results.

Moreover, the triaxial test was accompanied by several direct shear test. Based on the precise results of the triaxial test, the direct shear test would not have been necessary, particularly since comparisons between both tests were hardly given due to disturbing conditions, but also since a particle size distribution, for the sample from the cylindrical cutter, was not provided. However, concerning the stability analysis, the direct shear test could have given a first and fast estimation for the shear strength, revealing that stability is not precarious. Especially for sands, the direct shear test provides confident results, and complex triaxial testing would not have been necessary.

In zone 2, it is the contrary. A first assessment of the slopes reveals that the stability is precarious, due to the steep inclination. Furthermore, the soil conditions of the upper layer, which is affected by instability, is uncertain. It is not clear in which extent the triaxial results represent the in-situ soil since it is contradictory to the *SPT* results. Hence, the analysis based on inaccurate results and assumptions. Additionally, it did not include any safety factors and therefore, even with *FS* above 1.0, stability is very questionable. In this connection, more test, regarding zone 2, should have been provided to obtain more information about actual soil properties to ensure proper safety.

## References

- Adeyeri, Joseph B. 2015.** *Technology and practice in geotechnical engineering.* Hershey, Pa : Business Science Reference, 2015.
- Asghari, E., Toll, D. G. and Haeri, S. M. 2002.** *Triaxial behaviour of a cemented gravely sand, Tehran alluvium.* Tehran : Geotechnical and Geological Engineering 21: 1–28, 2002.
- Dohmel, Welsch. 2014.** *Arbeitsblätter Geotechnik.* Dresden : s.n., 2014.
- Dr. Rees, Sean. 2013.** *What is Triaxial Testing? PART ONE: INTRODUCTION TO TRIAXIAL TESTING.* s.l. : GDS Instruments, 2013.
- Fratta, Dante, Aguetant, Jennifer and Roussel-Smith, Lynne. 2007 .** *Introduction to soil mechanics laboratory testing .* Boca Raton ; London ; New York : CRC Press, 2007 .
- GDS Instruments. 2019.** <https://www.gdsinstruments.com>. [Online] GDS Instruments, 2019. <https://www.gdsinstruments.com/gds-products/triaxial-testing-system-automated-stress-path-type>.
- GEO-SLOPE International Ltd. 2018.** *Stability Modelling with GeoStudio.* Calgary, AB, Canada : s.n., 2018.
- ISO 14688-1. 2017.** Geotechnical investigation and testing - Identification and classification of soil - Part 1: Identification and description. 2017.
- ISO 14688-2. 2017.** Geotechnical investigation and testing - Identification and classification of soil - Part 2: Principles for a classification. 2017.
- ISO 17892-10. 2018.** Geotechnical investigation and testing - Laboratory testing of soil - Part 10: Direct shear tests. 2018.
- ISO 17892-1. 2014.** Geotechnical investigation and testing - Laboratory testing of soil - Part 1: Determination of water content. 2014.
- ISO 17892-12. 2018.** Geotechnical investigation and testing - Laboratory testing of soil - Part 12: Determination of liquid and plastic limits. 2018.
- ISO 17892-4. 2016.** Geotechnical investigation and testing - Laboratory testing of soil - Part 4: Determination of particle size distribution. 2016.
- ISO 17892-9. 2018.** Geotechnical investigation and testing - Laboratory testing of soil - Part 9: Consolidated triaxial compression tests on water saturated soils. 2018.
- Kolymbas, Dimitrios. 2016.** *Geotechnik : Bodenmechanik, Grundbau und Tunnelbau .* Berlin : Springer Vieweg, 2016.
- Kuntsche, Konrad. 2016.** *Geotechnik : Erkunden - Untersuchen - Berechnen - Ausführen - Messen.* Wlesbaden : Springer Vieweg, 2016.
- Lade, Poul V. and Trads , Niels . 2014.** *The role of cementation in the behaviour of cemented soil.* s.l. : Geotechnical Research, 2014.
- Lang, Hans-Jürgen, et al. 2011.** *Bodenmechanik und Grundbau : Das Verhalten von Böden und Fels und die wichtigsten grundbaulichen Konzepte .* Berlin, Heidelberg : Springer Berlin Heidelberg, 2011.
- Medzvieckas, Jurgis, Dirgėlienė, Neringa and Skuodis, Šarūnas. 2016.** *Stress-Strain States Differences in Specimens during Triaxial.* Vilnius, Lithuania : Procedia Engineering 172 ( 2017 ) 739 – 745, 2016.
- Rackwitz, Frank. 2005.** Einfluss der Endflächenreibung bei triaxialen Kompressionsversuchen mit Berliner Sand. *Entwicklungen in der Bodenmechanik, Bodendynamik und Geotechnik: Festschrift zum 60. Geburtstag von Herrn Univ.-Professor Dr.-Ing. habil. Stavros A. Savidis.* s.l. : Springer-Verlag, 2005.
- Wood, David Muir. 1990.** *Soil behaviour and critical state soil mechanics.* Cambridge : Cambridge Univ. Pr., 1990.

# ANNEXE

## A Tables and Figures

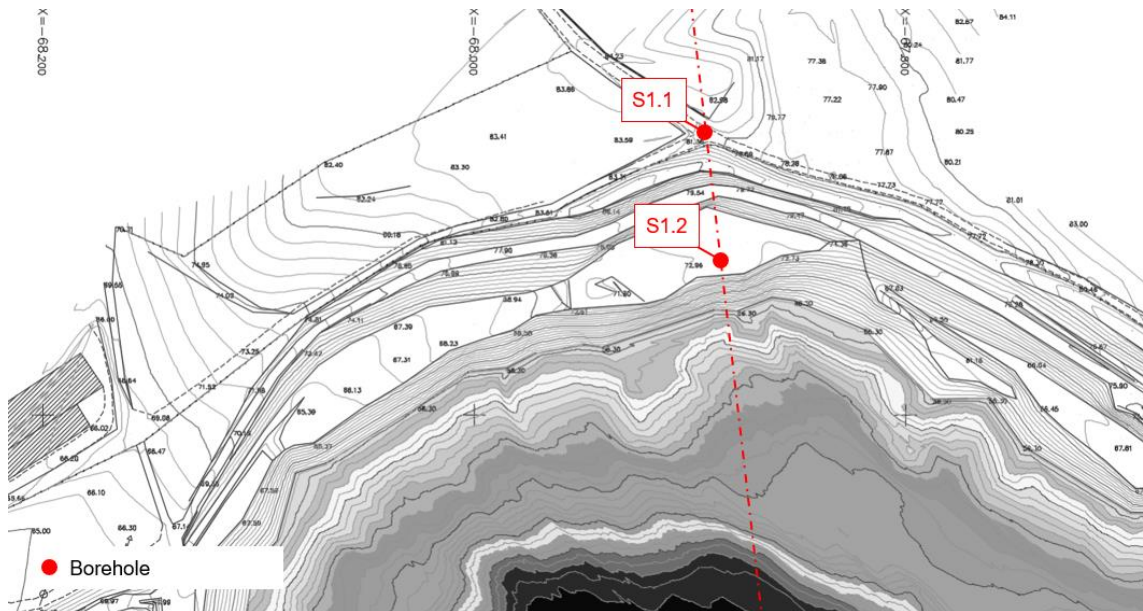


Figure A.1: Location of boreholes in zone 1

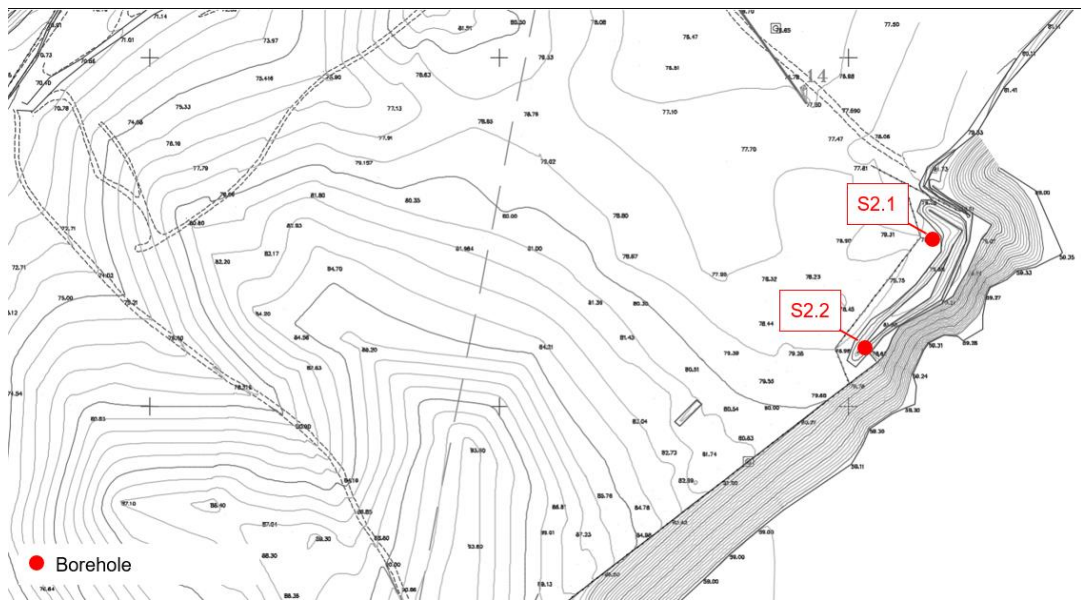


Figure A.2: Location of boreholes on zone 2

Table A.1: Performed laboratory tests

Date	Sample	Borehole	Depth [m]	WC	PD	LL+PL	PSD	TA	DS
20/03/2019	5579	S1-1	3,00-3,50	X					
20/03/2019	5578	S1-1	13,50-14,10	X	X	(X)	X	X	
20/03/2019	5579	S1-1	14,10-14,25	X		(X)	X		
11/04/2019	5587	S1-1	16,60-17,50	X					
11/04/2019	5588	S1-1	21,00-21,55	X		(X)	X		
12/04/2019	5589	S1-2	2,00-3,00	X					
12/04/2019	5590	S1-2	6,50-7,00	X		(X)	X		
12/04/2019	5591	S1-2	10,00-11,10	X					
12/04/2019	5592	S1-2	14,70-15,00	X		(X)	X		
24/04/2019	5593	S2-1	12,00-12,80	X	X	(X)	X	X	
24/04/2019	5594	S2-1	18,00-18,70	X	X		X		
24/04/2019	5595	S2-2	3,00-3,70	X		(X)			
24/04/2019	5596	S2-2	10,00-11,30	X			X		
24/04/2019	5597	S2-2	18,00-19,00	X		(X)		X	
14/05/2019	5598	Zone 1	superficial	X					X
14/05/2019	5599	Zone 1	superficial	X					X
14/05/2019	5601	Zone 1	superficial	X			X		X
14/05/2019	5602	Zone 1	superficial	X					X
14/05/2019	5604	Zone 1	superficial	X					X
14/05/2019	5609	Zone 1	superficial	X					X
<i>x = performed test</i> <i>(x) = intended test, but not performed</i> <i>WC = water content</i> <i>PD = Particle Density</i> <i>LL = Liquid Limit</i> <i>PL = Plastic Limit</i> <i>PSD = Particle Size Distribution</i> <i>TA = Triaxial Test</i> <i>DS = Direct Shear Test</i>									



Table A.2: Determined water content of all sample

Sample	Borehole	Depth [m]	W [%]
5577	S1-1	3,00-3,50	18,3
5578	S1-1	13,50-14,10	15,5
5579	S1-1	14,10-14,25	18,0
5587	S1-1	16,60-17,50	24,6
5588	S1-1	21,00-21,55	24,8
5589	S1-2	2,00-3,00	18,7
5590	S1-2	6,50-7,00	20,3
5591	S1-2	10,00-11,10	22,3
5592	S1-2	14,70-15,00	22,0
5593	S2-1	12,00-12,80	19,4
5594	S2-1	18,00-18,70	13,4
5595	S2-2	3,00-3,70	14,9
5596	S2-2	10,00-11,30	21,5
5597	S2-2	18,00-19,00	20,7
5598	Zone 1	superficial	5,1
5599	Zone 1	superficial	6,5
5601	Zone 1	superficial	6,4
5602	Zone 1	superficial	4,9
5604	Zone 1	superficial	5,6
5609	Zone 1	superficial	5,5

Table A.3: Result from the particle size distribution

Sample	5578	5579	5588	5590	5592	5593	5596	5597
Borehole	S1-1	S1-1	S1-1	S1-2	S1-2	S2-1	S2-2	S2-1
Depth [m]	13,50 - 14,10	14,10 - 14,25	21,00 - 21,55	6,50 - 7,00	14,70 - 15,00	12,00 - 12,80	10,00 - 11,30	18,00 - 19,00
Primary fraction: Sand (Sa) [%]	91.5	97	96	85	95.5	96	93	9
Coarse sand (cSa) [%]	15	12	30	28	27	5	13	1
Medium sand (mSa) [%]	55	75	62	52	60	61	75	72
Fine sand (fSa) [%]	11.5	10	4	5	2.5	30	5	7
Secondary fraction: Clay (cl) [%]	8.5	3	4	15	4.5	4	7	6
d <sub>60</sub> [mm]	0.34	0.4	0.5	0.5	0.5	0.29	0.38	0.39
d <sub>30</sub> [mm]	0.25	0.27	0.32	0.29	0.31	0.19	0.28	0.29
d <sub>10</sub> [mm]	0.1	0.17	0.21	< 0.06	0.15	0.12	0.14	0.15
C <sub>u</sub>	3.40	2.35	2.38	7.94	3.33	2.42	2.71	2.60
C <sub>c</sub>	1.84	1.07	0.98	2.67	1.28	1.04	1.47	1.44
Soil description	cl' Sa	cl' Sa	cl' Sa	cl' Sa	cl' Sa	cl' Sa	cl' Sa	cl' Sa
grading	uniformly	uniformly	uniformly	medium	poorly	uniformly	uniformly	uniformly

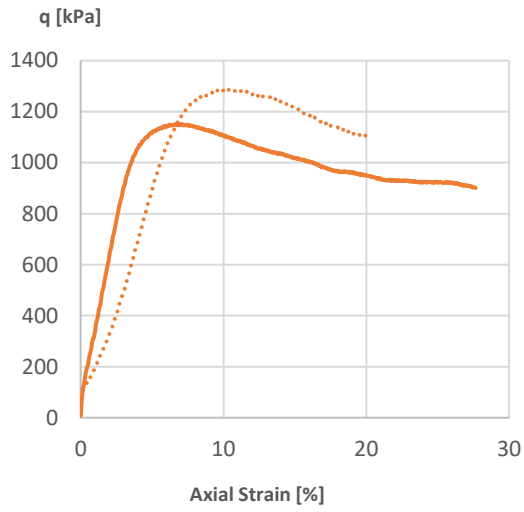


Figure A.3: Stress-strain behaviour of sample 5597

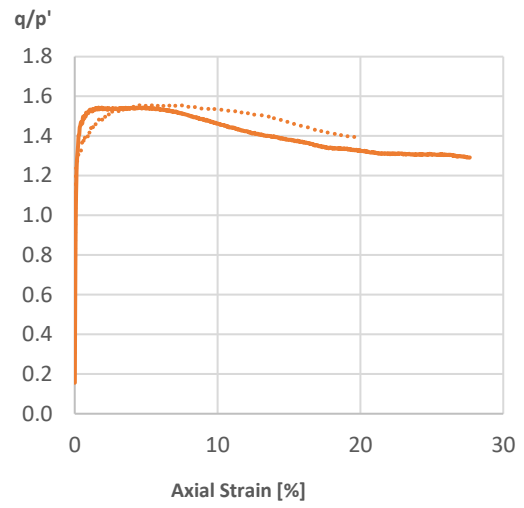


Figure A.4: Stress ratio - strain behaviour of sample 5597

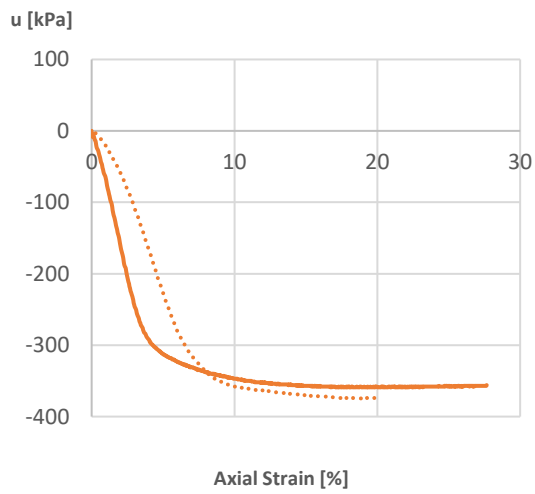


Figure A.5: Pore pressure – strain behaviour of sample 5597

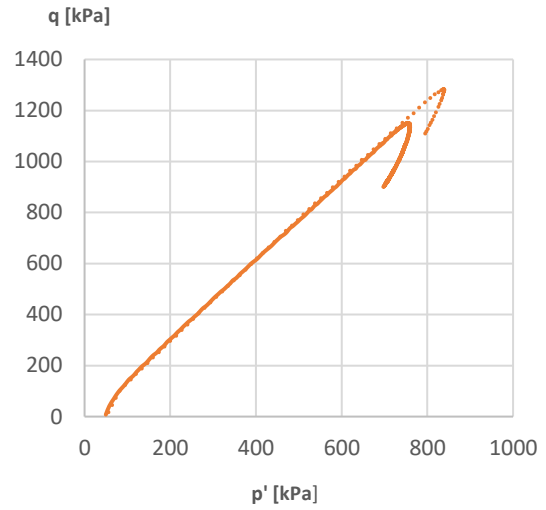


Figure A.6: Stress path of sample 5597

## **B Data Sheets**

## Particle Density Data Sheet - Pycnometer Method

Date: 06/06/2019  
 Sample number: 5578  
 Soil description: cl' Sa  
 Borehole: S1-1 (13.50 – 14.10 m)

Description			Specimens		
<b>Pycnometer No.</b>			4	14	72
Pycnometer + distilled water	m <sub>3</sub>	[g]	148.56	134.51	149.95
Pycnometer + specimen + distilled water	m <sub>5</sub>	[g]	164.38	151.03	165.80
<b>Container No.</b>			21	30	42
Container			97.43	173.48	171.76
Dried specimen + container		[g]	122.76	199.75	197.04
Dried specimen	m <sub>4</sub>		25.33	26.27	25.28
Water temperature	t	[°]	25	25	25
Temperature correction factor	k		0.999	0.999	0.999
Particle density	ρ <sub>s</sub>	g/cm <sup>3</sup>	2.66	2.69	2.68
Average particle density	ρ <sub>s</sub>	g/cm <sup>3</sup>	2.68		

Date: 11/06/2019  
 Sample number: 5606  
 Soil description: cl' Sa  
 Borehole: Cylindric cutter

Description			Specimens		
<b>Pycnometer No.</b>			31	62	92
Pycnometer + distilled water	m <sub>3</sub>	[g]	138.22	135.79	141.63
Pycnometer + specimen + distilled water	m <sub>5</sub>	[g]	154.95	150.47	157.68
<b>Container No.</b>			4	7	13
Container			168.32	191.01	212.64
Dried specimen + container		[g]	193.58	216.50	238.04
Dried specimen	m <sub>4</sub>		25.26	25.49	25.40
Water temperature	t	[°]	23	23	25
Temperature correction factor	k		0.999	0.999	0.999
Particle density	ρ <sub>s</sub>	g/cm <sup>3</sup>	2.96	2.36	2.71
Average particle density	ρ <sub>s</sub>	g/cm <sup>3</sup>	2.68		

Date: 17/06/2019  
 Sample number: 5604  
 Soil description: cl' Sa  
 Borehole: Cylindric cutter

Description			Specimens		
<b>Pycnometer No.</b>			4	14	59
Pycnometer + distilled water	m <sub>3</sub>	[g]	148.90	135.45	135.19
Pycnometer + specimen + distilled water	m <sub>5</sub>	[g]	164.48	151.01	151.12
<b>Container No.</b>			9	30	42
Container			135.07	173.48	171.75
Dried specimen + container		[g]	160.46	198.86	197.17
Dried specimen	m <sub>4</sub>		25.39	25.38	25.42
Water temperature	t	[°]	21	21	21
Temperature correction factor	k		1.000	1.000	1.000
Particle density	ρ <sub>s</sub>	g/cm <sup>3</sup>	2.59	2.58	2.68
Average particle density	ρ <sub>s</sub>	g/cm <sup>3</sup>	2.62		

**Particle Density Data Sheet**

**Date:** 04/07/2019  
**Sample number:** 5593  
**Soil description:** cl' Sa  
**Borehole:** S2-1 (12.00 -12.80 m)

Description			Specimens		
<b>Pycnometer No.</b>			4	14	59
<b>Pycnometer + distilled water</b>	m <sub>3</sub>	[g]	148.82	134.47	134.72
<b>Pycnometer + specimen + distilled water</b>	m <sub>5</sub>	[g]	164.80	150.05	150.68
<b>Container No.</b>			3	11	20
<b>Container</b>			152.27	212.51	236.73
<b>Dried specimen + container</b>		[g]	177.70	237.28	262.09
<b>Dried specimen</b>	m <sub>4</sub>		25.43	24.77	25.36
<b>Water temperature</b>	t	[°]	25	25	25
<b>Temperature correction factor</b>	k		0.999	0.999	0.999
<b>Particle density</b>	ρ <sub>s</sub>	g/cm <sup>3</sup>	2.69	2.69	2.70
<b>Average particle density</b>	ρ <sub>s</sub>	g/cm <sup>3</sup>	2.69		

**Calculations**

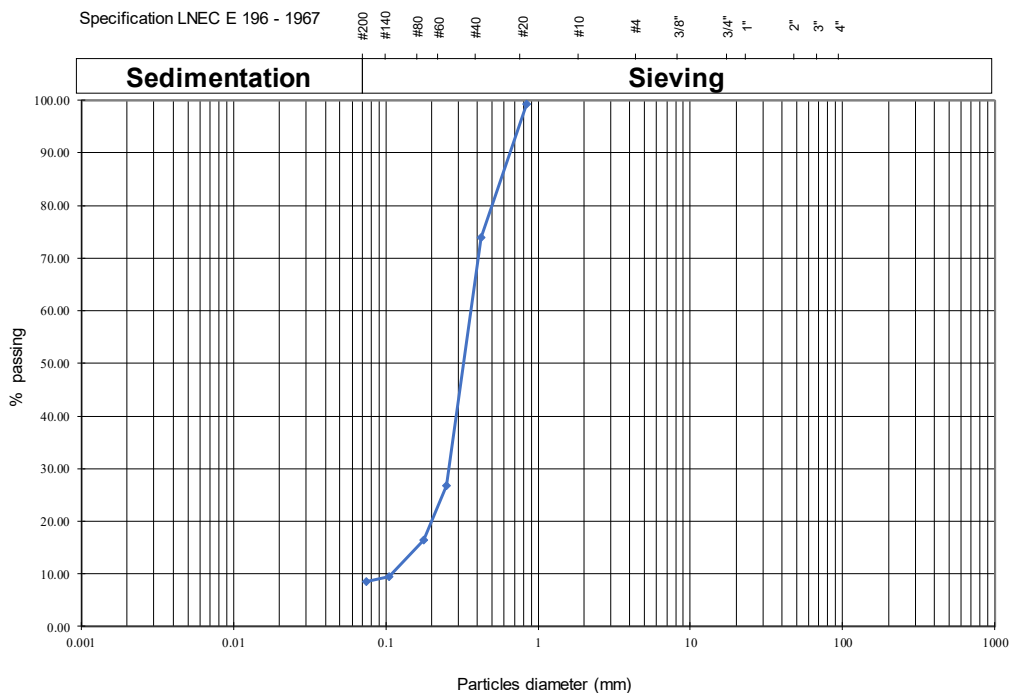
$$\rho_s = k \cdot \frac{m_4}{m_3 - (m_5 - m_4)}$$

Temp. (°)	ρ <sub>w</sub>	k
10	0.99973	1.002
11	0.99963	1.001
12	0.99953	1.001
13	0.99941	1.001
14	0.99927	1.001
15	0.99913	1.001
16	0.99897	1.001
17	0.99880	1.001
18	0.99862	1.000
19	0.99843	1.000
20	0.99823	1.000
21	0.99802	1.000
22	0.99780	1.000
23	0.99757	0.999
24	0.99733	0.999
25	0.99708	0.999
26	0.99681	0.999
27	0.99654	0.998
28	0.99626	0.998
29	0.99598	0.998
30	0.99568	0.997

## Particle Size Distribution Data Sheet

**Date:** 11/07/2019 **Mass before washing:** 728.23 g  
**Sample number:** 5578 **Mass after washing:** 671.45 g  
**Soil description:** cl' Sa  
**Borehole:** S1-1 (13,50 - 14,10 m)  
**Type of test:** Sieving

Sieve Number	Diameter [mm]	Soil retained [g]	Soil retained [%]	Soil Passing [%]
20	0.84	5.52	0.76	99.24
40	0.42	184.06	25.28	73.96
60	0.25	343.79	47.22	26.74
80	0.177	74.78	10.27	16.46
140	0.105	51.45	7.07	9.40
200	0.074	5.92	0.81	8.58
pan		5.71	0.78	7.80
washing		56.78	7.80	0.00
<b>SUM</b>		<b>728.01</b>	<b>100.00</b>	



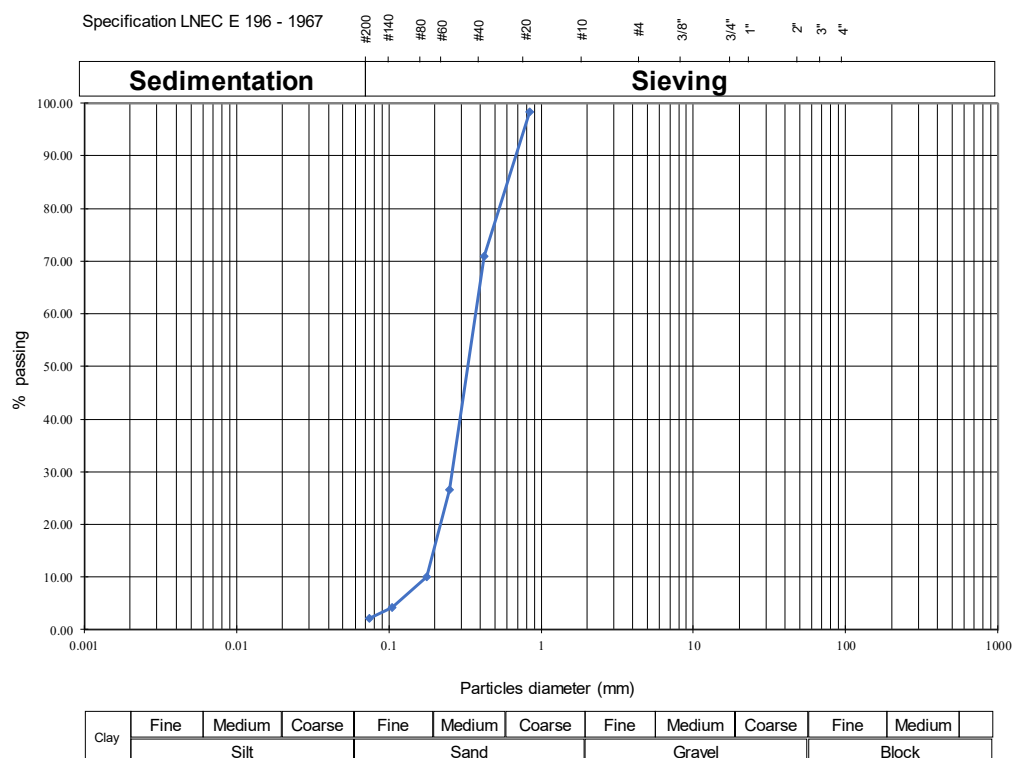
Clay	Fine	Medium	Coarse	Fine	Medium	Coarse	Fine	Medium	Coarse	Fine	Medium
	Silt			Sand			Gravel			Block	

**d<sub>60</sub>** = 0.34 mm **Primary fraction:** Sand (Sa) 91.5 %  
**d<sub>30</sub>** = 0.25 mm **Coarse sand (cSa)** (>0,63 to ≤2,0) 15 %  
**d<sub>10</sub>** = 0.1 mm **Medium sand (mSa)** (>0,20 to ≤0,63) 65 %  
**U** = 3.40 **Fine sand (fSa)** (>0,063 to ≤0,20) 11.5 %  
**C<sub>c</sub>** = 1.86 **Secondary fraction:** Clay (cl) 8.5 %

## Particle Size Distribution Data Sheet

**Date:** 27/05/2019  
**Sample number:** 5579  
**Soil description:** cl' Sa  
**Borehole:** S1-1 (14,10 - 14,25 m)  
**Type of test:** Sieving

Sieve Number	Diameter [mm]	Soil retained [g]	Soil retained [%]	Soil Passing [%]
20	0.84	3.54	1.60	98.40
40	0.42	60.45	27.40	71.00
60	0.25	98	44.41	26.59
80	0.177	36.53	16.56	10.03
140	0.105	12.84	5.82	4.21
200	0.074	4.42	2.00	2.21
Pan	< 0.074	4.87	2.21	0.00
<b>SUM:</b>		<b>220.65</b>	<b>100.00</b>	

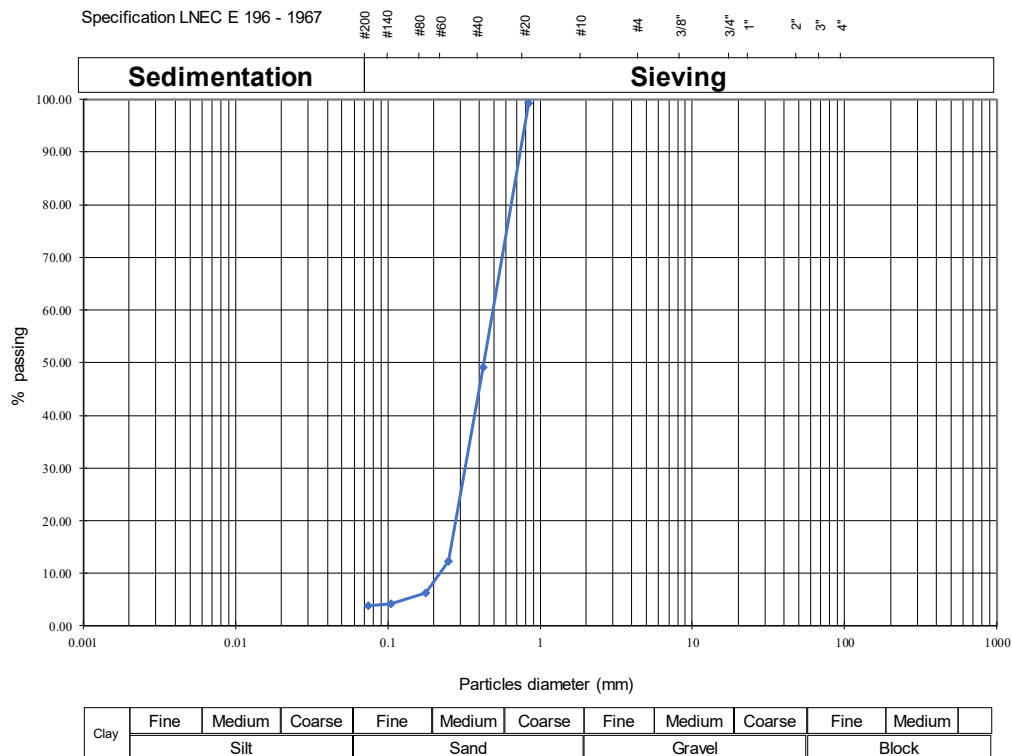


<b>d<sub>60</sub></b> = 0.4 mm	<b>Primary fraction:</b>	Sand (Sa)	97 %
<b>d<sub>30</sub></b> = 0.27 mm	<b>Coarse sand (cSa)</b>	(>0,63 to ≤2,0)	12 %
<b>d<sub>10</sub></b> = 0.17 mm	<b>Medium sand (mSa)</b>	(>0,20 to ≤0,63)	75 %
<b>U</b> = 2.35	<b>Fine sand (fSa)</b>	(>0,063 to ≤0,20)	10 %
<b>C<sub>c</sub></b> = 1.07	<b>Secondary fraction:</b>	Clay (cl)	3 %

## Particle Size Distribution Data Sheet

**Date:** 11/07/2019 **Mass before washing:** 599.43 g  
**Sample number:** 5588 **Mass after washing:** 580.67 g  
**Soil description:** cl' Sa  
**Borehole:** S1-1 (21,00 - 21,55 m)  
**Type of test:** Sieving

Sieve Number	Diameter [mm]	Soil retained [g]	Soil retained [%]	Soil Passing [%]
20	0.84	3.96	0.66	99.34
40	0.42	301.29	50.24	49.10
60	0.25	221.08	36.87	12.23
80	0.177	35.56	5.93	6.30
140	0.105	12	2.00	4.30
200	0.074	3.12	0.52	3.78
pan		3.9	0.65	3.13
washing		18.76	3.13	0.00
<b>SUM</b>		<b>599.67</b>	<b>100.00</b>	



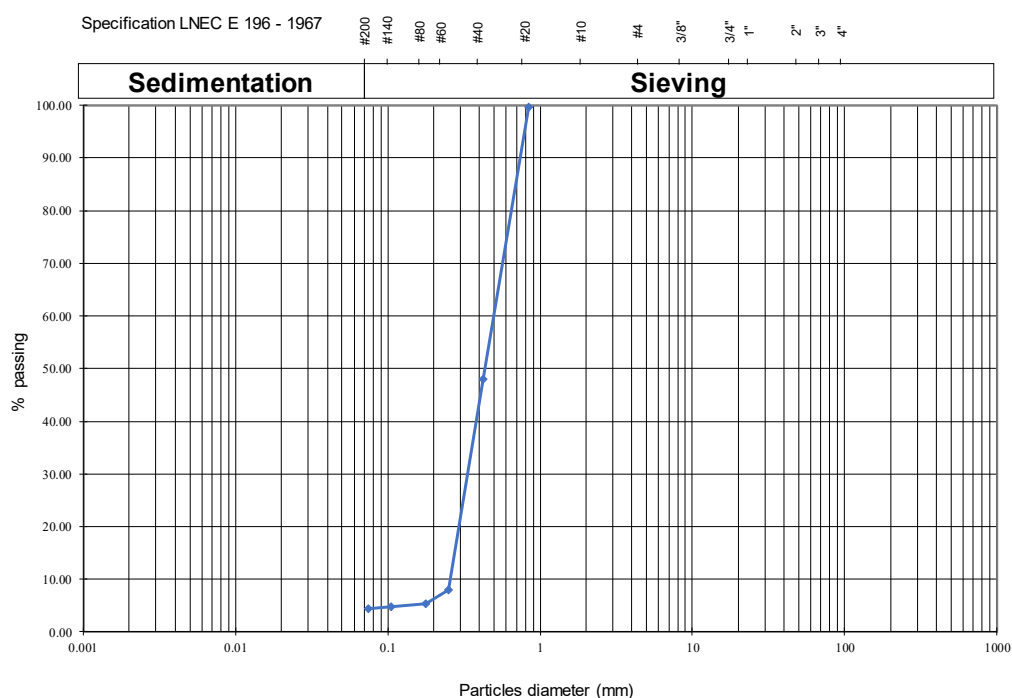
**d<sub>60</sub>** = 0.5 mm **Primary fraction:** Sand (Sa) 96 %  
**d<sub>30</sub>** = 0.32 mm  
**d<sub>10</sub>** = 0.21 mm **Coarse sand (cSa)** (>0,63 to ≤2,0) 30 %  
**U** = 2.38 **Medium sand (mSa)** (>0,20 to ≤0,63) 62 %  
**C<sub>c</sub>** = 0.98 **Fine sand (fSa)** (>0,063 to ≤0,20) 4 %  
**Secondary fraction:** 4 %



## Particle Size Distribution Data Sheet

**Date:** 15/07/2019 **Mass before washing:** 419.21 g  
**Sample number:** 5590 **Mass after washing:** 365.02 g  
**Soil description:** cl' Sa  
**Borehole:** S1-2 (6,50 - 7,00 m)  
**Type of test:** Sieving

Sieve Number	Diameter [mm]	Soil retained [g]	Soil retained [%]	Soil Passing [%]
20	0.84	13.82	3.30	96.70
40	0.42	208.61	49.83	46.87
60	0.25	99.14	23.68	23.19
80	0.177	22.75	5.43	17.76
140	0.105	8.95	2.14	15.62
200	0.074	4.11	0.98	14.64
pan		7.11	1.70	12.94
washing		54.19	12.94	0.00
<b>SUM</b>		<b>418.68</b>	<b>100.00</b>	



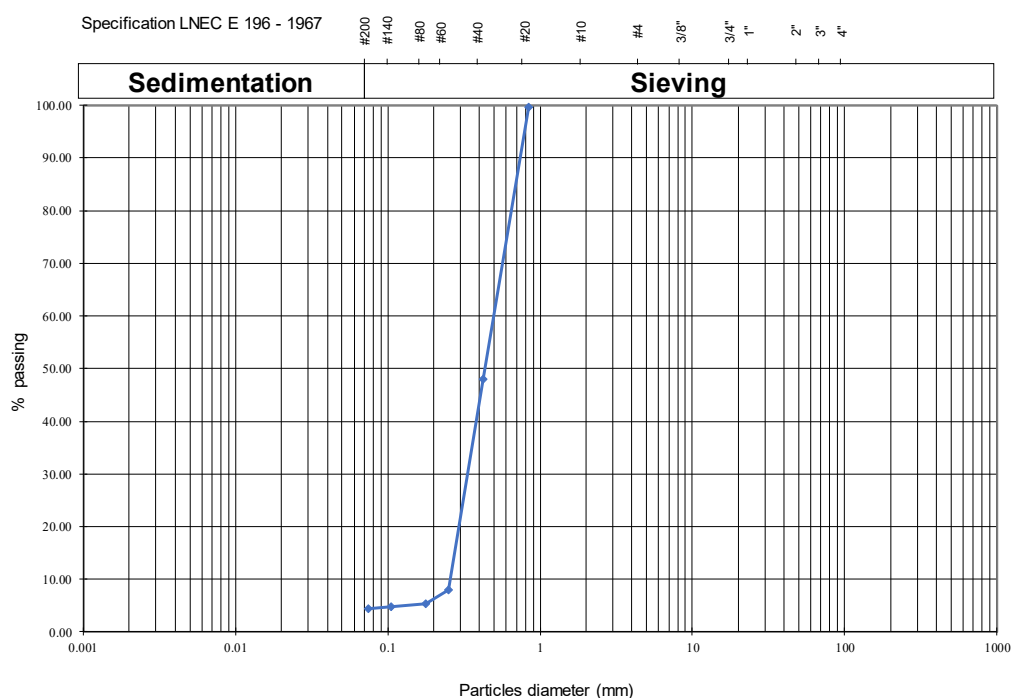
Clay	Fine	Medium	Coarse	Fine	Medium	Coarse	Fine	Medium	Coarse	Fine	Medium
	Silt			Sand			Gravel			Block	

**d<sub>60</sub>** = 0.5 mm **Primary fraction:** Sand (Sa) 85 %  
**d<sub>30</sub>** = 0.29 mm  
**d<sub>10</sub>** = < 0.063 mm **Coarse sand (cSa)** (>0,63 to ≤2,0) 28 %  
**U** = 7.94 **Medium sand (mSa)** (>0,20 to ≤0,63) 52 %  
**C<sub>c</sub>** = 2.67 **Fine sand (fSa)** (>0,063 to ≤0,20) 5 %  
**Secondary fraction:** Clay (cl) 15 %

## Particle Size Distribution Data Sheet

**Date:** 15/07/2019 **Mass before washing:** 391.57 g  
**Sample number:** 5592 **Mass after washing:** 375.92 g  
**Soil description:** cl' Sa  
**Borehole:** S1-2 (14,70 - 15,00 m)  
**Type of test:** Sieving

Sieve Number	Diameter [mm]	Soil retained [g]	Soil retained [%]	Soil Passing [%]
20	0.84	1.52	0.39	99.61
40	0.42	202.58	51.68	47.94
60	0.25	156.5	39.92	8.01
80	0.177	10.43	2.66	5.35
140	0.105	2.59	0.66	4.69
200	0.074	1.13	0.29	4.41
pan		1.62	0.41	3.99
washing		15.65	3.99	0.00
<b>SUM</b>		<b>392.02</b>	<b>100.00</b>	



Clay	Fine	Medium	Coarse	Fine	Medium	Coarse	Fine	Medium	Coarse	Fine	Medium
	Silt			Sand			Gravel			Block	

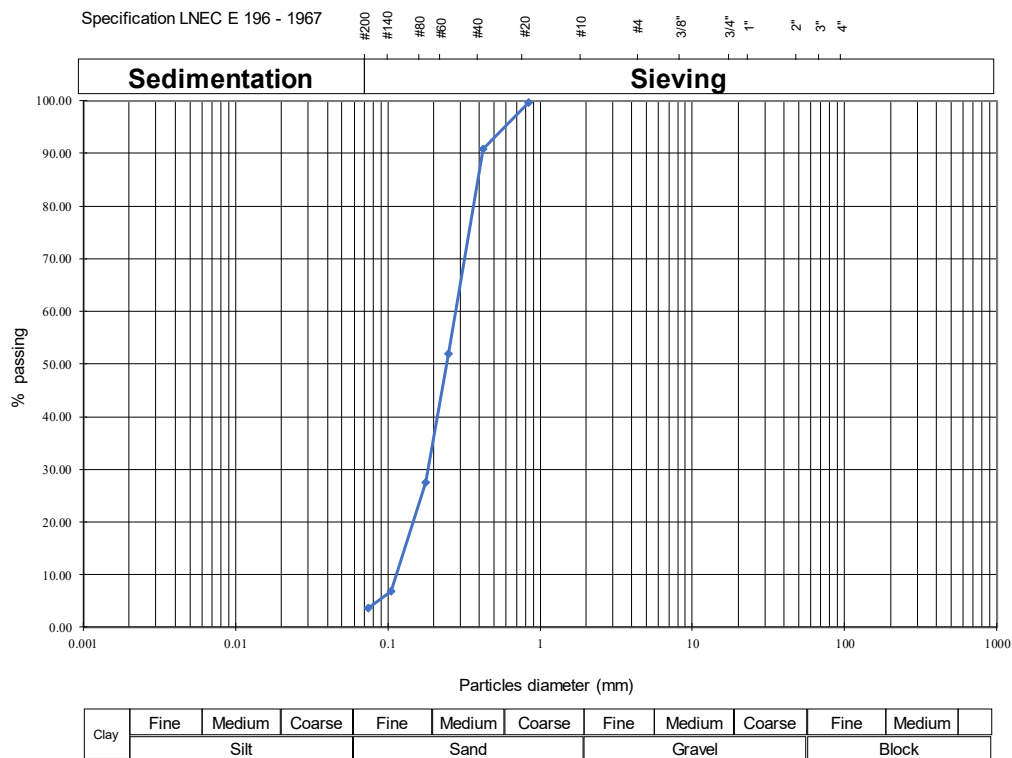
**d<sub>60</sub>** = 0.5 mm      Primary fraction:      Sand (Sa)      95.5 %  
**d<sub>30</sub>** = 0.31 mm  
**d<sub>10</sub>** = 0.15 mm      Coarse sand (cSa)      (>0,63 to ≤2,0)      27 %  
**U** = 3.33      Medium sand (mSa)      (>0,20 to ≤0,63)      66 %  
**C<sub>c</sub>** = 1.28      Fine sand (fSa)      (>0,063 to ≤0,20)      2.5 %  
  
 Secondary fraction:      Clay (cl)      4.5 %

## Particle Size Distribution Data Sheet

**Date:** 5/06/2019  
**Sample number:** 5593  
**Soil description:** cl' Sa  
**Borehole:** S2-1 (12,00 - 12,80 m)  
**Type of test:** Sieving

**Mass before washing:** 574.12 g  
**Mass after washing:** 570.39 g

Sieve Number	Diameter [mm]	Soil retained [g]	Soil retained [%]	Soil Passing [%]
20	0.84	1.96	0.34	99.66
40	0.42	50.42	8.78	90.88
60	0.25	223.23	38.88	51.99
80	0.177	140.1	24.40	27.59
140	0.105	119.29	20.78	6.81
200	0.074	18.19	3.17	3.65
Pan		17.2	3.00	0.65
washing		3.73	0.65	0.00
<b>SUM</b>		<b>574.12</b>	<b>100.00</b>	



**d<sub>60</sub>** = 0.29 mm      **Primary fraction:** Sand (Sa)      96 %  
**d<sub>30</sub>** = 0.19 mm  
**d<sub>10</sub>** = 0.12 mm      **Coarse sand (cSa)** (>0,63 to ≤2,0)      5 %  
**U** = 2.42      **Medium sand (mSa)** (>0,20 to ≤0,63)      60 %  
**C<sub>c</sub>** = 1.04      **Fine sand (fSa)** (>0,063 to ≤0,20)      31 %  
  
**Secondary fraction:** Clay (cl)      4 %

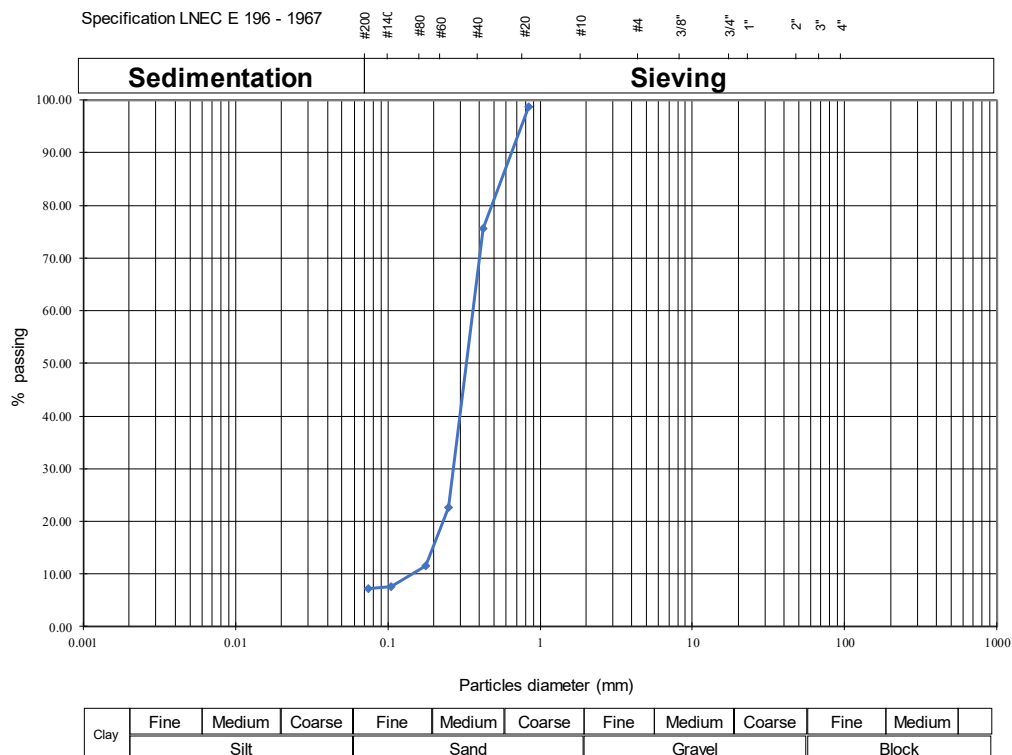


## Particle Size Distribution Data Sheet

**Date:** 11/07/2019  
**Sample number:** 5596  
**Soil description:** cl' Sa  
**Borehole:** S2-2 (10,00 - 11,30 m)  
**Type of test:** Sieving

**Mass before washing:** 427.61 g  
**Mass after washing:** 399.26 g

Sieve Number	Diameter [mm]	Soil retained [g]	Soil retained [%]	Soil Passing [%]
20	0.84	5.28	1.24	98.76
40	0.42	99.23	23.22	75.55
60	0.25	225.81	52.83	22.71
80	0.177	48.01	11.23	11.48
140	0.105	16.58	3.88	7.60
200	0.074	1.71	0.40	7.20
pan		2.43	0.57	6.63
washing		28.35	6.63	0.00
<b>SUM</b>		<b>427.4</b>	<b>100.00</b>	



<b>d<sub>60</sub></b> = 0.38 mm	<b>Primary fraction:</b>	Sand (Sa)	93 %
<b>d<sub>30</sub></b> = 0.28 mm			
<b>d<sub>10</sub></b> = 0.14 mm	<b>Coarse sand (cSa)</b>	(>0,63 to ≤2,0)	13 %
<b>U</b> = 2.71	<b>Medium sand (mSa)</b>	(>0,20 to ≤0,63)	75 %
<b>C<sub>c</sub></b> = 1.47	<b>Fine sand (fSa)</b>	(>0,063 to ≤0,20)	5 %
	<b>Secondary fraction:</b>	Clay (cl)	7 %

### Triaxial Data Sheet – Saturation/ Consolidation

**Date:** 02/05/2019  
**Sample number:** 5578\_50kPa  
**Soil description:** cl' Sa  
**Borehole:** S1-1 (13.50 - 14.10 m)  
**Type of test:** Consolidated undrained  
**Effective confining stress:**  $\sigma_3 = 50$  kPa

**Initial specimen height:**  $H_0 = 11.63$  cm  
**Initial specimen diameter:**  $D_0 = 6.0$  cm  
**Initial specimen volume:**  $V_0 = 328$  cm<sup>3</sup>  
**Specimen initial mass:**  $M_0 = 673.43$  g  
**Specimen initial density:**  $\rho = 2.0$  g/cm<sup>3</sup>  
**Initial water content:**  $w = 10$  %  
**Particles specific gravity:**  $\rho_s = 2.68$  g/cm<sup>3</sup>  
**Specimen initial void ratio:**  $e = 48$  %

**Final mass:**  $M = 726$  g  
**Final dry mass:**  $M_d = 611.53$  g  
**Final water content:**  $w = 18.7$  %

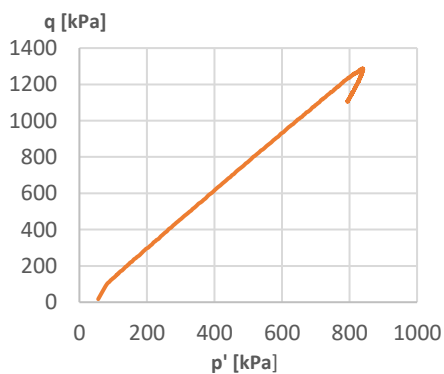
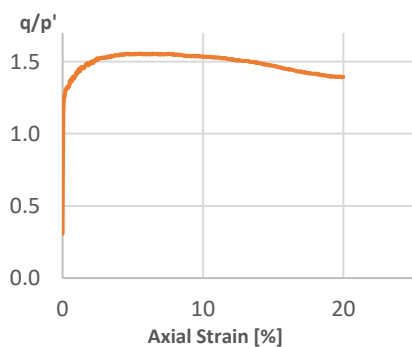
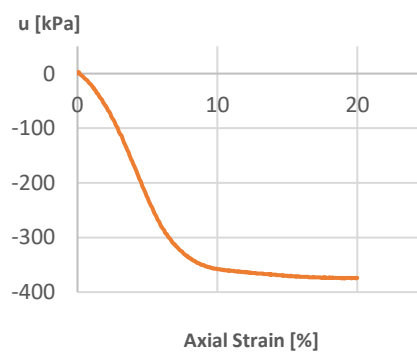
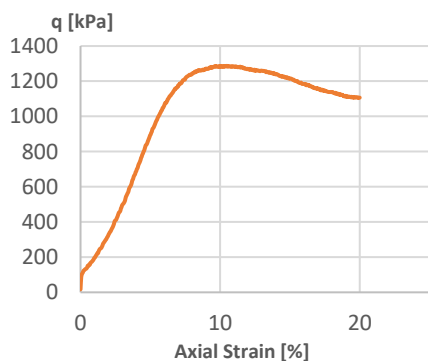
Time		Change in volume inside the cell chamber			Change in volume inside the specimen			Saturation		
Date	Time	Cell pressure [kPa]	Reading	$\Delta V$ [mm <sup>3</sup> ]	Back pressure [kPa]	Reading	$\Delta V$ [mm <sup>3</sup> ]	Pore pressure [kPa]	B-Value	Sr [%]
02/05/2019	16:30	0	0		0	0	0			
02/05/2019	16:30	20			10	0	0			
03/05/2019	09:00	20	-672	-672	10	-10914	0			
03/05/2019	11:25	20	-700	-28	10	0	0			
06/05/2019	08:30	20	-2924	-2224	10	-3733	-3733			
06/05/2019	10:30	20	-3146	-222	10	-4265	-532			
RAMP		Target: Cell pressure = 220 kPa Back pressure = 200 kPa								
07/05/2019	10:00	38	-5096	-1950	28	-6603	-2338			
08/05/2019	10:00	57	-7027	-1931	48	-10181	-3578			
09/05/2019	09:20	77	-7738	-711	67	-12420	-2239			
10/05/2019	09:50	98	-8859	-1121	88	-14467	-2047			
13/05/2019	11:00	158	-9691	-832	149	-17147	-2680			
13/05/2019	13:30	179	-10164	-473	168	-17150	-3			
14/05/2019	09:20	206	-11178	-1014	194	-17140	10			
15/05/2019	11:10	220	-12772	-1594	200	-16073	1067	194		
15/05/2019	11:10	240	-12772	0	BF	-16073	0	210	16/20	80 %
15/05/2019	11:35	240	-14383	-1611	220	-17691	-1618			
16/05/2019	10:35	240	-14383	0	220	-18253	-562	216		
16/05/2019	10:35	260	-14383	0	BF	-18253	0	232	16/20	80 %
16/05/2019	11:00	260	-14943	-560	240	-18324	-71			
17/05/2019	14:45	260	-14930	13	240	-18551	-227			
17/05/2019	15:10	260	-18136	-3206	240	-50222	-31671	flushing		
17/05/2019	15:20	260	-18136	0	240	0	50222			
17/05/2019	16:40	260	-18016	120	240	-1017	-1017	234		
17/05/2019	16:40	280	-18016	0	BF	-1017	0	252	18/20	90 %
17/05/2019	16:45	280	-18496	-480	260	-1079	-62			
20/05/2019	11:00	320	-19774	-1278	300	-2490	-1411			
20/05/2019	11:00	340	-20785	-1011	BF	-2490	0	295	20/20	100 %
20/05/2019	11:10	340	-20088	697	320	-2532	-42	315		
Consolidation		Target: Cell pressure = 370 kPa const. Back pressure = 320 kPa								
21/05/2019	10:10	348	-20785	-697	320	-2314	218	320		
22/05/2019	11:10	359	-21440	-655	320	-1976	338	320		
23/05/2019	09:45	369	-21833	-393	320	-1685	291	320		
23/05/2019	14:00	371	-21893	-60	320	-1633	52	320		
23/05/2019	16:00	371	-21877	16	320	-1622	11	320		
24/05/2019	09:06	369	-22275	-398	319	-1742	-120	320		

### Triaxial Data Sheet – Shearing

Date of shearing: 28/05/2019  
 Sample number: 5578\_50kPa  
 Strain rate: 0.05 mm/min

Cell pressure: 370 kPa  
 Back pressure: 320 kPa

Time	Pore Pressure	Axial Displacement	Axial Force	Axial Strain	Axial Stress	Eff. Axial Stress	Eff. Radial Stress	q	p'	q/p'
[min]	u [kPa]	v <sub>1</sub> [mm]	F [kN]	ε <sub>1</sub> [%]	σ <sub>1</sub> [kPa]	σ' <sub>1</sub> [kPa]	σ' <sub>3</sub> [kPa]	[kPa]	[kPa]	
0	320	0.0	1.1	0.0	387.1	67.1	50	17.1	55.7	0.31
20	302	1.0	1.6	0.9	550.8	248.8	69	179.8	128.9	1.39
40	273	2.0	1.9	1.7	658.4	385.4	98	287.4	193.8	1.48
60	234	3.0	2.3	2.6	794.6	560.6	137	423.6	278.2	1.52
80	186	4.0	2.8	3.5	956.2	770.2	185	585.2	380.1	1.54
100	133	5.0	3.4	4.3	1135.6	1002.6	238	764.6	492.9	1.55
120	82	6.0	3.9	5.2	1302.5	1220.5	289	931.5	599.5	1.55
140	39	7.0	4.3	6.0	1440.5	1401.5	332	1069.5	688.5	1.55
160	7	8.1	4.7	6.9	1536.5	1529.5	364	1165.5	752.5	1.55
180	-13	9.1	4.9	7.8	1608.0	1621.0	384	1237.0	796.3	1.55
200	-28	10.1	5.1	8.7	1634.0	1662.0	399	1263.0	820.0	1.54
220	-36	11.1	5.2	9.6	1654.0	1690.0	407	1283.0	834.7	1.54
240	-40	12.1	5.2	10.4	1657.6	1697.6	411	1286.6	839.9	1.53
260	-42	13.1	5.3	11.3	1650.4	1692.4	413	1279.4	839.5	1.52
280	-44	14.2	5.3	12.2	1639.6	1683.6	415	1268.6	837.9	1.51
300	-46	15.2	5.3	13.1	1628.9	1674.9	417	1257.9	836.3	1.50
320	-48	16.2	5.3	14.0	1609.8	1657.8	419	1238.8	831.9	1.49
340	-50	17.3	5.3	14.8	1591.8	1641.8	421	1220.8	827.9	1.47
360	-51	18.3	5.2	15.7	1561.2	1612.2	422	1190.2	818.7	1.45
380	-53	19.3	5.2	16.6	1537.4	1590.4	424	1166.4	812.8	1.44
400	-54	20.3	5.2	17.5	1519.5	1573.5	425	1148.5	807.8	1.42
420	-54	21.3	5.2	18.3	1499.2	1553.2	425	1128.2	801.1	1.41
440	-54	22.3	5.2	19.2	1483.8	1537.8	425	1112.8	795.9	1.40



### Triaxial Data Sheet – Saturation/ Consolidation

**Date:** 02/05/2019  
**Sample number:** 5578\_280kPa  
**Borehole:** S1-1 (13.50 - 14.10 m)  
**Soil Description:** cl' Sa  
**Type of test;** Consolidated undrained  
**Effective confining stress:**  $\sigma_3 = 280$  kPa

**Initial specimen height:**  $H_0 = 10,7$  cm  
**Initial specimen diameter:**  $D_0 = 6,0$  cm  
**Initial specimen volume:**  $V_0 = 302$  cm<sup>3</sup>  
**Specimen initial mass:**  $M_0 = 648,81$  g  
**Specimen initial density:**  $\rho = 2.1$  g/cm<sup>3</sup>  
**Initial water content:**  $W = 16$  %  
**Particles specific gravity:**  $\rho_s = 2.68$  g/cm<sup>3</sup>  
**Specimen initial void ratio:**  $e = 45$  %

**Final mass:**  $M = 659,46$  g  
**Final dry mass:**  $M_d = 558,36$  g  
**Final water content:**  $w = 18$  %

Time		Change in volume inside the cell chamber			Change in volume inside the specimen			Saturation		
Date	Time	Cell pressure [kPa]	Reading	$\Delta V$ [mm]	Back pressure [kPa]	Reading	$\Delta V$ [mm]	Pore pressure [kPa]	B-Value	Sr [%]
02/05/2019	16:30	0	0	0	0	0	0			
02/05/2019	16:30	20	0	0	10	0	0			
03/05/2019	09:00	20	-994	-994	10	-3231	-3231			
06/05/2019	08:30	20	-2858	-1864	10	-6483	-3252			
06/05/2019	10:40	20	-2959	-101	10	-7282	-799			
RAMP		Target: Cell pressure = 220 kPa Back pressure = 200 kPa								
07/05/2019	10:00	39	-3977	-1018	29	-10729	-3447			
08/05/2019	10:00	58	-5480	-1503	48	-14113	-3384			
09/05/2019	09:20	78	-6102	-622	68	-15928	-1815			
10/05/2019	09:50	98	-7131	-1029	89	-17754	-1826			
13/05/2019	11:00	158	-8120	-989	148	-20310	-2556			
13/05/2019	11:30	160	-8187	-67	150	-20317	-7			
13/05/2019	11:30	180	-	0	BF	-	0			
13/05/2019	15:30	179	-8909	-722	168	-20315	2			
14/05/2019	9:30	209	-9652	-743	197	-20571	-256			
15/05/2019	11:10	220	-11520	-1868	200	-19079	1492			
15/05/2019	11:10	220	-	0	200	-	0	197	19/20	95 %
15/05/2019	11:10	240	-	0	BF	-	0	216		
15/05/2019	11:45	240	-12125	-605	220	-19597	-518			
16/05/2019	11:00	240	-12432	-307	220	-19769	-172			
16/05/2019	11:00	260	-12771	-339	240	-19859	-90			
17/05/2019	14:45	260	-12788	-17	240	-20142	-283			
17/05/2019	15:15	260	-16897	-4109	240	-38002	-17860			
17/05/2019	17:00	280	-16737	160	259	-38239	-237			
20/05/2019	11:00	320	-19172	-2435	300	-30923	7316			
20/05/2019	11:10	340	-18491	681	320	-38965	-8042			
Consolidation		Target: Cell pressure = 600 kPa const. Back pressure = 320 kPa								
21/05/2019	10:10	357	-19861	-1370	320	-38030	935			
22/05/2019	11:10	378	-21075	-1214	320	-37191	839			
23/05/2019	09:50	396	-21844	-769	320	-36693	498			
24/05/2019	09:10	416	-23045	-1201	320	-36278	415			
27/05/2019	11:20	477	-25541	-2496	320	-35002	1276			
28/05/2019	09:30	496	-26508	-967	320	-34664	338			
28/05/2019	17:40	502	-26495	13	320	-34511	153			
29/05/2019	10:20	520	-26906	-411	320	-34462	49	325		
30/05/2019	10:00	549	-27696	-790	320	-34049	413	325		
31/05/2019	11:15	581	-28455	-759	320	-33608	441	326		
31/05/2019	11:30	580	0	28455	320	0	-			
03/06/2019	10:20	600	-611	-611	320	712	712	320		
03/06/2019	11:25	600	-391	-1370	320	-1401	-2113	320		

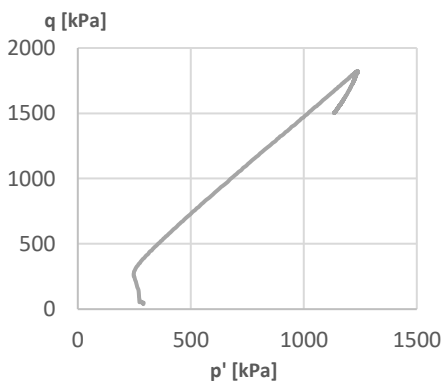
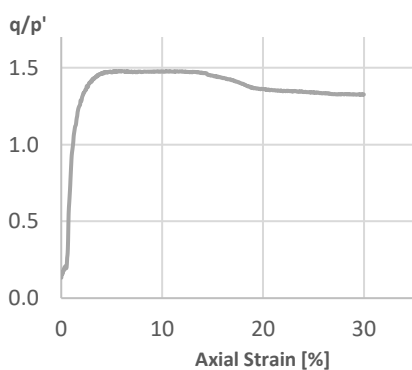
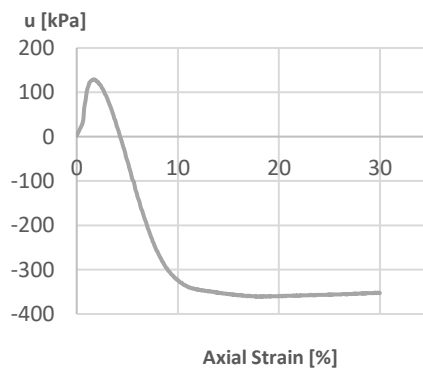
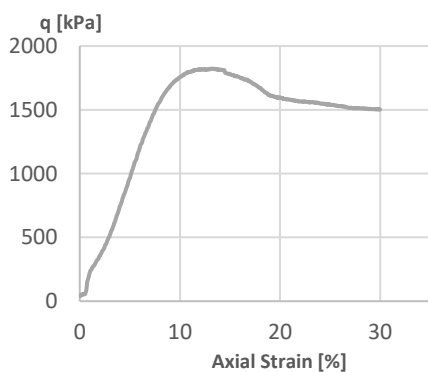


### Triaxial Data Sheet – Shearing

Date of testing: 04/06/2019  
 Sample number: 5578-280kPa  
 Strain rate: 0.05 mm/min

Cell pressure: 600 kPa  
 Back pressure: 320 kPa

Time	Pore Pressure	Axial Displacement	Axial Force	Axial Strain	Axial Stress	Eff. Axial Stress	Eff. Radial Stress	q	p'	q/p'
[min]	u [kPa]	v <sub>1</sub> [mm]	F [kN]	ε <sub>1</sub> [%]	σ <sub>1</sub> [kPa]	σ' <sub>1</sub> [kPa]	σ' <sub>3</sub> [kPa]	[kPa]	[kPa]	
0	320	0.00	1.10	0.00	387.1	67.10	50	17.104	55.7	0.13
20	415	1.02	2.32	0.95	813.3	398.3	186	212.3	256.8	0.83
40	447	2.02	2.72	1.89	942.4	495.4	154	341.4	267.8	1.27
60	414	3.06	3.19	2.86	1094.4	680.4	187	493.4	351.5	1.40
80	359	4.03	3.78	3.76	1285.1	926.1	242	684.1	470.0	1.46
100	289	5.06	4.46	4.73	1503.7	1214.7	312	902.7	612.9	1.47
120	214	6.09	5.18	5.69	1726.4	1512.4	387	1125.4	762.1	1.48
140	146	7.03	5.82	6.57	1922.6	1776.6	454	1322.6	894.9	1.48
160	84	8.04	6.40	7.52	2091.9	2007.9	517	1490.9	1014.0	1.47
180	40	9.02	6.87	8.43	2225.8	2185.8	561	1624.8	1102.6	1.47
200	9	10.03	7.24	9.38	2319.9	2310.9	592	1718.9	1165.0	1.48
220	-10	11.10	7.48	10.37	2372.1	2382.1	611	1771.1	1201.4	1.47
240	-22	12.12	7.67	11.32	2406.9	2428.9	623	1805.9	1225.0	1.47
260	-26	13.14	7.80	12.28	2419.1	2445.1	627	1818.1	1233.0	1.47
280	-29	14.14	7.90	13.22	2423.5	2452.5	630	1822.5	1237.5	1.47
300	-33	15.14	7.95	14.15	2413.2	2446.2	634	1812.2	1238.1	1.46
320	-36	16.18	7.91	15.13	2375.4	2411.4	637	1774.4	1228.5	1.44
340	-37	17.21	7.91	16.09	2347.0	2384.0	637	1747.0	1219.3	1.43
360	-40	18.22	7.91	17.03	2319.7	2359.7	641	1718.7	1213.9	1.42
380	-41	19.26	7.84	18.00	2272.9	2313.9	641	1672.9	1198.6	1.40
400	-40	20.26	7.73	18.94	2216.6	2256.6	640	1616.6	1178.9	1.37
420	-40	21.27	7.75	19.88	2196.6	2236.6	641	1595.6	1172.9	1.36
440	-39	22.31	7.80	20.85	2183.8	2222.8	640	1582.8	1167.6	1.36
460	-38	23.32	7.85	21.79	2170.1	2208.1	638	1570.1	1161.4	1.35
480	-38	24.29	7.91	22.70	2162.2	2200.2	638	1562.2	1158.7	1.35
500	-37	25.34	7.99	23.68	2157.4	2194.4	638	1556.4	1156.8	1.35
520	-37	26.38	8.04	24.66	2143.6	2180.6	638	1542.6	1152.2	1.34
540	-36	27.38	8.11	25.59	2134.3	2170.3	637	1533.3	1148.1	1.34
560	-35	28.41	8.18	26.55	2125.1	2160.1	636	1524.1	1144.0	1.33
580	-35	29.41	8.24	27.49	2113.6	2148.6	636	1512.6	1140.2	1.33
600	-34	30.41	8.35	28.42	2113.1	2147.1	635	1512.1	1139.0	1.33
620	-33	31.43	8.44	29.37	2107.6	2140.6	634	1506.6	1136.2	1.33



### Triaxial Data Sheet – Saturation/ Consolidation

**Date:** 02/05/2019  
**Sample number:** 5578\_500kPa  
**Soil description:** cl' Sa  
**Borehole:** S1-1 (13.50-14.10 m)  
**Type of test:** Consolidated undrained  
**Effective confining stress:**  $\sigma_3 = 500$  kPa

**Initial specimen height:**  $H_0 = 11,48$  cm  
**Initial specimen diameter:**  $D_0 = 6,0$  cm  
**Initial specimen volume:**  $V_0 = 333$  cm<sup>3</sup>  
**Specimen initial mass:**  $M_0 = 673,43$  g  
**Specimen initial density:**  $\rho = 2.05$  g/cm<sup>3</sup>  
**Initial water content:**  $W = 20$  %  
**Particles specific gravity:**  $\rho_s = 2.68$  g/cm<sup>3</sup>  
**Specimen initial void ratio:**  $e = 50$  %

**Final mass:**  $M = 694,99$  g  
**Final dry mass:**  $M_d = 588,58$  g  
**Final water content:**  $w = 24,5$  %

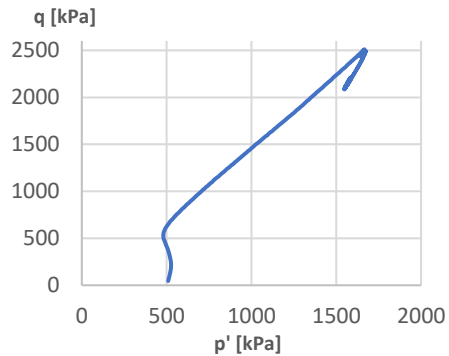
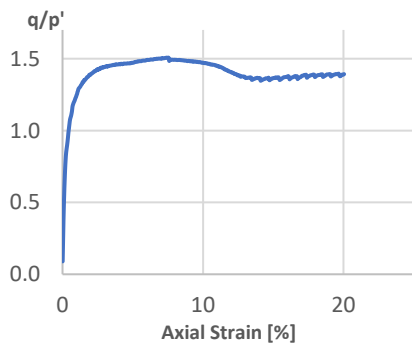
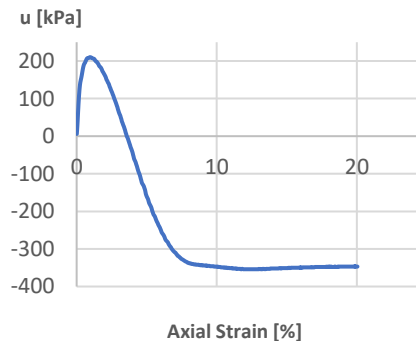
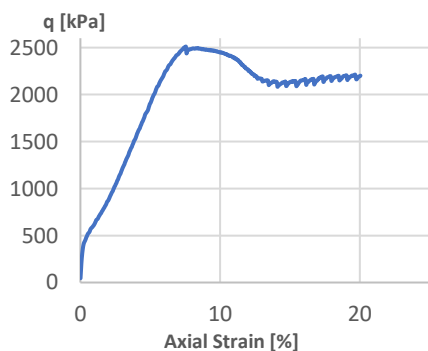
Time		Change in volume inside the cell chamber			Change in volume inside the specimen			Saturation		
Date	Time	Cell pressure [kPa]	Reading	$\Delta V$ [mm]	Back pressure [kPa]	Reading	$\Delta V$ [mm]	Pore pressure [kPa]	B-Value	Sr [%]
02/05/2019	16:30	0	0	0	0	0	0			
02/05/2019	16:30	20	0	0	10	0	0			
03/05/2019	09:00	20	-643	-643	10	-7415	-7415			
06/05/2019	08:30	20	-1595	-952	10	-13316	-5901			
06/05/2019	10:40	20	-1825	-230	10	-14319	-1003			
RAMP		Target: Cell pressure = 220 kPa Back pressure = 200 kPa								
07/05/2019	10:00	39	-1595	230	28	-20161	-5842			
07/05/2019	14:00	42	-1804	-209	31	-21242	-1081			
08/05/2019	10:00	58	-3027	-1223	48	-24937	-3695			
09/05/2019	09:20	78	-3449	-422	67	-24937	0			
10/05/2019	09:50	99	-4364	-915	88	-27895	-2958			
13/05/2019	11:30	159	-4714	-350	149	-30736	-2841			
13/05/2019	15:30	179	-5401	-687	166	-34592	-3856			
14/05/2019	09:30	211	-6570	-1169	196	-34759	-167			
15/05/2019	11:10	220	-7348	-778	200	-34348	411			
15/05/2019	11:10	240	-	0	200	-	0	198	18/20	90 %
15/05/2019	11:10	240	-	0	BF	-	0	216		
16/05/2019	10:50	260	-7849	-501	220	-34402	-54	218	18/20	90 %
16/05/2019	10:50	260	-	0	BF	-	0	236		
16/05/2019	11:05	260	-8649	-800	240	-35357	-955			
17/05/2019	14:45	260	-8614	35	240	-78822	-43465			
17/05/2019	15:15	260	-12848	-4234	240	-78822	0			
17/05/2019	16:45	260	-12472	376	240	-79508	-686	238	18/20	90 %
17/05/2019	16:45	280	-12855	-383	BF	-	0	256		
17/05/2019	16:50	280	-	0	259	-79574	-66			
20/05/2019	11:00	320	-14343	-1488	300	-80782	-1208	298	20/20	100 %
20/05/2019	11:00	340	-	0	BF	-	0	318		
20/05/2019	11:10	340	-14868	-525	320	-80932	-150			
Consolidation		Target: Cell pressure = 820 kPa const. Back pressure = 320 kPa								
21/05/2019	10:10	367	-16933	-2065	320	-79420	1512	320		
22/05/2019	11:10	398	-18465	-1532	320	-78354	1066	320		
23/05/2019	09:50	427	-19412	-947	320	-77740	614	320		
24/05/2019	09:10	455	-20803	-1391	320	-77366	374	317		
27/05/2019	11:20	549	-23623	-2820	320	-75931	1435	320		
28/05/2019	09:30	577	-24742	-1119	320	-75594	337	320		
28/05/2019	17:40	586	-24564	178	320	-75387	207	320		
29/05/2019	10:25	615	-25130	-566	320	-74984	403	320		
30/05/2019	10:00	654	-25920	-790	320	-74466	518	320		
31/05/2019	11:15	697	-26826	-906	320	-74001	465	320		
03/06/2019	09:40	813	-30283	-3457	320	-72324	1677	320		
04/06/2019	10:20	819	-31283	-2065	320	-71819	505	320		
05/06/2019	10:25	820	-34353	-1532	320	-71750	69	317		
05/06/2019	11:05	820	-34267	-947	320	-71741	9	320		

### Triaxial Data Sheet – Shearing

Date of testing: 0/06/2019  
 Sample number: 5578\_500kPa  
 Strain rate: 0.05 mm/min

Cell pressure: 820 kPa  
 Back pressure: 320 kPa

Time	Pore Pressure	Axial Displacement	Axial Force	Axial Strain	Axial Stress	Eff. Axial Stress	Eff. Radial Stress	q	p'	q/p'
[min]	u [kPa]	v <sub>1</sub> [mm]	F [kN]	ε <sub>1</sub> [%]	σ <sub>1</sub> [kPa]	σ' <sub>1</sub> [kPa]	σ' <sub>3</sub> [kPa]	[kPa]	[kPa]	
0	320	0	1.09	0.00	387.104	67.104	50	17.1	55.7	0.09
20	528	0.99	4.02	0.86	1410	882.3	292	590.3	488.8	1.21
40	500	2.02	4.70	1.76	1633	1133.3	321	812.3	591.8	1.37
60	428	3.00	5.51	2.62	1896	1468.3	393	1075.3	751.4	1.43
80	336	3.97	6.40	3.46	2186	1850.5	485	1365.5	940.2	1.45
100	236	4.97	7.37	4.33	2494	2257.9	585	1672.9	1142.6	1.46
120	141	5.95	8.34	5.18	2796	2654.8	680	1974.8	1338.3	1.48
140	64	6.97	9.24	6.07	3068	3004.0	757	2247.0	1506.0	1.49
160	13	7.98	9.86	6.95	3245	3232.1	808	2424.1	1616.0	1.50
180	-14	8.97	10.13	7.82	3303	3317.4	835	2482.4	1662.5	1.49
200	-22	10.01	10.23	8.72	3302	3323.9	842	2481.9	1669.3	1.49
220	-26	11.04	10.29	9.61	3289	3314.6	847	2467.6	1669.5	1.48
240	-30	12.08	10.25	10.52	3242	3272.3	851	2421.3	1658.1	1.46
260	-32	13.11	10.12	11.42	3170	3202.1	853	2349.1	1636.0	1.44
280	-34	14.10	9.82	12.28	3045	3079.2	854	2225.2	1595.7	1.39
300	-34	15.11	9.65	13.16	2965	2999.0	855	2144.0	1569.7	1.37
320	-32	16.15	9.72	14.06	2956	2987.6	853	2134.6	1564.5	1.36
340	-31	17.14	9.80	14.93	2948	2979.2	851	2128.2	1560.4	1.36
360	-30	18.21	10.00	15.87	2974	3004.2	851	2153.2	1568.7	1.37
380	-29	19.21	9.94	16.73	2926	2955.3	849	2106.3	1551.1	1.36
400	-28	20.21	10.26	17.60	2991	3018.9	848	2170.9	1571.6	1.38
420	-28	21.23	10.48	18.49	3020	3048.3	848	2200.3	1581.4	1.39
440	-27	22.24	10.58	19.37	3017	3044.0	848	2196.0	1580.0	1.39



### Triaxial Data Sheet – Saturation/ Consolidation

**Date:** 27/05/2019  
**Sample number:** 5593\_50kPa  
**Soil description:** cl' Sa  
**Borehole:** S2-1 (12.0 – 12.80 m)  
**Type of test:** Consolidated undrained  
**Effective confining stress:** 50 kPa

**Initial specimen height:**  $H_0 = 12.2$  cm  
**Initial specimen diameter:**  $D_0 = 7.53$  cm  
**Initial specimen volume:**  $V_0 = 543.2$  cm<sup>3</sup>  
**Specimen initial mass:**  $M_0 = 948.21$  g  
**Specimen initial density:**  $\rho = 1.73$  g/cm<sup>3</sup>  
**Initial water content:**  $W = 18$  %  
**Particles specific gravity:**  $\rho_s = 2.68$  g/cm<sup>3</sup>  
**Specimen initial void ratio:**  $e = 81$  %

**Final mass:**  $M = 954.57$  g  
**Final dry mass:**  $M_d = 801.77$  g  
**Final water content:**  $W = 19$  %

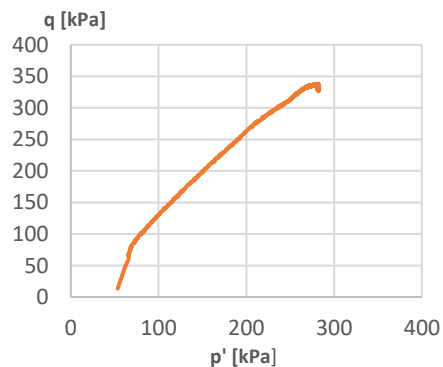
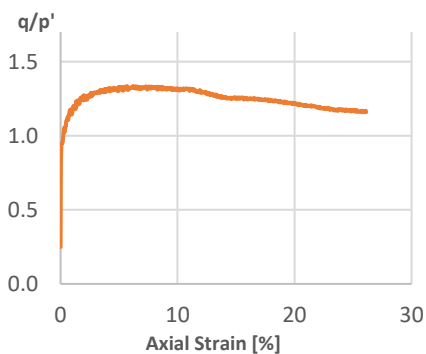
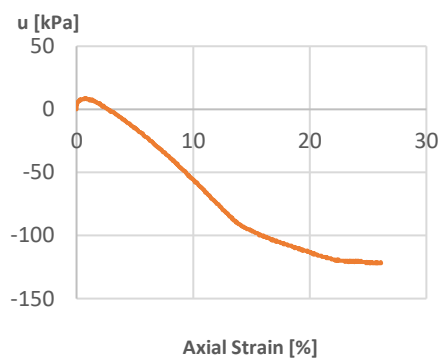
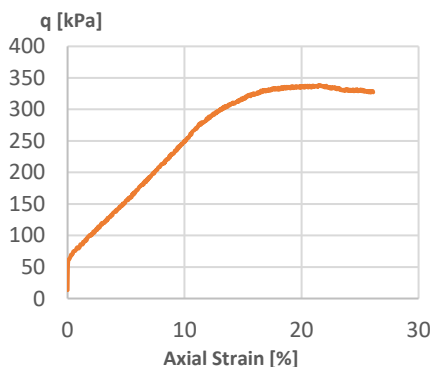
Time		Change in volume inside the cell chamber			Change in volume inside the specimen			Saturation		
Date	Time	Cell pressure [kPa]	Reading	$\Delta V$ [mm <sup>3</sup> ]	Back pressure [kPa]	Reading	$\Delta V$ [mm <sup>3</sup> ]	Pore pressure [kPa]	B-Value	Sr [%]
27/05/19	17:30	20	0	0	10	0	0			
27/05/19	17:35	20	-3391	0	10	-2222	-2222			
28/05/19	9:35	20	-5765	-7415	10	-5209	-2987			
28/05/19	11:30	20	-5765	-5901	10	5219	10428			
RAMP 20 kPa/d		Target: Cell pressure = 160 kPa Back pressure = 150 kPa								
29/05/19	10:30	37	-7582	20161	27	-13666	-18885			
30/05/19	10:00	56	-9553	-3391	46	-20138	-6472			
31/05/19	11:15	77	-11349	-2374	67	-25239	-5101			
03/06/19	9:40	136	-15596	0	126	-34330	-9091			
04/06/19	10:20	156	-17247	-1817	146	-36224	-1894			
05/06/19	10:35	160	-20833	-1971	150	-30226	5998			
05/06/19	11:20	160	0	-1796	150	0	30226			
05/06/19	11:50	160	-446	-4247	150	619	619	150	17/20	85 %
05/06/19	11:50	180	-	-1651	BF	-	0	167		
RAMP 30 kPa/d		Target: Cell pressure = 300 kPa Back pressure = 290 kPa								
05/06/19	12:15	180	-1747	-1301	165	640	-18885			
06/06/19	11:15	200	-3693	-1946	192	195	-6472			
07/06/19	10:15	235	-6096	-2403	222	-1170	-5101			
11/06/19	10:20	300	-13209	-7113	290	-3739	-9091	290	17/20	85 %
11/06/19	10:20	320	-	0	BF	-	-1894	307		
11/06/19	10:35	320	-13602	-393	310	-3945	5998			
12/06/19	11:35	320	-15105	-1503	310	-4251	30226	310	17/20	85%
12/06/19	11:35	340	-	0	BF	-	619	327		
12/06/19	11:55	340	-16627	-1522	320	-3132	0			
12/06/19	16:30	340	-26672	-10045	320	-28505	21			
12/06/19	10:30	360	-28817	-2145	350	-30158	-445			
14/06/19	10:35	360	-28824	-7	350	-30171	-1365	350	19/20	95 %
14/06/19	10:35	380	-	0	BF	-	-2569	369		
14/06/19	10:35	380	-29175	-351	370	-30265	0			
14/06/19	11:10	380	-29253	-78	370	-30245	-206			
14/06/19	11:20	380	-29301	-48	370	0	-306			
Consolidation		Target: Cell pressure = 420 kPa Back pressure = 370 kPa								
17/06/19	11:15	420	-37679	-8378	370	2555	2555			
17/06/19	11:30	420	-37700	-21	370	2560	5			

### Triaxial Data Sheet – Shearing

Date of shearing: 18/06/2019  
 Sample number: 5593\_50kPa  
 Strain rate: 0.05 mm/min

Cell pressure: 420 kPa  
 Back pressure: 370 kPa

Time	Pore Pressure	Axial Displacement	Axial Force	Axial Strain	Axial Stress	Eff. Axial Stress	Eff. Radial Stress	q	p'	q/p'
[min]	u [kPa]	v <sub>1</sub> [mm]	F [kN]	ε <sub>1</sub> [%]	σ <sub>1</sub> [kPa]	σ' <sub>1</sub> [kPa]	σ' <sub>3</sub> [kPa]	[kPa]	[kPa]	
0	370	0.0	1.93	0.00	432.31	62.31	49.00	13.31	53.44	0.25
20	379	1.0	2.3	0.8	501.9	122.9	42	80.9	69.0	1.17
40	376	2.0	2.3	1.7	514.3	138.3	45	93.3	76.1	1.23
60	371	3.0	2.4	2.5	531.9	160.9	50	110.9	87.0	1.28
80	367	4.0	2.5	3.3	543.5	176.5	54	122.5	94.8	1.29
100	361	5.1	2.6	4.1	558.6	197.6	60	137.6	105.9	1.30
120	355	6.1	2.7	5.0	576.4	221.4	66	155.4	117.8	1.32
140	349	7.1	2.8	5.8	591.3	242.3	72	170.3	128.8	1.32
160	342	8.1	2.9	6.7	607.8	265.8	79	186.8	141.3	1.32
180	336	9.2	3.0	7.5	623.4	287.4	85	202.4	152.5	1.33
200	329	10.2	3.1	8.3	636.8	307.8	92	215.8	163.9	1.32
220	322	11.2	3.2	9.2	655.4	333.4	99	234.4	177.1	1.32
240	314	12.2	3.3	10.0	669.4	355.4	107	248.4	189.8	1.31
260	307	13.2	3.4	10.9	688.3	381.3	114	267.3	203.1	1.32
280	299	14.2	3.5	11.7	700.8	401.8	122	279.8	215.3	1.30
300	291	15.2	3.6	12.5	712.1	421.1	130	291.1	227.0	1.28
320	283	16.3	3.7	13.3	721.9	438.9	138	300.9	238.3	1.26
340	278	17.3	3.8	14.2	731.4	453.4	143	310.4	246.5	1.26
360	274	18.3	3.9	15.0	737.8	463.8	147	316.8	252.6	1.25
380	270	19.3	3.9	15.8	744.1	474.1	151	323.1	258.7	1.25
400	267	20.3	4.0	16.7	751.1	484.1	154	330.1	264.0	1.25
420	264	21.3	4.1	17.5	752.5	488.5	157	331.5	267.5	1.24
440	262	22.4	4.1	18.3	753.1	491.1	159	332.1	269.7	1.23
460	259	23.4	4.2	19.2	757.2	498.2	162	336.2	274.1	1.23
480	257	24.4	4.2	20.0	757.6	500.6	164	336.6	276.2	1.22
500	254	25.4	4.3	20.8	758.0	504.0	167	337.0	279.3	1.21
520	252	26.4	4.3	21.6	759.3	507.3	169	338.3	281.8	1.20
540	251	27.4	4.3	22.5	754.0	503.0	170	333.0	281.0	1.18
560	249	28.5	4.4	23.3	752.0	503.0	172	331.0	282.3	1.17
580	250	29.5	4.4	24.2	752.3	502.3	171	331.3	281.4	1.18
600	248	30.5	4.5	25.0	750.8	502.8	173	329.8	282.9	1.17



### Triaxial Data Sheet – Saturation/ Consolidation

**Date:** 27/05/2019  
**Sample number:** 5593\_250kPa  
**Soil description:** cl' Sa  
**Borehole:** S2-1 (12.0 – 12.80 m)  
**Type of test:** Consolidated undrained  
**Effective confining stress:** 250 kPa

**Initial specimen height:**  $H_0 = 13.1$  cm  
**Initial specimen diameter:**  $D_0 = 7.5$  cm  
**Initial specimen volume:**  $V_0 = 578.7$  cm<sup>3</sup>  
**Specimen initial mass:**  $M_0 = 983$  g  
**Specimen initial density:**  $\rho = 1.70$  g/cm<sup>3</sup>  
**Initial water content:**  $W = 16$  %  
**Particles specific gravity:**  $\rho_s = 2.68$  g/cm<sup>3</sup>  
**Specimen initial void ratio:** 83 %

**Final mass:**  $M = 1000$  g  
**Final dry mass:**  $M_d = 847$  g  
**Final water content:**  $W = 18$  %

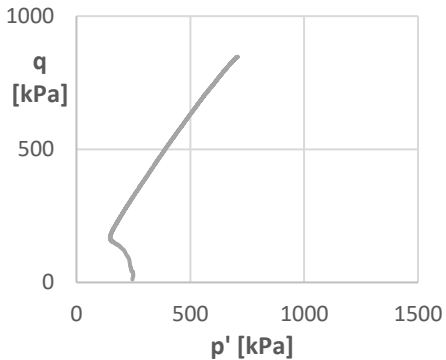
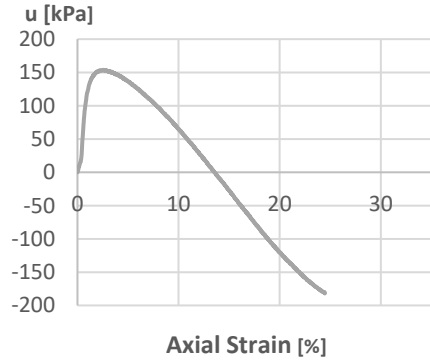
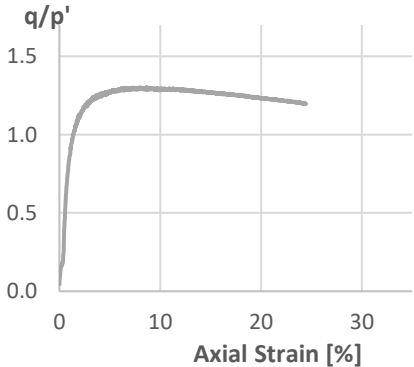
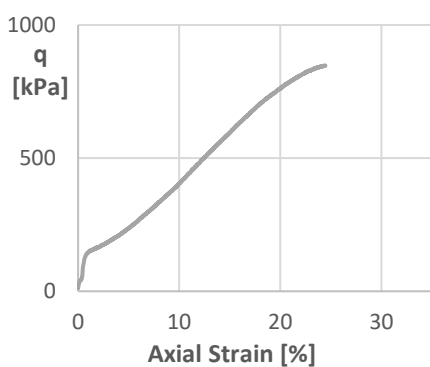
Time		Change in volume inside the cell chamber			Change in volume inside the specimen			Saturation		
Date	Time	Cell pressure [kPa]	Reading	$\Delta V$ [mm <sup>3</sup> ]	Back pressure [kPa]	Reading	$\Delta V$ [mm <sup>3</sup> ]	Pore pressure [kPa]	B-Value	Sr [%]
27/05/19	17:30	20			10					
27/05/19	17:35	20			10					
28/05/19	9:35	20			10					
28/05/19	11:30	20			10					
RAMP 20 kPa/d										
29/05/19	10:30	39			27					
30/05/19	10:00	56			46					
31/05/19	11:15	77			67					
03/06/19	9:40	135			126					
04/06/19	10:20	157			146					
05/06/19	10:35	160			150					
05/06/19	11:20	160			150					
05/06/19	11:50	160			150			150	17/20	75 %
05/06/19	11:50	180			BF	-		165		
RAMP 30 kPa/d Target: Cell pressure = 300 kPa Back pressure = 290 kPa										
05/06/19	12:15	180			165					
06/06/19	11:15	200			192					
07/06/19	10:15	235			222					
11/06/19	10:20	300			290			290	18/20	90 %
11/06/19	10:20	320			BF			305		
11/06/19	10:35	320			310					
12/06/19	11:35	320			310			310	19/20	95 %
12/06/19	11:35	340			BF			327		
12/06/19	11:55	340			320					
12/06/19	16:30	340			320					
12/06/19	10:30	360			350					
14/06/19	10:35	360			350					
14/06/19	10:35	380			370					
Consolidation Target: Cell pressure = 620 kPa Back pressure = 370 kPa										
17/06/19	11:15	420			370					
17/06/19	11:30	420			370					
18/06/19	10:30	458			370					
19/06/19	10:30	488			370					
20/06/19	9:30	506			370					
21/06/19	11:40	541			370					
24/06/19	11:15	570			370					
25/06/19	11:00	601			370					
26/06/19	08:10	620			370					

### Triaxial Data Sheet – Shearing

Date of shearing: 26/06/2019  
 Sample number: 5593\_250kPa  
 Strain rate: 0.05 mm/min

Cell pressure: 620 kPa  
 Back pressure: 370 kPa

Time	Pore Pressure	Axial Displacement	Axial Force	Axial Strain	Axial Stress	Eff. Axial Stress	Eff. Radial Stress	q	p'	q/p'
[min]	u [kPa]	v <sub>1</sub> [mm]	F [kN]	ε <sub>1</sub> [%]	σ <sub>1</sub> [kPa]	σ' <sub>1</sub> [kPa]	σ' <sub>3</sub> [kPa]	[kPa]	[kPa]	
0	320	0.00	1.10	0.00	387.1	67.10	50	17.104	55.7	0.04
20	401	0.52	3.03	0.39	678.3	277.3	220	57.3	239.1	0.24
40	477	1.01	3.40	0.77	757.9	280.9	144	136.9	189.6	0.72
60	508	1.50	3.48	1.14	771.8	263.8	113	150.8	163.3	0.92
80	521	2.01	3.52	1.54	777.4	256.4	100	156.4	152.1	1.03
100	527	2.48	3.56	1.90	783.6	256.6	94	162.6	148.2	1.10
120	530	3.00	3.60	2.29	790.4	260.4	91	169.4	147.5	1.15
140	530	3.51	3.66	2.68	799.4	269.4	91	178.4	150.5	1.19
160	529	4.01	3.72	3.06	808.7	279.7	92	187.7	154.6	1.21
180	527	4.55	3.77	3.47	817.9	290.9	94	196.9	159.6	1.23
200	524	5.07	3.83	3.87	825.9	301.9	97	204.9	165.3	1.24
220	521	5.58	3.90	4.26	837.7	316.7	100	216.7	172.2	1.26
240	517	6.10	3.96	4.66	847.7	330.7	103	227.7	178.9	1.27
260	513	6.59	4.03	5.03	858.4	345.4	108	237.4	187.1	1.27
280	509	7.11	4.11	5.43	872.2	363.2	112	251.2	195.7	1.28
300	504	7.61	4.16	5.81	879.9	375.9	116	259.9	202.6	1.28
320	499	8.09	4.26	6.18	896.6	397.6	122	275.6	213.9	1.29
340	494	8.59	4.33	6.56	908.2	414.2	126	288.2	222.1	1.30
360	489	9.10	4.40	6.95	920.2	431.2	132	299.2	231.7	1.29
380	484	9.63	4.48	7.36	931.0	447.0	137	310.0	240.3	1.29
400	478	10.12	4.56	7.73	945.5	467.5	143	324.5	251.2	1.29
420	472	10.65	4.65	8.14	958.5	486.5	149	337.5	261.5	1.29
440	466	11.13	4.73	8.50	972.4	506.4	155	351.4	272.1	1.29
460	461	11.66	4.83	8.90	987.8	526.8	160	366.8	282.3	1.30
480	454	12.19	4.90	9.31	997.8	543.8	167	376.8	292.6	1.29
500	448	12.69	5.00	9.69	1013.3	565.3	172	393.3	303.1	1.30
520	441	13.18	5.09	10.07	1028.3	587.3	180	407.3	315.8	1.29
540	434	13.67	5.19	10.45	1044.3	610.3	187	423.3	328.1	1.29
560	427	14.17	5.28	10.83	1057.1	630.1	193	437.1	338.7	1.29
580	420	14.68	5.38	11.22	1071.9	651.9	200	451.9	350.6	1.29
600	414	15.19	5.48	11.60	1088.5	674.5	207	467.5	362.8	1.29
620	406	15.72	5.58	12.01	1103.0	697.0	214	483.0	375.0	1.29
640	399	16.20	5.69	12.38	1120.0	721.0	222	499.0	388.3	1.29
660	392	16.72	5.78	12.78	1132.8	740.8	229	511.8	399.6	1.28
680	384	17.22	5.88	13.16	1147.6	763.6	237	526.6	412.5	1.28
700	377	17.70	5.98	13.52	1161.2	784.2	243	541.2	423.4	1.28
720	369	18.22	6.08	13.92	1175.1	806.1	251	555.1	436.0	1.27
740	363	18.73	6.19	14.31	1191.2	828.2	258	570.2	448.1	1.27
760	355	19.25	6.30	14.71	1206.5	851.5	266	585.5	461.2	1.27
780	348	19.77	6.40	15.10	1219.8	871.8	273	598.8	472.6	1.27
800	340	20.26	6.50	15.48	1234.1	894.1	281	613.1	485.4	1.26



### Triaxial Data Sheet – Saturation/ Consolidation

**Date:** 27/05/2019  
**Sample number:** 5593\_500kPa  
**Soil description:** cl' Sa  
**Borehole:** S2-1 (12.0 – 12.80 m)  
**Type of test:** Consolidated undrained  
**Effective confining stress:** 500 kPa

**Initial specimen height:**  $H_0 = 13.5$  cm  
**Initial specimen diameter:**  $D_0 = 7.0$  cm  
**Initial specimen volume:**  $V_0 = 519.5$  cm<sup>3</sup>  
**Specimen initial mass:**  $M_0 = 899$  g  
**Specimen initial density:**  $\rho = 1.73$  g/cm<sup>3</sup>  
**Initial water content:**  $W = 18$  %  
**Particles specific gravity:**  $\rho_s = 2.68$  g/cm<sup>3</sup>  
**Specimen initial void ratio:**  $e = 47$  %

**Final mass:**  $M = 909$  g  
**Final dry mass:**  $M_d = 737$  g  
**Final water content:**  $W = 19$  %

Time		Change in volume inside the cell chamber			Change in volume inside the specimen			Saturation		
Date	Time	Cell pressure [kPa]	Reading	$\Delta V$ [mm <sup>3</sup> ]	Back pressure [kPa]	Reading	$\Delta V$ [mm <sup>3</sup> ]	Pore pressure [kPa]	B-Value	Sr [%]
27/05/19	17:30	20			10					
27/05/19	17:35	20			10					
28/05/19	9:35	20			10					
28/05/19	11:30	20			10					
RAMP 20 kPa/d										
29/05/19	10:30	39			27					
30/05/19	10:00	56			46					
31/05/19	11:15	77			67					
03/06/19	9:40	135			126					
04/06/19	10:20	156			146					
05/06/19	11:50	160			150			150	15/20	75 %
05/06/19	11:50	180			BF	-		165		
RAMP 30 kPa/d Target: Cell pressure = 300 kPa Back pressure = 290 kPa										
05/06/19	12:15	180			165					
06/06/19	11:15	200			192					
07/06/19	10:10	233			222					
11/06/19	10:15	320			290			288	17/20	85 %
11/06/19	10:20	340			BF			305		
11/06/19	10:35	340			310					
12/06/19	11:35	320			310			310	19/20	95 %
12/06/19	11:35	340			BF			327		
12/06/19	11:55	340			320					
12/06/19	16:30	340			320					
12/06/19	10:30	360			350					
14/06/19	10:35	360			350			349	20/20	100 %
14/06/19	10:35	360			BF			369		
14/06/19	10:35	380			370					
Consolidation Target: Cell pressure = 870 kPa Back pressure = 370 kPa										
17/06/19	11:15	420			370					
17/06/19	11:30	420			370					
18/06/19	10:30	448			370					
19/06/19	10:30	480			370					
20/06/19	9:30	508			370					
21/06/19	11:40	542			370					
24/06/19	11:15	631			370					
25/06/19	11:00	661			370					
26/06/19	11:10	692			370					
27/06/19	9:20	718			370					
28/06/19	11:15	749			370					
01/07/19	9:40	836			370					
02/07/19	8:00	870			370					

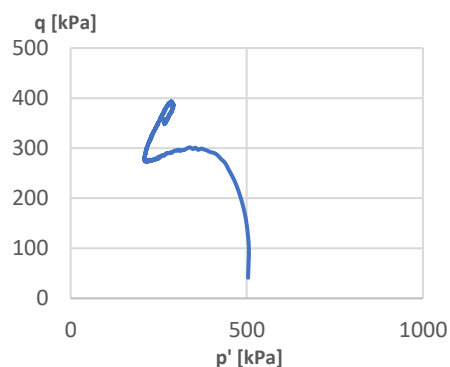
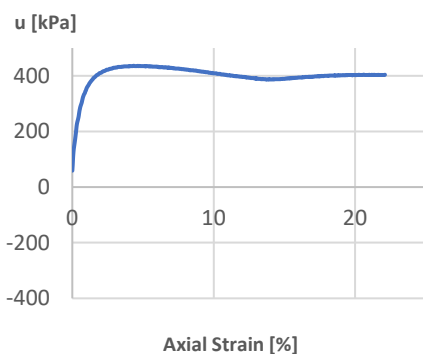
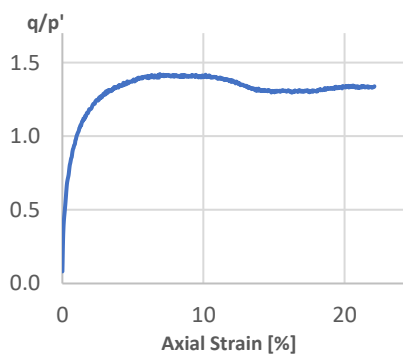
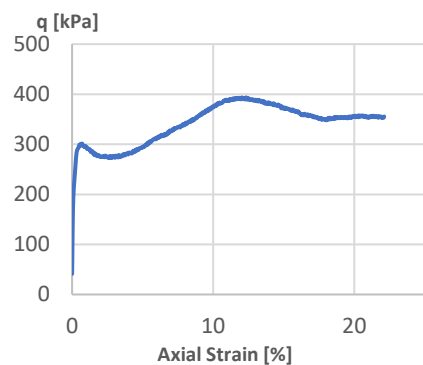


### Triaxial Data Sheet – Shearing

Date of shearing: 02/07/2019  
 Sample number: 5593\_500kPa  
 Strain rate: 0.05 mm/min

Cell pressure: 870 kPa  
 Back pressure: 370 kPa

Time	Pore Pressure	Axial Displacement	Axial Force	Axial Strain	Axial Stress	Eff. Axial Stress	Eff. Radial Stress	q	p'	q/p'
[min]	u [kPa]	v <sub>1</sub> [mm]	F [kN]	ε <sub>1</sub> [%]	σ <sub>1</sub> [kPa]	σ' <sub>1</sub> [kPa]	σ' <sub>3</sub> [kPa]	[kPa]	[kPa]	
0	379	0	3.50	0	910	531	490	41	503	0.08
20	637	0.98	4.54	0.73	1172	534.9	234	300.9	334.3	0.90
40	709	1.98	4.51	1.46	1154	444.8	162	282.8	256.3	1.10
60	737	2.99	4.51	2.21	1147	409.8	134	275.8	225.9	1.22
80	749	4.02	4.55	2.97	1147	398.4	122	276.4	214.1	1.29
100	754	5.04	4.59	3.73	1149	394.5	117	277.5	209.5	1.32
120	755	6.06	4.67	4.49	1160	405.0	116	289.0	212.3	1.36
140	754	7.04	4.75	5.21	1170	416.1	117	299.1	216.7	1.38
160	753	8.05	4.83	5.96	1181	428.2	118	310.2	221.4	1.40
180	750	9.12	4.93	6.75	1194	444.1	121	323.1	228.7	1.41
200	746	10.14	5.02	7.51	1206	459.7	125	334.7	236.6	1.41
220	741	11.16	5.10	8.26	1217	475.5	130	345.5	245.2	1.41
240	736	12.16	5.19	9.00	1227	491.5	135	356.5	253.8	1.40
260	731	13.15	5.29	9.73	1240	509.3	140	369.3	263.1	1.40
280	726	14.19	5.38	10.50	1252	526.0	145	381.0	272.0	1.40
300	721	15.22	5.46	11.27	1259	537.9	150	387.9	279.3	1.39
320	717	16.23	5.53	12.02	1264	547.3	154	393.3	285.1	1.38
340	712	17.27	5.56	12.78	1261	548.9	159	389.9	289.0	1.35
360	708	18.26	5.59	13.52	1255	547.1	163	384.1	291.0	1.32
380	707	19.28	5.60	14.27	1248	541.0	163	378.0	289.0	1.31
400	709	20.31	5.62	15.03	1242	532.6	162	370.6	285.5	1.30
420	713	21.34	5.66	15.79	1238	525.3	158	367.3	280.4	1.31
440	716	22.32	5.67	16.52	1229	513.5	155	358.5	274.5	1.31
460	718	23.35	5.70	17.28	1226	507.5	153	354.5	271.2	1.31
480	720	24.40	5.73	18.06	1219	499.0	151	348.0	267.0	1.30
500	721	25.40	5.79	18.80	1222	501.1	149	352.1	266.4	1.32
520	723	26.42	5.86	19.56	1224	501.1	148	353.1	265.7	1.33
540	723	27.43	5.92	20.30	1225	502.0	148	354.0	266.0	1.33
560	723	28.42	5.97	21.04	1225	501.6	148	353.6	265.9	1.33
580	723	29.43	6.04	21.79	1227	503.7	148	355.7	266.6	1.33



### Triaxial Data Sheet – Saturation/ Consolidation

**Date:** 24/07/2019  
**Sample number:** 5597\_50kPa  
**Soil description:** cl' Sa  
**Borehole:** S2-1 (18.0 – 19.0 m)  
**Type of test:** Consolidated undrained  
**Effective confining stress:** 50 kPa

**Initial specimen height:**  $H_0 = 13.5$  cm  
**Initial specimen diameter:**  $D_0 = 7.0$  cm  
**Initial specimen volume:**  $V_0 = 519.5$  cm<sup>3</sup>  
**Specimen initial mass:**  $M_0 = 1047,3$  g  
**Specimen initial density:**  $\rho = 2.0$  g/cm<sup>3</sup>  
**Initial water content:**  $W = 21$  %  
**Particle density:**  $\rho_s = 2.68$  g/cm<sup>3</sup>  
**Specimen initial void ratio:**  $e = 38$  %

**Final mass:**  $M = 1063,47$  g  
**Final dry mass:**  $M_d = 862,11$  g  
**Final water content:**  $W = 23.3$  %

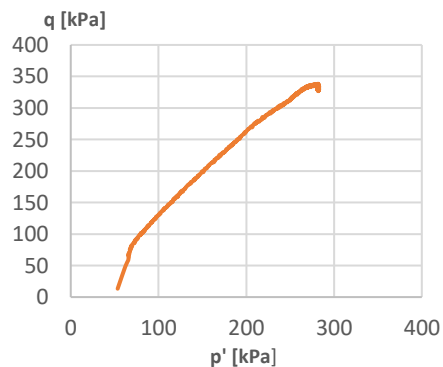
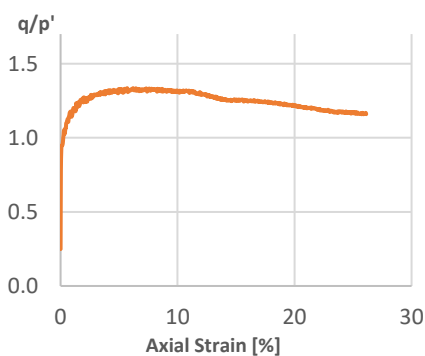
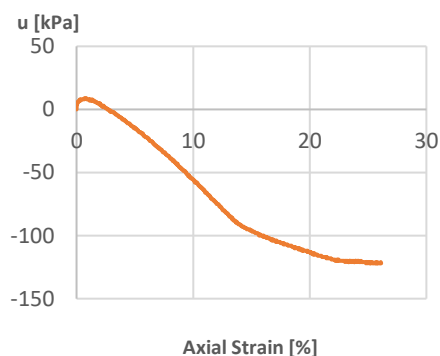
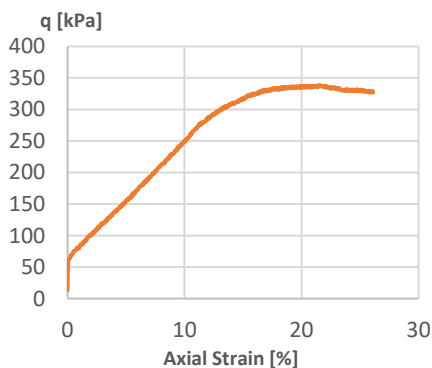
Time		Change in volume inside the cell chamber			Change in volume inside the specimen			Saturation		
Date	Time	Cell pressure [kPa]	Reading	$\Delta V$ [mm <sup>3</sup> ]	Back pressure [kPa]	Reading	$\Delta V$ [mm <sup>3</sup> ]	Pore pressure [kPa]	B-Value	Sr [%]
08/07/19	17:15	20	0	0	10	0	0			
08/07/19	17:30	20	-4284	-4284	10	-5608	-5608			
09/07/19	10:13	20	-5267	-983	10	-10048	-4440			
09/07/19	17:00	20	-8510	-3243	10	-38535	-28487			
09/07/19	17:30	20	-8658	-148	10	-66409	-27874			
09/07/19	17:40	20	-8618	40	10	0	0			
10/07/19	09:45	20	-9048	-430	10	-1207	65202			
RAMP		Target: Cell pressure = 120 kPa Back pressure = 110 kPa								
11/07/19	9:40	39	-10625	-1577	27	-5306	-4099			
12/07/19	9:30	64	-11396	-771	52	-10652	-5346			
12/07/19	16:50	71	-11396	0	60	-12094	-1442			
13/07/19	10:30	120	-12906	-1510	110	-19443	-7349	104	13/20	65 %
13/07/19	11:00	140	-	0	BF	-	0	117		
13/07/19	11:30	140	-13313	-407	130	-20397	-954			
RAMP		Target: Cell pressure = 240 kPa Back pressure = 230 kPa								
16/07/19	10:15	160	-13965	-652	151	-22655	-2258			
17/07/19	10:10	185	-14344	-379	176	-24149	-1494			
18/07/19	18:25	211	14956	29300	202	-25422	-1273			
18/07/19	11:05	220	15981	1025	210	-31315	-5893			
19/07/19	18:25	237	16265	284	228	-32368	-1053			
19/07/19	11:05	240	-16370	-32635	230	-32379	-11			
19/07/19	11:05	260	-	0	BF	-	0	225	18/20	90 %
19/07/19	11:05	260	-	0	250	-	0	243		
RAMP		Target: Cell pressure = 300 kPa Back pressure = 290 kPa								
22/07/19	10:10	300	-18038	-1668	290	-34115	-1736			
22/07/19	10:10	300	-	0	289	-	0	287	20/20	100 %
22/07/19	10:10	320	-	0	308	BF	0	307		
CONSOLIDATION		Target: Cell pressure = 360 kPa Back pressure = 290 kPa								
22/07/19	11:10	320	-19840	-1802	310	-34181	-66			
22/07/19	17:50	330	-19860	-20	310	-33579	602			
23/07/19	10:05	348	-20474	-614	310	-32479	1100			
23/07/19	15:50	360	-21050	-576	310	-31936	543			

### Triaxial Data Sheet – Shearing

Date of shearing: 24/07/2019  
 Sample number: 5597\_50kPa  
 Strain rate: 0.05 mm/min

Cell pressure: 360 kPa  
 Back pressure: 310 kPa

Time	Pore Pressure	Axial Displacement	Axial Force	Axial Strain	Axial Stress	Eff. Axial Stress	Eff. Radial Stress	q	p'	q/p'
[min]	u [kPa]	v <sub>1</sub> [mm]	F [kN]	ε <sub>1</sub> [%]	σ <sub>1</sub> [kPa]	σ' <sub>1</sub> [kPa]	σ' <sub>3</sub> [kPa]	[kPa]	[kPa]	
0	310	0.0	1.1	0.0	362.1	67.1	50	17.1	55.7	0.16
20	271.0	1.0	2.4	0.7	631.5	360.5	90	270.5	180.2	1.50
40	209.0	2.0	3.3	1.5	841.3	632.3	152	480.3	312.1	1.54
60	141.0	3.0	4.2	2.2	1057.1	916.1	220	696.1	452.0	1.54
80	79.0	4.0	5.0	2.9	1249.0	1170.0	282	888.0	578.0	1.54
100	38.0	4.9	5.5	3.7	1381.0	1343.0	323	1020.0	663.0	1.54
120	17.0	6.0	5.8	4.5	1452.0	1435.0	344	1091.0	707.7	1.54
140	5.0	7.1	6.0	5.2	1486.2	1481.2	355	1126.2	730.4	1.54
160	-3.0	8.1	6.2	6.0	1502.8	1505.8	364	1141.8	744.6	1.53
180	-9.0	9.1	6.2	6.7	1509.0	1518.0	370	1148.0	752.7	1.53
200	-14.0	10.1	6.3	7.5	1508.4	1522.4	375	1147.4	757.5	1.51
220	-19.0	11.1	6.3	8.2	1500.3	1519.3	380	1139.3	759.8	1.50
240	-23.0	12.1	6.3	9.0	1485.4	1508.4	384	1124.4	758.8	1.48
260	-26.0	13.2	6.3	9.7	1470.7	1496.7	387	1109.7	756.9	1.47
280	-29.0	14.2	6.3	10.5	1456.6	1485.6	390	1095.6	755.2	1.45
300	-31.0	15.2	6.3	11.3	1443.0	1474.0	392	1082.0	752.7	1.44
320	-32.0	16.2	6.2	12.0	1427.0	1459.0	393	1066.0	748.3	1.42
340	-34.0	17.2	6.2	12.8	1413.4	1447.4	395	1052.4	745.8	1.41
360	-35.0	18.3	6.2	13.5	1401.9	1436.9	396	1040.9	743.0	1.40
380	-36.0	19.3	6.3	14.3	1392.5	1428.5	397	1031.5	740.8	1.39
400	-37.0	20.3	6.2	15.0	1380.1	1417.1	398	1019.1	737.7	1.38
420	-37.0	21.3	6.3	15.8	1369.1	1406.1	398	1008.1	734.0	1.37
440	-38.0	22.3	6.2	16.5	1353.2	1391.2	399	992.2	729.7	1.36
460	-39.0	23.3	6.2	17.3	1337.8	1376.8	400	976.8	725.6	1.35
480	-39.0	24.3	6.2	18.0	1326.1	1365.1	400	965.1	721.7	1.34
500	-39.0	25.3	6.3	18.8	1322.1	1361.1	400	961.1	720.4	1.33
520	-38.0	26.4	6.3	19.5	1314.7	1352.7	399	953.7	716.9	1.33
540	-39.0	27.4	6.3	20.2	1307.0	1346.0	400	946.0	715.3	1.32
560	-38.0	28.4	6.3	21.0	1295.7	1333.7	399	934.7	710.6	1.32
580	-39.0	29.4	6.4	21.7	1292.5	1331.5	400	931.5	710.5	1.31
600	-39.0	30.4	6.4	22.5	1290.1	1329.1	400	929.1	709.7	1.31
620	-38.0	31.4	6.4	23.2	1286.1	1324.1	399	925.1	707.4	1.31
640	-38.0	32.4	6.5	24.0	1283.4	1321.4	399	922.4	706.5	1.31
660	-37.0	33.4	6.6	24.7	1283.7	1320.7	398	922.7	705.6	1.31
680	-38.0	34.4	6.6	25.5	1282.5	1320.5	399	921.5	706.2	1.30
700	-37.0	35.5	6.7	26.2	1278.2	1315.2	398	917.2	703.7	1.30
720	-37.0	36.4	6.7	27.0	1273.1	1310.1	398	912.1	702.0	1.30



**Direct shear test – Data Sheet**

<b>Sample</b>	<b>5598</b>	<b>Proving ring constant</b>	C = 0.428 kN/mm
<b>Date</b>	<b>07/06/2019</b>	<b>rate of displacement</b>	v = 0.5 mm/min
<b>Normal stress</b>	$\sigma' = 50$ kPa	<b>required weight</b>	m = 18.35 kg
<b>Specimen height</b>	H = 17.60 mm		
<b>Specimen area</b>	A = 3600.00 mm <sup>2</sup>	<b>T<sub>max</sub></b>	= 39 kPa
<b>Specimen Volume</b>	V = 63.45 cm <sup>3</sup>	<b><math>\phi_{peak}</math></b>	= 37.2 °
<b>Initial weight</b>	m = 112.11 g		
<b>Initial bulk density</b>	$\rho = 1.76$ g/cm <sup>3</sup>		
<b>Initial water content</b>	w = 0.046		
<b>Dry density</b>	$\rho_d = 1.68$ g/cm <sup>3</sup>		
<b>Initial void ratio</b>	e <sub>0</sub> = 0.57		
<b>Initial height</b>	H <sub>0</sub> = 17.6 mm		
<b>Hight after consolidation</b>	H = 17.1 mm		

Time [min]	Horizontal displacement $\delta h$ [mm]	Vertical displacement $\delta v$ [mm]	Shear force [mm]	Shear force T [kN]	$\tau$ [kPa]	$\tau/\sigma$
0	0.00	0.00	0.00	0.00	0.00	0.00
1	0.47	0.00	0.14	0.06	16.05	0.31
2	0.92	0.01	0.22	0.09	25.80	0.50
3	1.37	0.05	0.28	0.12	33.76	0.66
4	1.85	0.12	0.30	0.13	35.31	0.69
5	2.33	0.21	0.32	0.14	38.52	0.75
6	2.82	0.31	0.33	0.14	39.00	0.76
7	3.30	0.41	0.31	0.13	36.97	0.72
8	3.79	0.49	0.29	0.12	34.24	0.67
9	4.28	0.54	0.27	0.12	31.98	0.62
10	4.77	0.57	0.25	0.11	29.84	0.58
11	5.26	0.60	0.23	0.10	27.58	0.54
12	5.76	0.61	0.22	0.09	26.27	0.51
13	6.26	0.62	0.21	0.09	25.20	0.49
14	6.76	0.62	0.20	0.09	24.25	0.47
15	7.26	0.60	0.20	0.08	23.42	0.46
16	7.76	0.60	0.19	0.08	22.95	0.45
17	8.25	0.59	0.19	0.08	22.11	0.43
18	8.75	0.59	0.19	0.08	21.99	0.43
19	9.24	0.58	0.18	0.08	21.52	0.42
20	9.75	0.57	0.18	0.07	20.81	0.40
21	10.25	0.57	0.18	0.07	20.81	0.40
22	10.76	0.56	0.18	0.07	20.81	0.40
23	11.26	0.55	0.17	0.07	20.57	0.40
24	11.76	0.54	0.17	0.07	19.97	0.39
25	12.26	0.53	0.17	0.07	20.69	0.40
26	12.75	0.52	0.17	0.07	20.33	0.40

**Direct shear test – Data Sheet**

<b>Sample</b>	<b>5598</b>	<b>Proving ring constant</b>	C = 0.428	kN/mm
<b>Date</b>	<b>07/06/2019</b>	<b>rate of displacement</b>	v = 0.5	mm/min
<b>Normal stress</b>	$\sigma' = 280$	<b>required weight</b>	m = 102.75	kg
<b>Specimen height</b>	H = 17.60			
<b>Specimen area</b>	A = 3600.00		$\tau_{max} = 197.95$	kPa
<b>Specimen Volume</b>	V = 63.45		$\phi_{peak} = 35.12$	°
<b>Initial weight</b>	m = 114.72			
<b>Initial bulk density</b>	$\rho = 1.80$			g/cm <sup>3</sup>
<b>Initial water content</b>	w = 0.05			
<b>Dry density</b>	$\rho_d = 1.7$			g/cm <sup>3</sup>
<b>Initial void ratio</b>	$e_0 = 0.54$			
<b>Initial height</b>	H <sub>0</sub> = 17.6			mm
<b>Hight after consolidation</b>	H = 16.26			mm

Time [min]	Horizontal displacement $\delta h$ [mm]	Vertical displacement $\delta v$ [mm]	Shear force [mm]	Shear force T [kN]	$\tau$ [kPa]	$\tau/\sigma$
0	0.00	0.00	0.00	0.00	0.00	0.00
1	0.48	-0.09	0.23	0.10	26.87	0.10
2	0.94	-0.11	0.45	0.19	53.02	0.19
3	1.40	-0.12	0.64	0.28	76.56	0.27
4	1.86	-0.12	0.87	0.37	102.96	0.37
5	2.01	-0.11	0.91	0.39	107.83	0.38
6	2.07	-0.15	0.93	0.40	110.33	0.39
7	2.51	-0.15	1.12	0.48	133.16	0.47
8	2.97	-0.15	1.25	0.53	148.02	0.53
9	3.43	-0.15	1.37	0.59	163.35	0.58
10	3.89	-0.15	1.52	0.65	181.07	0.64
11	4.36	-0.15	1.65	0.71	196.52	0.70
12	4.84	-0.05	1.48	0.63	175.60	0.62
13	5.32	0.09	0.81	0.35	96.06	0.34
14	5.80	0.10	0.69	0.29	81.68	0.29
15	6.27	0.10	0.65	0.28	76.68	0.27
16	6.75	0.10	0.63	0.27	74.42	0.26
17	7.23	0.10	0.61	0.26	73.00	0.26
18	7.71	0.10	0.60	0.26	71.21	0.25
19	8.20	0.09	0.59	0.25	69.67	0.25
20	8.69	0.09	0.59	0.25	69.91	0.25
21	9.18	0.08	0.59	0.25	69.55	0.25
22	9.67	0.08	0.58	0.25	68.84	0.24
23	10.16	0.07	0.58	0.25	69.31	0.25
24	10.65	0.07	0.59	0.25	70.14	0.25
25	11.14	0.07	0.60	0.26	71.33	0.25
26	11.63	0.07	0.62	0.26	73.47	0.26

## Direct shear test – Data Sheet

<b>Sample</b>	<b>5598</b>	<b>Proving ring constant</b>	C = 0.428	kN/mm
<b>Date</b>	<b>07/06/2019</b>	<b>rate of displacement</b>	v = 0.5	mm/min
<b>Normal stress</b>	$\sigma' = 500$	<b>required weight</b>	m = 183.49	kg
<b>Specimen height</b>	H = 17.60			
<b>Specimen area</b>	A = 3600.00		$\tau_{max} = 401$	kPa
<b>Specimen Volume</b>	V = 63.45		$\phi_{peak} = 39^\circ$	
<b>Initial weight</b>	m = 117.3			
<b>Initial bulk density</b>	$\rho = 1.85$			g/cm <sup>3</sup>
<b>Initial water content</b>	w = 0.05			
<b>Dry density</b>	$\rho_d = 1.75$			g/cm <sup>3</sup>
<b>Initial void ratio</b>	$e_0 = 0.50$			
<b>Initial height</b>	$H_0 = 17.6$			mm
<b>Hight after consolidation</b>	H = 16.32			mm

Time [min]	Horizontal displacement $\delta h$ [mm]	Vertical displacement $\delta v$ [mm]	Shear force [mm]	Shear force T [kN]	$\tau$ [kPa]	$\tau/\sigma$
0	0.00	0.00	0.00	0.00	0.00	0.00
1	0.02	0.00	0.01	0.01	1.55	0.00
2	0.02	0.00	0.01	0.01	1.66	0.00
3	0.34	0.00	0.25	0.11	29.72	0.06
4	0.79	-0.03	0.56	0.24	66.34	0.13
5	1.24	-0.06	0.86	0.37	102.24	0.20
6	1.70	-0.07	1.16	0.50	137.91	0.28
7	2.16	-0.07	1.44	0.62	170.96	0.34
8	2.62	-0.07	1.71	0.73	203.18	0.41
9	3.07	-0.06	1.97	0.84	234.57	0.47
10	3.53	-0.04	2.23	0.96	265.36	0.53
11	3.98	-0.02	2.50	1.07	296.98	0.59
12	4.45	-0.01	2.75	1.18	326.83	0.65
13	4.91	0.00	2.99	1.28	355.48	0.71
14	5.37	0.01	3.17	1.36	376.64	0.75
15	5.84	0.01	3.27	1.40	388.41	0.77
16	6.30	-0.04	3.32	1.42	395.19	0.79
17	6.77	-0.06	3.37	1.44	401.13	0.80
18	7.24	-0.06	3.37	1.44	400.18	0.80
19	7.71	-0.05	3.18	1.36	378.42	0.75
20	8.18	-0.07	3.02	1.29	359.16	0.72
21	8.65	-0.09	3.16	1.35	376.05	0.75
22	9.12	-0.12	3.16	1.35	375.57	0.75
23	9.59	-0.14	3.25	1.39	386.51	0.77

**Direct shear test – Data Sheet**

**Sample**

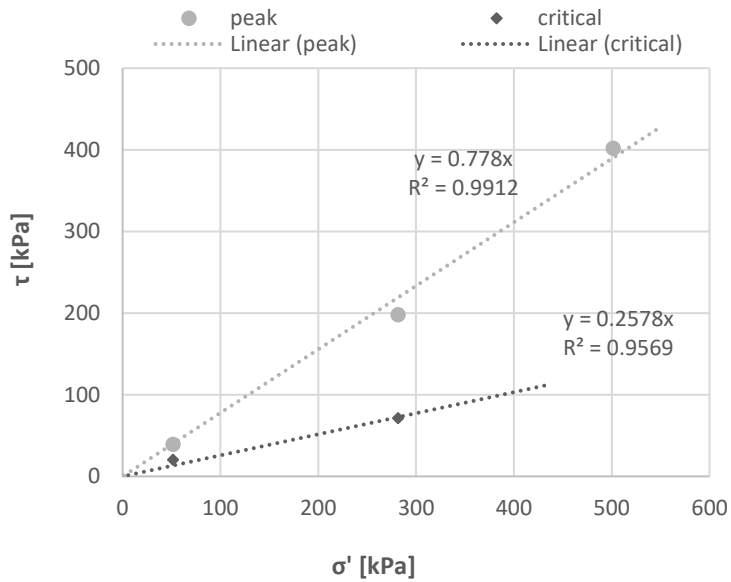
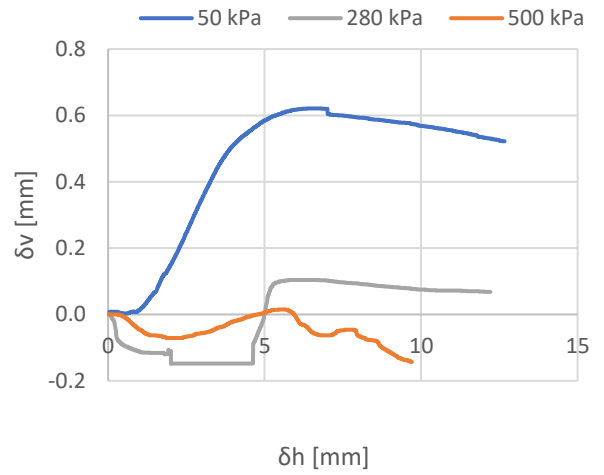
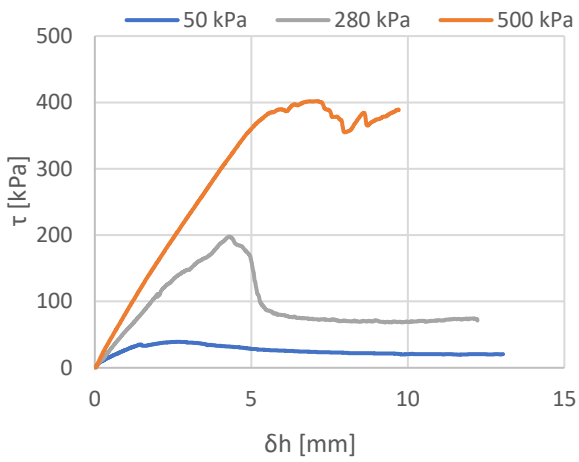
**5598**

$\varphi'_{peak} = 38^\circ$

**Date**

**07/06/2019**

$\varphi'_{crit} = 15^\circ$



## Direct shear test – Data Sheet

<b>Sample</b>	<b>5601</b>	<b>Proving ring constant</b>	C = 0.428	kN/mm
<b>Date</b>	<b>14/06/2019</b>	<b>rate of displacement</b>	v = 0.5	mm/min
<b>Normal stress</b>	$\sigma' =$ 50	<b>required weight</b>	m = 18.35	kg
<b>Specimen height</b>	H = 17.60			
<b>Specimen area</b>	A = 3600.00		$T_{max} =$ 57.19°	
<b>Specimen Volume</b>	V = 63.45		$\phi_{peak} =$ 48.04°	
<b>Initial weight</b>	m = 112.11			
<b>Initial bulk density</b>	$\rho =$ 1.80			
<b>Initial water content</b>	w = 0.05			
<b>Dry density</b>	$\rho_d =$ 1.71			
<b>Initial void ratio</b>	$e_0 =$ 0.55			
<b>Initial height</b>	$H_0 =$ 17.60			
<b>Height after consolidation</b>	H = 17.13			

Time [min]	Horizontal displacement $\delta h$ [mm]	Vertical displacement $\delta v$ [mm]	Shear force [mm]	Shear force T [kN]	$\tau$ [kPa]	$\tau/\sigma$
0	0	-	0	0	0	0
1	0.11	-	0.08	0.03	9.51	0.19
2	0.12	-	0.08	0.03	9.63	0.19
3	0.34	-	0.13	0.06	15.46	0.30
4	0.78	-	0.22	0.10	26.39	0.51
5	1.23	-	0.31	0.13	36.26	0.71
6	1.70	-	0.36	0.15	42.21	0.82
7	2.19	-	0.39	0.17	46.25	0.90
8	2.66	-	0.44	0.19	52.55	1.02
9	3.14	-	0.48	0.20	56.59	1.10
10	3.63	-	0.48	0.20	56.71	1.10
11	4.11	-	0.43	0.18	51.36	1.00
12	4.61	-	0.39	0.17	46.25	0.90
13	5.11	-	0.36	0.15	42.80	0.83
14	5.61	-	0.34	0.15	40.78	0.79
15	6.10	-	0.33	0.14	39.71	0.77
16	6.60	-	0.33	0.14	39.35	0.77
17	7.09	-	0.33	0.14	39.11	0.76
18	7.58	-	0.33	0.14	38.88	0.76



**Direct shear test – Data Sheet**

<b>Sample</b>	<b>5601</b>	<b>Proving ring constant</b>	C = 0.428	kN/mm
<b>Date</b>	<b>14/06/2019</b>	<b>rate of displacement</b>	v = 0.5	mm/min
<b>Normal stress</b>	$\sigma' =$ 280	<b>required weight</b>	m = 102.75	kg
<b>Specimen height</b>	H = 17.60			
<b>Specimen area</b>	A = 3600.00		$\tau_{max} =$ 293.42	kPa
<b>Specimen Volume</b>	V = 63.45		$\phi_{peak} =$ 46.20	°
<b>Initial weight</b>	m = 114.72			
<b>Initial bulk density</b>	$\rho =$ 1.8			
<b>Initial water content</b>	w = 0.05			
<b>Dry density</b>	$\rho_d =$ 1.72			
<b>Initial void ratio</b>	$e_0 =$ 0.539			
<b>Initial height</b>	$H_0 =$ 17.6			
<b>Height after consolidation</b>	H = 16.26			

Time [min]	Horizontal displacement $\delta h$ [mm]	Vertical displacement $\delta v$ [mm]	Shear force [mm]	Shear force T [kN]	$\tau$ [kPa]	$\tau/\sigma$
0	0.00	0.00	0.00	0.00	0.00	0.00
1	0.38	-	0.08	0.04	9.99	0.04
2	0.86	-	0.28	0.12	32.81	0.12
3	1.32	-	0.58	0.25	69.19	0.25
4	1.79	-	0.88	0.38	104.74	0.37
5	2.27	-	1.15	0.49	136.13	0.48
6	2.73	-	1.39	0.59	164.90	0.59
7	3.18	-	1.62	0.69	192.12	0.68
8	3.65	-	1.84	0.79	218.76	0.78
9	4.11	-	2.04	0.87	242.77	0.86
10	4.57	-	2.22	0.95	263.34	0.94
11	5.04	-	2.40	1.03	285.81	1.02
12	5.52	-	2.46	1.05	292.82	1.04
13	5.98	-	2.46	1.05	292.82	1.04
14	6.48	-	2.46	1.05	292.82	1.04
15	6.96	-	2.46	1.05	292.82	1.04
16	7.45	-	2.46	1.05	292.82	1.04
17	7.93	-	2.46	1.05	292.82	1.04
18	8.43	-	2.46	1.05	292.82	1.04
19	8.92	-	2.46	1.05	292.82	1.04
20	9.41	-	2.46	1.05	292.82	1.04
21	9.91	-	2.46	1.05	292.82	1.04
22	10.40	-	2.46	1.05	292.82	1.04
23	10.88	-	2.46	1.05	292.82	1.04
24	11.38	-	2.46	1.05	292.82	1.04
25	11.87	-	2.46	1.05	292.82	1.04
26	12.36	-	2.46	1.05	292.82	1.04

**Direct shear test – Data Sheet**

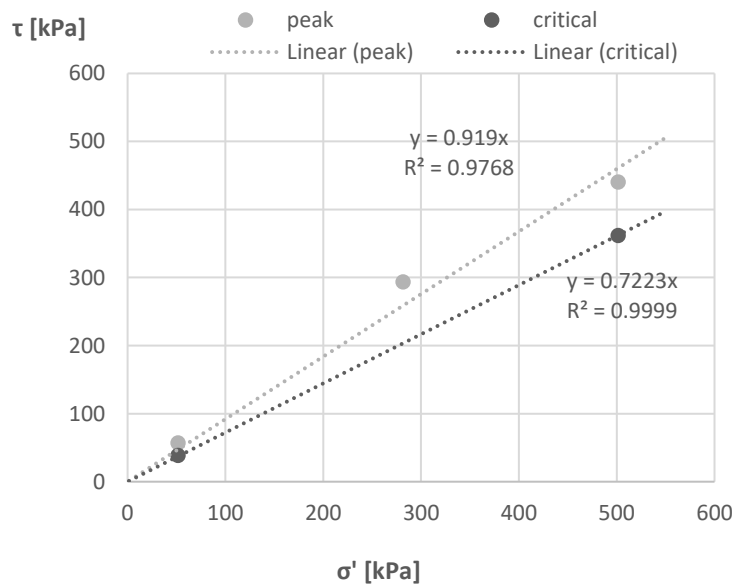
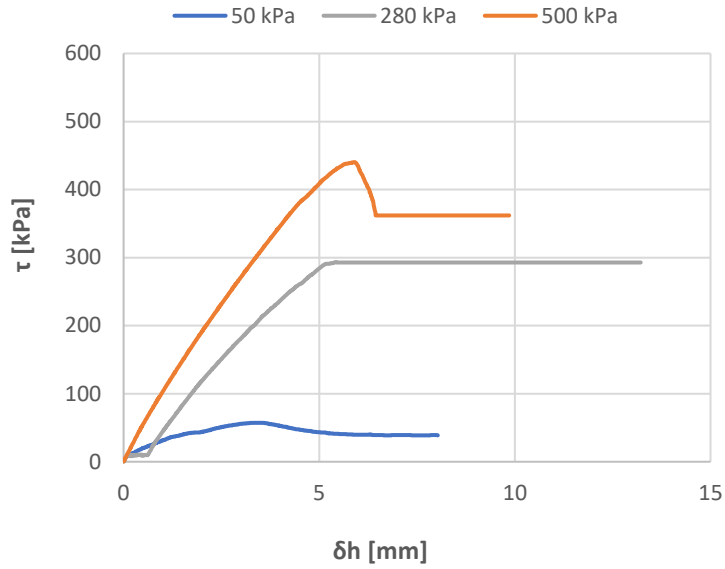
<b>Sample</b>	<b>5601</b>	<b>Proving ring constant</b>	C = 0.428	kN/mm
<b>Date</b>	<b>14/06/2019</b>	<b>rate of displacement</b>	v = 0.5	mm/min
<b>Normal stress</b>	$\sigma' =$ 500	<b>required weight</b>	m = 183.49	kg
<b>Specimen height</b>	H = 17.60			
<b>Specimen area</b>	A = 3600.00		$T_{max} =$ 440	kPa
<b>Specimen Volume</b>	V = 63.45		$\phi_{peak} =$ 41.28	°
<b>Initial weight</b>	m = 117.38			
<b>Initial bulk density</b>	$\rho =$ 1.85			
<b>Initial water content</b>	w = 0.05			
<b>Dry density</b>	$\rho_d =$ 1.76			
<b>Initial void ratio</b>	$e_0 =$ 0.50			
<b>Initial height</b>	$H_0 =$ 17.6			
<b>Height after consolidation</b>	H = 16.32			

Time [min]	Horizontal displacement $\delta h$ [mm]	Vertical displacement $\delta v$ [mm]	Shear force [mm]	Shear force T [kN]	$\tau$ [kPa]	$\tau/\sigma$
0	0.00	-	0.00	0.00	0.00	0.00
1	0.37	-	0.35	0.15	41.97	0.08
2	0.81	-	0.71	0.31	84.89	0.17
3	1.25	-	1.06	0.45	126.02	0.25
4	1.72	-	1.41	0.60	167.04	0.33
5	2.17	-	1.73	0.74	205.32	0.41
6	2.63	-	2.04	0.87	242.06	0.48
7	3.08	-	2.34	1.00	278.56	0.56
8	3.55	-	2.63	1.13	312.80	0.62
9	4.01	-	2.92	1.25	346.92	0.69
10	4.47	-	3.19	1.36	378.78	0.76
11	4.93	-	3.40	1.46	404.46	0.81
12	5.39	-	3.60	1.54	428.12	0.85
13	5.87	-	3.70	1.58	440.13	0.88
14	6.34	-	3.27	1.40	388.89	0.78
15	6.84	-	3.05	1.30	362.14	0.72
16	7.32	-	3.05	1.30	362.14	0.72
17	7.79	-	3.05	1.30	362.14	0.72
18	8.26	-	3.05	1.30	362.14	0.72
19	8.74	-	3.05	1.30	362.14	0.72
20	9.21	-	3.05	1.30	362.14	0.72
21	9.68	-	3.05	1.30	362.14	0.72

**Direct shear test – Data Sheet**

Sample **5601**  
 Date **14/06/2019**

$\varphi'_{peak} = 42^\circ$   
 $\varphi'_{crit} = 36^\circ$



*Note: Results are unusable due to high frame opening and tilting of the shear box's top cap whereby soil interlocked between both frames.*

**Direct shear test – Data Sheet**

<b>Sample</b>	<b>5604</b>	<b>Proving ring constant</b>	C = 0.428 kN/mm
<b>Date</b>	<b>05/06/2019</b>	<b>rate of displacement</b>	v = 0.5 mm/min
<b>Normal stress</b>	$\sigma' = 50$ kPa	<b>required weight</b>	m = 18.35 kg
<b>Specimen height</b>	H = 17.60 mm		
<b>Specimen area</b>	A = 3600.00 mm <sup>2</sup>	<b>T<sub>max</sub></b>	= 39 kPa
<b>Specimen Volume</b>	V = 63.45 cm <sup>3</sup>	<b><math>\phi_{peak}</math></b>	= 37 °
<b>Initial weight</b>	m = 114.88 g		
<b>Initial bulk density</b>	$\rho = 1.811$ g/cm <sup>3</sup>		
<b>Initial water content</b>	w = 0.056		
<b>Dry density</b>	$\rho_d = 1.71$ g/cm <sup>3</sup>		
<b>Initial void ratio</b>	e <sub>0</sub> = 0.54		
<b>Initial height</b>	H <sub>0</sub> = 17.6 mm		
<b>Hight after consolidation</b>	H = 17.1 mm		

Time [min]	Horizontal displacement $\delta h$ [mm]	Vertical displacement $\delta v$ [mm]	Shear force [mm]	Shear force T [kN]	$\tau$ [kPa]	$\tau/\sigma$
0	0	0	0	0	0	0
1	0.45	0.03	0.19	0.08	22.47	0.44
2	0.93	0.10	0.27	0.12	32.58	0.63
3	1.43	0.21	0.31	0.13	37.21	0.72
4	1.92	0.33	0.33	0.14	38.64	0.75
5	2.43	0.45	0.30	0.13	35.55	0.69
6	2.92	0.54	0.27	0.12	32.22	0.63
7	3.42	0.59	0.25	0.11	29.48	0.57
8	3.92	0.62	0.23	0.10	26.99	0.52
9	4.42	0.64	0.21	0.09	24.97	0.49
10	4.93	0.65	0.21	0.09	24.61	0.48
11	5.44	0.66	0.21	0.09	24.49	0.48
12	5.94	0.67	0.20	0.09	24.13	0.47
13	6.45	0.68	0.21	0.09	24.49	0.48
14	6.95	0.68	0.21	0.09	24.61	0.48
15	7.45	0.69	0.20	0.09	24.25	0.47
16	7.95	0.70	0.20	0.09	23.90	0.46
17	8.46	0.71	0.20	0.09	23.90	0.46
18	8.97	0.71	0.20	0.09	24.13	0.47
19	9.48	0.72	0.19	0.08	23.06	0.45
20	9.98	0.73	0.20	0.08	23.30	0.45
21	10.49	0.73	0.19	0.08	23.06	0.45
22	10.99	0.74	0.20	0.08	23.18	0.45
23	11.49	0.74	0.19	0.08	23.06	0.45
24	12.00	0.75	0.18	0.08	21.04	0.41
25	12.49	0.75	0.19	0.08	22.71	0.44

## Direct shear test – Data Sheet

<b>Sample</b>	<b>5604</b>	<b>Proving ring constant</b>	C = 0.428	kN/mm
<b>Date</b>	<b>05/06/2019</b>	<b>rate of displacement</b>	v = 0.5	mm/min
<b>Normal stress</b>	$\sigma' = 280$	<b>required weight</b>	m = 102.75	kg
<b>Specimen height</b>	H = 17.60			
<b>Specimen area</b>	A = 3600.00		$T_{max} = 257.16$	kPa
<b>Specimen Volume</b>	V = 63.45		$\phi_{peak} = 42.42$	°
<b>Initial weight</b>	m = 116.8			g
<b>Initial bulk density</b>	$\rho = 1.84$			g/cm <sup>3</sup>
<b>Initial water content</b>	w = 0.056			
<b>Dry density</b>	$\rho_d = 1.74$			g/cm <sup>3</sup>
<b>Initial void ratio</b>	$e_0 = 0.52$			
<b>Initial height</b>	$H_0 = 17.6$			mm
<b>Hight after consolidation</b>	H = 16.65			mm

Time [min]	Horizontal displacement $\delta h$ [mm]	Vertical displacement $\delta v$ [mm]	Shear force [mm]	Shear force T [kN]	$\tau$ [kPa]	$\tau/\sigma$
0	0.00	0.00	0.00	0.01	0.00	0.00
1	0.48	-0.01	0.35	0.15	41.49	0.15
2	0.93	-0.02	0.64	0.27	75.61	0.27
3	1.39	-0.02	0.90	0.38	106.88	0.38
4	1.85	-0.02	1.17	0.50	138.62	0.49
5	2.31	0.00	1.42	0.61	168.70	0.60
6	2.77	0.03	1.65	0.71	195.93	0.70
7	3.23	0.06	1.86	0.80	220.90	0.78
8	3.70	0.10	2.01	0.86	239.44	0.85
9	4.17	0.15	2.10	0.90	250.14	0.89
10	4.63	0.21	2.15	0.92	255.61	0.91
11	5.10	0.21	2.04	0.87	242.65	0.86
12	5.57	0.18	2.00	0.85	237.18	0.84
13	6.04	0.20	2.03	0.87	241.70	0.86
14	6.53	0.28	1.56	0.67	185.82	0.66
15	7.03	0.29	1.39	0.59	164.78	0.59
16	7.53	0.29	1.34	0.57	159.55	0.57
17	8.02	0.29	1.33	0.57	157.77	0.56
18	8.51	0.29	1.31	0.56	155.15	0.55
19	9.00	0.29	1.27	0.54	150.99	0.54
20	9.49	0.28	1.24	0.53	147.18	0.52
21	9.99	0.28	1.24	0.53	146.83	0.52
22	10.48	0.27	1.23	0.53	146.00	0.52
23	10.98	0.27	1.21	0.52	143.74	0.51
24	11.48	0.26	1.22	0.52	144.45	0.51
25	11.98	0.25	1.17	0.50	139.58	0.50
26	12.48	0.25	1.16	0.50	137.91	0.49

**Direct shear test – Data Sheet**

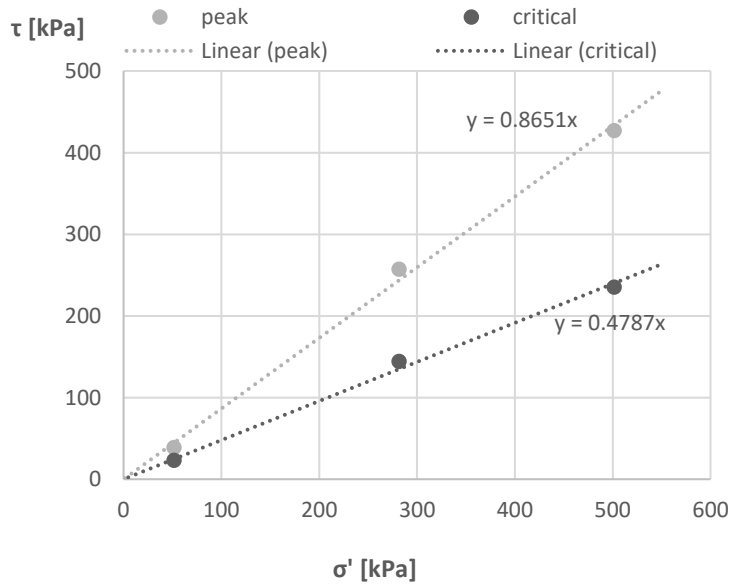
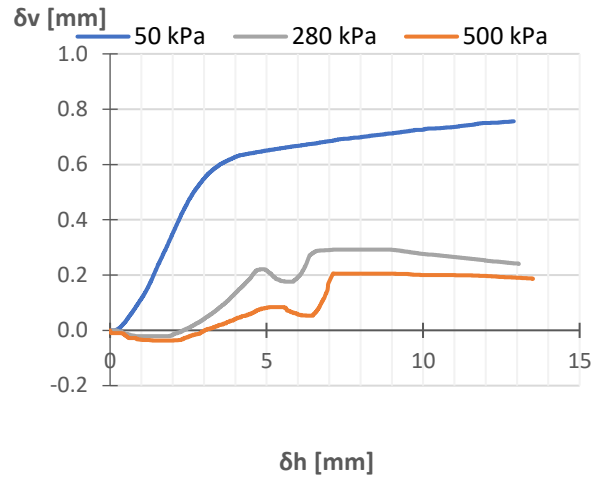
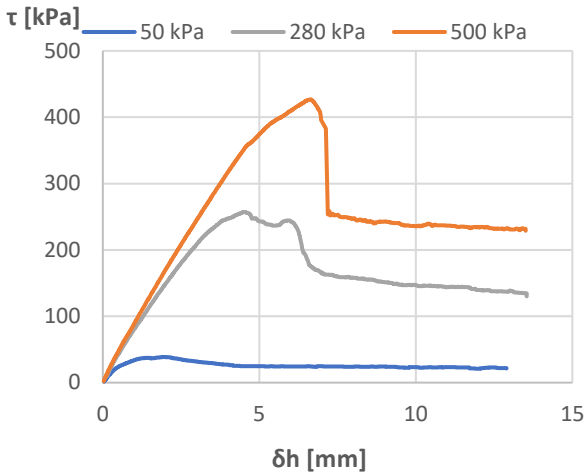
<b>Sample</b>	<b>5604</b>	<b>Proving ring constant</b>	C = 0.428 kN/mm
<b>Date</b>	<b>05/06/2019</b>	<b>rate of displacement</b>	v = 0.5 mm/min
<b>Normal stress</b>	$\sigma' = 500$ kPa	<b>required weight</b>	m = 183.49 kg
<b>Specimen height</b>	H = 17.60 mm		
<b>Specimen area</b>	A = 3600.00 mm <sup>2</sup>	<b>T<sub>max</sub></b>	= 426 kPa
<b>Specimen Volume</b>	V = 63.45 cm <sup>3</sup>	<b><math>\phi_{peak}</math></b>	= 40 °
<b>Initial weight</b>	m = 119.28 g		
<b>Initial bulk density</b>	$\rho = 1.88$ g/cm <sup>3</sup>		
<b>Initial water content</b>	w = 0.056		
<b>Dry density</b>	$\rho_d = 1.78$ g/cm <sup>3</sup>		
<b>Initial void ratio</b>	e <sub>0</sub> = 0.48		
<b>Initial height</b>	H <sub>0</sub> = 17.6 mm		
<b>Hight after consolidation</b>	H = 16.27 mm		

Time [min]	Horizontal displacement $\delta h$ [mm]	Vertical displacement $\delta v$ [mm]	Shear force [mm]	Shear force T [kN]	$\tau$ [kPa]	$\tau/\sigma$
0	0.00	0.00	0.00	0.01	0.00	0.00
1	0.44	-0.01	0.36	0.15	42.21	0.08
2	0.89	-0.03	0.67	0.29	79.42	0.16
3	1.34	-0.04	0.99	0.42	117.11	0.23
4	1.80	-0.04	1.30	0.55	153.96	0.31
5	2.26	-0.04	1.60	0.68	189.75	0.38
6	2.72	-0.02	1.89	0.81	224.70	0.45
7	3.18	0.01	2.17	0.93	258.35	0.52
8	3.63	0.02	2.45	1.05	291.40	0.58
9	4.09	0.05	2.72	1.16	323.26	0.64
10	4.55	0.06	2.98	1.28	354.41	0.71
11	5.01	0.08	3.15	1.35	374.74	0.75
12	5.48	0.08	3.32	1.42	394.24	0.79
13	5.95	0.06	3.44	1.47	408.38	0.81
14	6.42	0.05	3.55	1.52	422.17	0.84
15	6.89	0.13	3.47	1.48	412.19	0.82
16	7.54	0.21	2.11	0.90	251.21	0.50
17	8.01	0.21	2.08	0.89	247.53	0.49
18	8.48	0.21	2.04	0.87	242.41	0.48
19	8.95	0.21	2.04	0.87	242.41	0.48
20	9.42	0.20	2.02	0.87	240.51	0.48
21	9.90	0.20	1.99	0.85	236.11	0.47
22	10.37	0.20	2.01	0.86	239.09	0.48
23	10.84	0.20	2.00	0.85	237.30	0.47
24	11.31	0.20	1.98	0.85	235.28	0.47
25	11.78	0.20	1.97	0.84	233.62	0.47

**Direct shear test – Data Sheet**

**Sample** 5604  
**Date** 05/06/2019

$\varphi'_{peak} = 41^\circ$   
 $\varphi'_{crit} = 26^\circ$



**Direct shear test – Data Sheet**

<b>Sample</b>	<b>5609</b>	<b>Proving ring constant</b>	C = 0.428 kN/mm
<b>Date</b>	<b>11/06/2019</b>	<b>rate of displacement</b>	v = 0.5 mm/min
<b>Normal stress</b>	$\sigma' = 50$ kPa	<b>required weight</b>	m = 18.35 kg
<b>Specimen height</b>	H = 17.60 mm		
<b>Specimen area</b>	A = 3600.00 mm <sup>2</sup>	<b>T<sub>max</sub></b>	= 41 kPa
<b>Specimen Volume</b>	V = 63.45 cm <sup>3</sup>	<b><math>\phi_{peak}</math></b>	= 39 °
<b>Initial weight</b>	m = 115.63 g		
<b>Initial bulk density</b>	$\rho = 1.82$ g/cm <sup>3</sup>		
<b>Initial water content</b>	w = 0.051		
<b>Dry density</b>	$\rho_d = 1.73$ g/cm <sup>3</sup>		
<b>Initial void ratio</b>	e <sub>0</sub> = 0.53		
<b>Initial height</b>	H <sub>0</sub> = 17.6 mm		
<b>Hight after consolidation</b>	H = 17.1 mm		

Time [min]	Horizontal displacement $\delta h$ [mm]	Vertical displacement $\delta v$ [mm]	Shear force [mm]	Shear force T [kN]	$\tau$ [kPa]	$\tau/\sigma$
0	0	0	0	0	0	0
1	0.53	-0.01	0.10	0.04	12.36	0.24
2	1.00	0.00	0.21	0.09	24.37	0.47
3	1.46	0.04	0.28	0.12	32.93	0.64
4	1.94	0.13	0.33	0.14	38.88	0.76
5	2.43	0.25	0.31	0.13	37.09	0.72
6	2.92	0.37	0.32	0.14	38.04	0.74
7	3.42	0.50	0.29	0.12	34.24	0.67
8	3.91	0.60	0.23	0.10	27.58	0.54
9	4.40	0.64	0.17	0.07	20.33	0.40
10	4.90	0.65	0.14	0.06	17.00	0.33
11	5.39	0.65	0.13	0.06	15.57	0.30
12	5.88	0.65	0.13	0.06	15.81	0.31
13	6.38	0.65	0.13	0.05	15.22	0.30
14	6.88	0.64	0.13	0.06	15.57	0.30
15	7.38	0.64	0.13	0.05	14.86	0.29
16	7.88	0.64	0.12	0.05	14.62	0.28
17	8.38	0.64	0.12	0.05	14.62	0.28
18	8.88	0.64	0.11	0.05	13.20	0.26



## Direct shear test – Data Sheet

<b>Sample</b>	<b>5609</b>	<b>Proving ring constant</b>	C = 0.428	kN/mm
<b>Date</b>	<b>11/06/2019</b>	<b>rate of displacement</b>	v = 0.5	mm/min
<b>Normal stress</b>	$\sigma' = 280$	<b>required weight</b>	m = 102.75	kg
<b>Specimen height</b>	H = 17.60			
<b>Specimen area</b>	A = 3600.00		$T_{max} = 264$	kPa
<b>Specimen Volume</b>	V = 63.45		$\phi_{peak} = 43^\circ$	
<b>Initial weight</b>	m = 116.01			
<b>Initial bulk density</b>	$\rho = 1.82$			g/cm <sup>3</sup>
<b>Initial water content</b>	w = 0.05			
<b>Dry density</b>	$\rho_d = 1.72$			g/cm <sup>3</sup>
<b>Initial void ratio</b>	$e_0 = 0.53$			
<b>Initial height</b>	H <sub>0</sub> = 17.6			mm
<b>Hight after consolidation</b>	H = 16.55			mm

Time [min]	Horizontal displacement $\delta h$ [mm]	Vertical displacement $\delta v$ [mm]	Shear force [mm]	Shear force T [kN]	$\tau$ [kPa]	$\tau/\sigma$
0	0	0	0	0	0	0
1	0.44	0.00	0.24	0.10	28.89	0.10
2	0.92	-0.01	0.54	0.23	63.72	0.23
3	1.39	-0.02	0.80	0.34	94.87	0.34
4	1.87	-0.01	1.04	0.45	123.76	0.44
5	2.35	0.00	1.29	0.55	153.25	0.54
6	2.82	0.02	1.50	0.64	178.69	0.63
7	3.28	0.04	1.68	0.72	199.61	0.71
8	3.74	0.06	1.88	0.80	222.92	0.79
9	4.21	0.09	2.06	0.88	245.15	0.87
10	4.68	0.14	2.19	0.94	260.13	0.92
11	5.15	0.24	2.11	0.90	250.86	0.89
12	5.64	0.34	1.82	0.78	216.14	0.77
13	6.14	0.34	1.82	0.78	216.14	0.77
14	6.62	0.34	1.82	0.78	216.14	0.77
15	7.12	0.34	1.82	0.78	216.14	0.77
16	7.61	0.33	1.82	0.78	216.14	0.77
17	8.10	0.32	1.82	0.78	216.14	0.77
18	8.59	0.31	1.82	0.78	216.14	0.77
19	9.09	0.30	1.82	0.78	216.14	0.77
20	9.59	0.29	1.82	0.78	216.14	0.77
21	10.08	0.28	1.82	0.78	216.14	0.77
22	10.58	0.27	1.82	0.78	216.14	0.77
23	11.07	0.26	1.82	0.78	216.14	0.77
24	11.56	0.25	1.82	0.78	216.14	0.77
25	12.06	0.24	1.82	0.78	216.14	0.77
26	12.56	0.23	1.82	0.78	216.14	0.77

**Direct shear test – Data Sheet**

<b>Sample</b>	<b>5609</b>	<b>Proving ring constant</b>	C = 0.428	kN/mm
<b>Date</b>	<b>11/06/2019</b>	<b>rate of displacement</b>	v = 0.5	mm/min
<b>Normal stress</b>	$\sigma' = 500$	<b>required weight</b>	m = 183.49	kg
<b>Specimen height</b>	H = 17.60			
<b>Specimen area</b>	A = 3600.00		$T_{max} = 453$	kPa
<b>Specimen Volume</b>	V = 63.45		$\phi_{peak} = 42^\circ$	
<b>Initial weight</b>	m = 116.73			
<b>Initial bulk density</b>	$\rho = 1.84$			g/cm <sup>3</sup>
<b>Initial water content</b>	w = 0.0568			
<b>Dry density</b>	$\rho_d = 1.7411$			g/cm <sup>3</sup>
<b>Initial void ratio</b>	$e_0 = 0.522$			
<b>Initial height</b>	H <sub>0</sub> = 17.6			mm
<b>Hight after consolidation</b>	H = 16.11			mm

Time [min]	Horizontal displacement $\delta h$ [mm]	Vertical displacement $\delta v$ [mm]	Shear force [mm]	Shear force T [kN]	$\tau$ [kPa]	$\tau/\sigma$
0	0	0	0	0	0	0
1	0.41	0.01	0.34	0.15	40.66	0.08
2	0.86	0.01	0.71	0.30	84.29	0.17
3	1.32	0.01	1.03	0.44	122.22	0.24
4	1.86	0.01	1.37	0.59	162.64	0.32
5	2.31	0.02	1.64	0.70	195.45	0.39
6	2.77	0.03	1.92	0.82	228.15	0.46
7	3.23	0.04	2.20	0.94	261.08	0.52
8	3.68	0.05	2.43	1.04	288.90	0.58
9	4.15	0.05	2.65	1.14	315.41	0.63
10	4.61	0.05	2.85	1.22	338.48	0.68
11	5.07	0.03	3.04	1.30	360.95	0.72
12	5.54	0.02	3.22	1.38	382.23	0.76
13	6.00	0.02	3.47	1.49	412.66	0.82
14	6.46	0.04	3.65	1.56	434.06	0.87
15	6.92	0.08	3.80	1.63	452.02	0.90
16	7.40	0.18	3.55	1.52	422.53	0.84
17	7.91	0.22	3.04	1.30	361.90	0.72
18	8.39	0.21	3.04	1.30	361.90	0.72
19	8.86	0.20	3.04	1.30	361.90	0.72
20	9.33	0.19	3.04	1.30	361.90	0.72
21	9.80	0.19	3.04	1.30	361.90	0.72
22	10.27	0.18	3.04	1.30	361.90	0.72
23	10.74	0.17	3.04	1.30	361.90	0.72
24	11.21	0.16	3.04	1.30	361.90	0.72
25	11.68	0.16	3.04	1.30	361.90	0.72

**Direct shear test – Data Sheet**

**Sample** 5609  
**Date** 11/06/2019

$\varphi'_{peak} = 42^\circ$   
 $\varphi'_{crit} = 36^\circ$

